RICE UNIVERSITY

Exclusive Vector Meson Photoproduction in Ultraperipheral Heavy-Ion Collisions at the LHC with the CMS Detector

Thesis by

JiaZhao Lin

RICE

Doctor of Philosophy
Department of Physics and Astronomy
Rice University (Houston, Texas, USA) May, 2025

RICE UNIVERSITY

Exclusive Vector Meson Photoproduction in Ultraperipheral Heavy-Ion Collisions at the LHC with the CMS Detector

By

JiaZhao Lin

A THESIS SUBMITTED
IN PARTIAL FULFILLMENT OF THE
REQUIREMENTS FOR THE DEGREE

Doctor of Philosophy

APPROVED, THESIS COMMITTEE

Wei Li (Chair)

Professor, Department of Physics and Astronomy

Frank Geurts (May 5, 2025 14:03 CDT)

Frank Geurts

Professor, Department of Physics and Astronomy

Stephen Semmes

Stephen Semmes (May 5, 2025 09:08 CDT)

Stephen Semmes

Noah Harding Professor of Mathematics

HOUSTON, TEXAS

May 2025

Department of Physics and Astronomy
Rice University
Doctoral Thesis and Defense Report

Student's name: JiaZhao Liu

Report of the Committee – Doctoral thesis and defense

1) Please rate the extent to which the candidate demonstrated proficiency in reading the scientific literature in the doctoral thesis and oral defense (1 = inadequate; 3 = adequate; 5 = outstanding): 5

2) Please rate the extent to which the candidate demonstrated proficiency in oral and written communication of scientific ideas and results (1 = inadequate; 3 = adequate; 5 = outstanding): 4

3) Please rate the extent to which the candidate demonstrated the skills relevant for independent research in physics/astronomy (1 = inadequate; 3 = adequate; 5 = outstanding): 5

4) Please rate the extent to which the student has made an original and significant contribution to knowledge in their discipline (1 = inadequate; 3 = adequate; 5 = outstanding): 5

(a) Signature — Wei Li — Name (print or type)

(b) Signature — Frank Geurts — Name (print or type)

(c) Signature — Stephen Semmes — Name (print or type)

(d) Signature — Name (print or type)

Rev. 7/6/16

ABSTRACT

Exclusive Vector Meson Photoproduction in Ultraperipheral Heavy-Ion Collisions at the LHC with the CMS Detector

by

JiaZhao Lin

All nuclear matter consists of tiny particles called quarks and gluons. Gluons become increasingly dominant constituents of nuclear matter when probed at higher energies or smaller Bjorken-x values. A key objective of high-energy nuclear physics is to search for the onset of gluon saturation phenomena in the limit of extreme gluon densities.

Ultraperipheral collisions (UPCs) are collisions of relativistic heavy ions at impact parameters larger than the sum of their nuclear radii. The intense electromagnetic fields generated by relativistic heavy ions can be treated as a flux of linearly polarized, quasi-real photons. Photon-induced vector meson production in UPCs provides a unique and powerful probe of the gluon distribution in nuclei, as the cross section is directly sensitive to the nuclear gluon density.

The J/ψ meson, a bound state of charm and anticharm quarks, is an ideal probe of the gluon density in the nucleus due to its large mass and small size. However, in symmetric UPCs, a two-way ambiguity in determining the photon emitter and the target prevents the extraction of contributions involving high- and low-energy photon-nucleus interactions. This limitation has reduced the capability to probe the small-x regime for the past two decades. The first measurement of coherent charmonium

photoproduction, where the two-way ambiguity is overcome using a forward neutron tagging technique in UPC PbPb collisions at 5.02 TeV, unveils a novel behavior of the nuclear gluon density at small-x.

The $\phi(1020)$ meson lies at the boundary of hard scales between the perturbative and nonperturbative QCD regimes, making it uniquely suited to probe the transition between these two domains. Additionally, the $\phi(1020)$ meson has a larger size than the J/ψ meson, providing enhanced sensitivity to the gluon distribution in the nucleus. However, the significant challenge of detecting extremely low transverse momentum kaons from coherent $\phi(1020)$ meson decays has hindered the measurement of its production in UPCs for decades. The first observation and measurement of exclusive $\phi(1020)$ photoproduction via the $\phi \to \mathrm{K}^+\mathrm{K}^-$ decay channel in PbPb UPCs at 5.36 TeV, using the CMS detector with a new low-p_T reconstruction technique, is presented.

Together, this thesis employs multiple probes of exclusive vector meson production in UPCs to map the gluon distribution in nuclei, study nuclear structure at high energies, and provide new insights into the gluon saturation regime and small-x nuclear gluonic structure. The results challenge the current theoretical understanding at extreme densities, as standard leading-order QCD predictions and saturation/shadowing models fail to describe the data. These findings suggest the presence of strong nuclear effects, such as suppression, although the underlying physics remains unclear.

Acknowledgments

"What you learn from a life in science is the vastness of our ignorance."
— David Eagleman

Several years ago, while participating in an NSF REU program at UIUC, I first learned about the prevalence of imposter syndrome among graduate students—I never thought I would become one of them. It is often said that no one has an easy life in graduate school, and my time has certainly been marked by self-doubt. Neither my work nor I has ever felt quite good enough. But growing as a scientist also means growing as a person and learning to embrace imposter syndrome as part of the process. I hope that the work I have done in this thesis has made a small contribution to the field of nuclear physics.

I would like to express my deepest gratitude to my advisor, Professor Wei Li, for his invaluable guidance and support throughout my graduate studies. Wei is undoubtedly the greatest physicist I have had the privilege to meet. His passion for physics and keen insights have been a constant source of inspiration for me. Wei has taught me that a successful physicist need not be a genius, but rather someone who is willing to work hard and think deeply, rather than quickly. This work would not have been possible without his mentorship and expertise.

I am also grateful to my collaborators and colleagues, whose insights and contributions have been instrumental in shaping this thesis. Zhoudunming Tu was one of my first mentors when I started at Rice. We tried to work on the azimuthal asymmetries in DIS using H1 data. Although nothing came to fruition due to various technical issues, I learned a lot about the mindset required for research. Zaochen Ye contributed immensely to the UPC analysis, and we had countless discussions about

the physics and the analysis. He is a great friend and mentor. I have learned from him both academically and personally; I admire his dedication and work ethic, and I am grateful for the opportunity to work with him. Shuai Yang and Andre Stahl were also instrumental in the analysis. Their work laid the foundation for my own research. Shuai's particular attention to detail, thoughtfulness, and methodical approach to analysis have influenced my own work. Andre's expertise in the field and technical skills have been invaluable in accelerating the analysis. Although I do not have space to mention everyone, I would like to briefly acknowledge a few others: Austin Baty, Yousen Zhang, Parker Gardner, Xiaoyu Liu, Xiao Huang, and Jing Wang.

Finally, I would like to end with an excerpt that I believe captures the essence of what I have learned during my time in graduate school:

> "When I began writing *The Happiness Hypothesis*, I believed that happiness came from within, as Buddha and the Stoic philosophers said thousands of years ago. You'll never make the world conform to your wishes, so focus on changing yourself and your desires. But by the time I finished writing, I had changed my mind: Happiness comes from between. It comes from getting the right relationships between yourself and others, yourself and your work, and yourself and something larger than yourself."
> — Jonathan Haidt

Thank you all for being part of my journey.

Contents

To my family, friends, and

mentors.

Chapter 1

Introduction

The fundamental question of what we are made of and how we interact with the world around us has driven human curiosity for centuries. The ancient Greek philosopher Democritus coined the term *atom* to describe the smallest indivisible unit of matter, believing that the only true reality consists of atoms and void, and that our sensory perceptions are merely illusions.

Over the past few centuries, scientists have made tremendous progress in understanding the nature of matter. The discovery of the electron by J.J. Thomson in 1897, the nucleus by Ernest Rutherford in 1911, and the neutron by James Chadwick in 1932 dissected the atom into the concept of elementary particles and even smaller constituents. By the mid-20th century, advances in accelerator physics and experimental apparatus brought us to the era of high-energy physics, where fundamental particles and their interactions are studied at the smallest scales. Many more particles have been discovered, and their properties have been measured with great precision.

The Standard Model of particle physics was developed to describe the interactions of these particles, and it has been tested to an extraordinary degree of accuracy. In the Standard Model, matter is made up of quarks (q) and leptons (l), which interact through the exchange of force-carrying particles called bosons. Specifically, the strong force is mediated by gluons (g), the electromagnetic force by photons (γ), the weak force by the W and Z bosons, and the Higgs boson (H) provides mass to particles.

Equipped with the world's most powerful particle accelerator, the Large Hadron

Collider (LHC) at CERN, physicists have been able to test the Standard Model to an unprecedented level of precision. The discovery of the Higgs boson at the LHC in 2012 was a triumph for the Standard Model [1, 2]. However, the Standard Model is not a complete theory, leaving many open questions unanswered. Now it is our turn to explore the world of particles. In this thesis, we will explore the world of quarks and gluons, the fundamental constituents of nuclear matter, and examine the surprising phenomena that emerge when probing them at the smallest scales.

1.1 The Structure of Matter

Uncovering the structure of the proton has been a central theme in nuclear physics for over a century. Key insights into the structure of the proton came from electron-proton ($e^{\pm}p$) scattering experiments, where the proton was probed using an electron beam. The general idea is straightforward: use point-like leptons (e.g. $e^{\pm}$, $\mu^{\pm}$) to study the strong interaction of the proton and infer its inner structure.

At low energy, the dominant process is elastic scattering, where the electron scatters off the proton and the proton remains intact. This interaction can be described as the coherent interaction of a virtual photon with the proton. The elastic scattering cross section can be studied to understand the global properties of the proton, such as its charge and magnetic moment. However, at higher energies, the inelastic scattering process becomes dominant, where the electron interacts with the constituents of the proton. These constituents were later identified as quarks and gluons, collectively referred to as partons. The inelastic scattering process can be described by the incoherent interaction of the virtual photon with the partons inside the proton.

Several fixed-target scattering experiments were conducted in the 1960s and 1970s, including the pioneering electron experiment at the Stanford Linear Accelerator Cen-

ter (SLAC) in the 1960s and the muon experiment at CERN in the 1970s. Together, these experiments provided convincing evidence that the proton is composed of point-like constituents. The discovery of quarks resulted from studies of the deep inelastic scattering (DIS) process, while the discovery of gluons came from the observation of three-jet events in e^+e^- annihilation experiments at the PETRA collider at DESY in the 1980s [3]. Two jets corresponded to $q\overline{q}$ pair production, while the third jet provided a clear signature of gluon radiation. Subsequent quantitative studies of the DIS process at the HERA collider in the 1990s further validated the gluon distribution in the proton.

1.2 Quantum Chromodynamics

Quantum Chromodynamics (QCD) is the theory of the strong interaction that describes the interactions between quarks and gluons. Similar to Quantum Electrodynamics (QED), where photons mediate the electromagnetic force between charged particles, QCD is mediated by the exchange of gluons between quarks. However, quarks and gluons carry an additional degree of freedom, called the color charge. The concept of color charge was proposed in the 1960s to introduce an additional quantum number for quarks, resolving apparent violations of the Pauli Exclusion Principle in baryon states within the quark model. Subsequently, studies of hadronic final states in e^+e^- annihilation provided strong evidence for this idea. The observed ratio of hadronic to muonic cross sections, $\sigma(e^+e^- \to q\overline{q} \to \text{hadrons})/\sigma(e^+e^- \to \mu^+\mu^-)$, matched theoretical predictions incorporating three color charges ($N_c = 3$) [4]. This agreement supported the existence of color charge, in which quarks carry one of three colors (red, green, blue), and anti-quarks carry the corresponding anti-colors.

Unlike photons, which couple to electric charge but are electrically neutral, gluons

carry color charge, enabling self-interaction and making QCD a much richer theory than QED. Each gluon carries both a color and an anti-color charge, resulting in a total of eight distinct gluons. Examples of gluon self-interaction include gluon-gluon scattering, the three-gluon vertex, and the four-gluon vertex—features absent in QED. These vertices enable gluon splitting and merging, leading to phenomena such as gluon splitting and gluon fusion. As we will see later, this property of gluons plays a crucial role in the study of the proton structure at high energies.

Two of the most important features of QCD are asymptotic freedom and confinement. In QED, the strength of the electromagnetic force is determined by the coupling constant α_e, which increases with the energy scale due to the vacuum polarization effect. Such an effect can be studied by looking at the precise measurement of the differential cross section for Bhabha scattering, $e^+e^- \to e^+e^-$ [5]. In other words, the production of virtual e^+e^- pairs screens the electric charge, causing the effective QED coupling constant to decrease and asymptotically approach a constant value of $\alpha_e \approx 1/137$ at distances on the order of 10^{-13} m.

In contrast, the strength of the strong force is determined by the coupling constant α_S, which increases as the energy scale decreases:

$$\alpha_S(Q^2) = \frac{12\pi}{(3N_c - N_f)\ln(Q^2/\Lambda^2_{QCD})}, \tag{1.1}$$

where $N_c = 3$ is the number of colors, N_f is the number of flavors, and Λ_{QCD} is the QCD scale parameter. The experimental measurements of α_S as a function of the energy scale Q^2 are shown in Fig. 1.1. As shown, the coupling constant diverges as Q^2 approaches zero. This property, known as asymptotic freedom, implies that quarks and gluons interact weakly at high energies or short distances but strongly at low energies or long distances. As a result, quarks and gluons are confined within hadrons and cannot be observed as free particles, a phenomenon known as confinement.

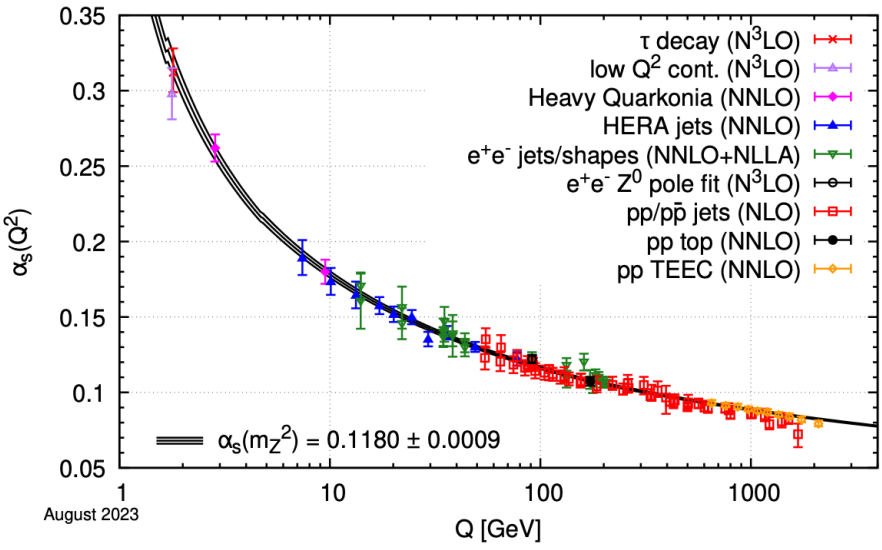

Figure 1.1 : The experimental measurements of the strong coupling constant α_S as a function of the energy scale Q^2 extracted from various experiments. The measurements are consistent with the QCD prediction of the running of the coupling constant. Figure from the Particle Data Group [6].

At high energies, quarks and gluons behave as free particles, allowing perturbative QCD to describe their interactions. However, at low energies, quarks and gluons are confined within hadrons, and their interactions are strong, causing perturbative QCD to break down. Quantitatively, quarks and anti-quarks interact strongly only when separated by a distance on the order of 1 fm (10^{-15} m). At larger separations, the energy stored in the color field becomes sufficient to create a new $q\bar{q}$ pair, ensuring that the original quarks are never observed as free particles.

1.3 Kinematics

To further the discussion, we introduce several kinematic variables commonly used to describe the $e^{\pm}p \to e^{\pm}X$ process, where p_1 and p_3 are the four-momenta of the

incident and scattered lepton, respectively, and p_2 and p_4 are the four-momenta of the incident and scattered proton, respectively. The squared four-momentum transfer, Q^2, is defined as the negative of the squared four-momentum of the virtual photon:

$$Q^2 = -q^2, \tag{1.2}$$

where q is the four-momentum of the virtual photon.

Bjorken x is defined as the fraction of the proton's momentum carried by the struck parton:

$$x = \frac{Q^2}{2p_2 \cdot q}. \tag{1.3}$$

Inelasticity, y, is defined as the fraction of the energy of the incident lepton transferred to the hadronic system:

$$y = \frac{p_2 \cdot q}{p_2 \cdot p_1} = 1 - \frac{E_3}{E_1}. \tag{1.4}$$

The center-of-mass energy, W, is the invariant mass of the hadronic system:

$$W = \sqrt{(p_2 + q)^2}. \tag{1.5}$$

The Mandelstam variable, s, represents the squared center-of-mass energy of the colliding system:

$$s = (p_1 + p_2)^2 = (p_3 + p_4)^2. \tag{1.6}$$

The momentum transfer, t, is the squared four-momentum transfer between the initial and final state proton:

$$t = (p_2 - p_4)^2. \tag{1.7}$$

The variables Q^2, x, and s are simply related in the approximation that the masses are negligible compared to the momenta:

$$Q^2 \approx sxy. \tag{1.8}$$

Thus, small values of x correspond to larger values of energy, $s \approx Q^2/(xy)$.

In elastic scattering, only one degree of freedom is present, and the collision system is fully described by measuring the scattering angle of the electron. In DIS, two degrees of freedom are present: the scattering angle of the electron and the energy of the scattered electron. Therefore, a minimum of two kinematic variables is needed to describe the process. The variables Q^2 and x are the most commonly used variables to describe the DIS process.

In modern high-energy physics experiments, experimental measurements need to be presented in a consistent way such that they are Lorentz invariant. However, velocity and direction are not Lorentz invariant. Instead, the rapidity, y, is used to describe the velocity and direction of the particles. The rapidity is defined as:

$$y = \frac{1}{2} \ln \left(\frac{E + p_z}{E - p_z} \right). \tag{1.9}$$

Rapidity is zero when the particle travels in the transverse direction relative to the beam axis and approaches infinity when the particle travels in the beam direction. Although rapidity itself is not Lorentz invariant, the rapidity difference, $\Delta y = y_1 - y_2$, is Lorentz invariant. For relativistic particles, the rapidity can be approximated by the pseudo-rapidity, η, which is defined as:

$$\eta = -\ln \left(\tan \left(\frac{\theta}{2} \right) \right), \tag{1.10}$$

where θ is the polar angle of the particle with respect to the beam axis.

The transverse momentum of a particle, p_{T}, relative to the beam axis is also Lorentz invariant under longitudinal boosts. It is defined as:

$$p_{\mathrm{T}} = \sqrt{p_x^2 + p_y^2}. \tag{1.11}$$

Throughout this thesis, natural units are used for numerical calculations, where $\hbar = c = 1$, with the following conversion factors:

- 1 [Length][Energy] $= \hbar c = 0.197\,\text{GeV} \cdot$ fm.
- 1 [Length][Time]$^{-1} = c = 3 \times 10^{23}$ fm.

1.4 HERA Experiments

The Hadron Elektron Ringanlage (HERA) at the DESY laboratory in Hamburg, Germany, was the first electron-proton collider. It operated from 1992 to 2007, colliding electrons and positrons (collectively referred to as electrons) with protons at a center-of-mass energy of up to $W_{\gamma\text{p}} \approx 320\,\text{GeV}$. The collider detectors at H1 and ZEUS at the HERA collider at DESY provided a wealth of information on the parton distribution functions (PDFs) in the proton. PDFs represent the probability distributions of partons in the proton as a function of the momentum fraction x and the energy scale Q^2. Fig. 1.2 shows the PDFs in the proton extracted from the combined HERA data at a scale of $Q^2 = 10\,\text{GeV}^2$. At high x values, the valence quarks dominate, with the up quark density xu_v being twice as large as the down quark density xd_v. However, the sea quark density xS and the gluon density xG grow exponentially with decreasing x values. In particular, xG dominates at small x values.

When the PDFs at the given x and Q^2 values are known, the Balitsky-Fadin-Kuraev-Lipatov (BFKL) theory can be used to predict the behavior of the gluon density at different x values at the same Q^2 values. Similarly, the Dokshitzer-Gribov-Lipatov-Altarelli-Parisi (DGLAP) theory predicts the behavior of the gluon density at different Q^2 values for the same x values. These two theories are used to describe the evolution of the PDFs in the linear regime, where gluons evolve independently of each other. A schematic of the behavior of xG at small x values for different resolution scales, $Q^2 = 5$, 20, and $200\,\text{GeV}^2$, is shown in Fig. 1.3. In general, the gluon density

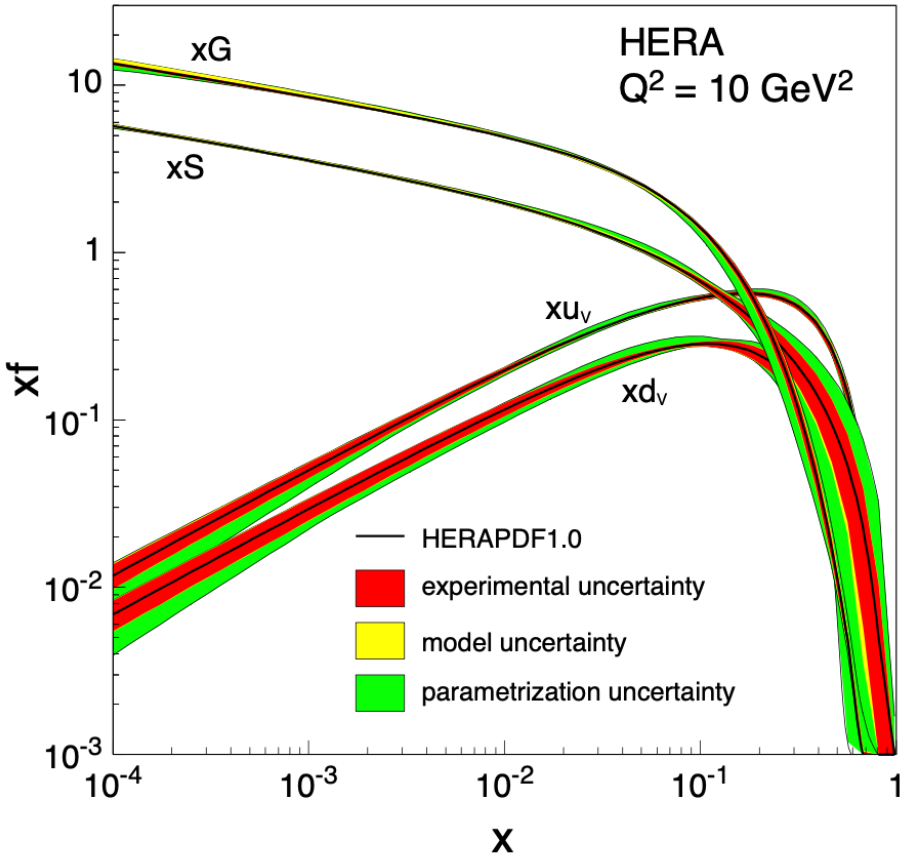

Figure 1.2 : The parton distribution functions (PDFs) in the proton as a function of the momentum fraction x at the scale $Q^2 = 10\,\mathrm{GeV}^2$ are shown. In the figure, the xu_v and xd_v are the valence up and down quark densities, respectively, while xS and xG are the sea quark and gluon densities, respectively. The gluon density is shown to dominate at small x values. Figure from the HERA experiments [7].

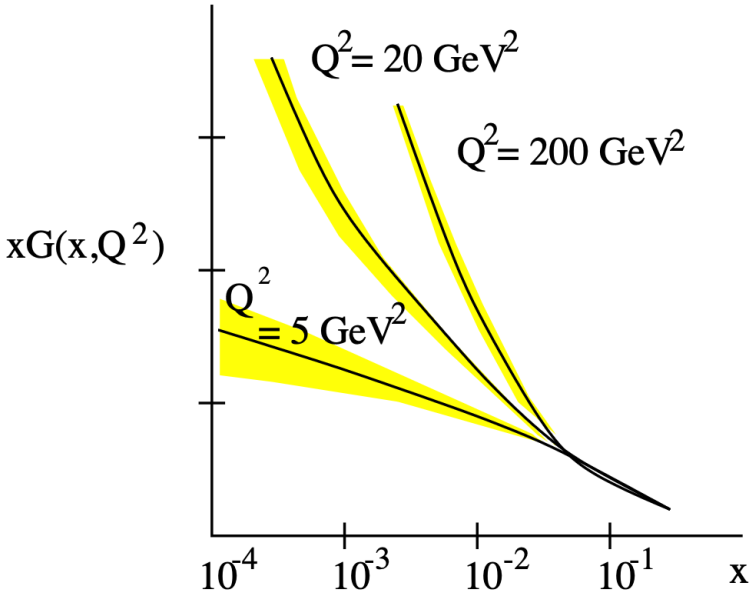

Figure 1.3 : A schematic illustration of the gluon density xG in the proton as a function of the momentum fraction x at different resolution scales $Q^2 = 5, 20, 200\,\mathrm{GeV}^2$ is shown. An increase in the resolution scale Q^2 leads to an increase in the gluon density at small x values. Figure from [8].

increases with the resolution scale Q^2 and increases with the decrease in x values.

Physically, this increase cannot continue indefinitely, and the gluon density must eventually saturate. The saturation scale, Q_S^2, is the scale at which the gluon density becomes so large that the gluons begin to overlap and interact with each other. The saturation scale can be approximated as:

$$Q_S^2 \sim A^{1/3} \left(\frac{1}{x}\right)^{\lambda} \approx \left(\frac{A}{x}\right)^{1/3}, \tag{1.12}$$

where A is the mass number of the nucleus, and λ is the exponent with best theoretical estimates of $\lambda = 0.2 - 0.3$ [7].

This leads to the phenomenon of gluon saturation [9, 10], where the gluon recombination and gluon splitting processes are in balance. The PDFs' evolution going

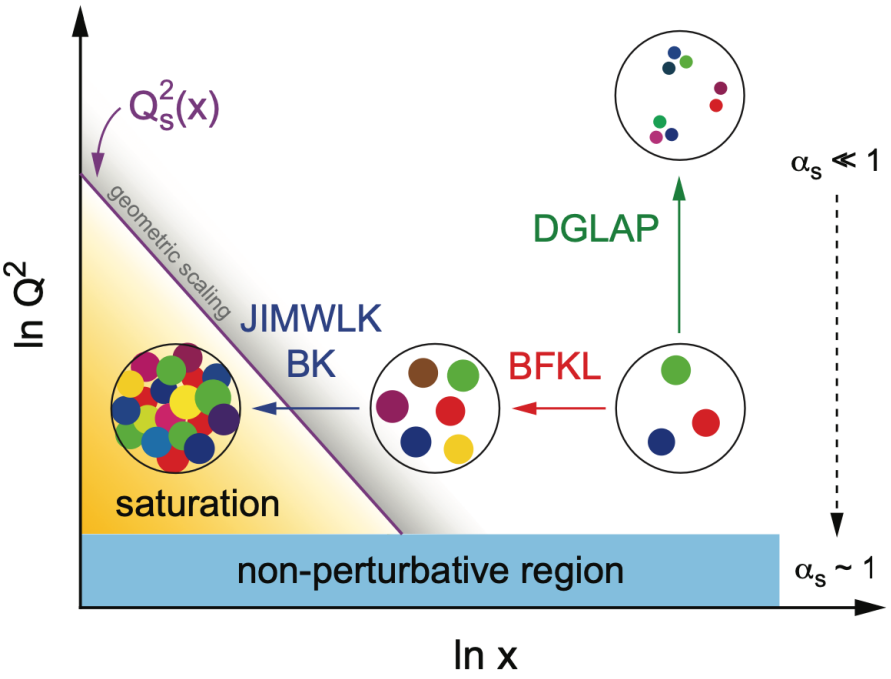

Figure 1.4 : A schematic map of the gluon density in the proton as a function of the momentum fraction x and the resolution scale Q^2 is shown. The Q_S^2 is the saturation scale, delineating the region where the gluon density saturates. At low Q^2 values, the strong coupling constant $\alpha_S \sim 1$, indicating the non-perturbative regime. At high Q^2 values, the strong coupling constant $\alpha_S \ll 1$, indicating the perturbative regime. Figure from [7].

into the saturation regime is provided by the Balitsky-Kovchegov (BK) and Jalilian-Marian-Iancu-McLerran-Weigert-Leonidov-Kovner (JIMWLK) equations, where gluons evolve non-linearly and interact with each other. Fig. 1.4 shows a schematic map of the gluon density in the proton as a function of x and Q^2. As Q^2 decreases, the x values at which the gluon density saturates increase.

Two types of processes were studied at HERA: the neutral-current (NC) process, where a photon or, at higher Q^2, a Z boson is exchanged, and the charged-current (CC) process, where a $W^{\pm}$ boson is exchanged. NC processes can be identified by energy deposits in the calorimeter consistent with an electron, matched with a track in

the tracking system, and back-to-back hadronic jets. CC processes can be identified by significant missing transverse energy in the event, consistent with an escaping neutrino. For the case of photon exchange in NC events, the possible processes can be further divided into two sub-categories based on the photon virtuality, Q^2: the photoproduction process, where $Q^2 \approx 0\,\mathrm{GeV}^2$, and the DIS process, where $Q^2 \gg 1\,\mathrm{GeV}^2$.

In this thesis, much of the discussion will focus on the photoproduction processes, where the photon virtuality is small, $Q^2 \ll 1\,\mathrm{GeV}^2$. The HERA experiment provided an ideal environment for the study of the hadronic final state over a wide range of W, Q^2, and x values. Both H1 and ZEUS detectors were asymmetric, with the electron beam coming from the left and the proton beam coming from the right. Due to the higher incoming energy of the proton beam, there is significantly greater particle multiplicity from hard scattering, with the proton remnant moving in the forward direction and the electron remnant moving in the backward direction. This allows for a forward-backward asymmetry in the detector instrumentation, which can be used to study the properties of the final state particles. Both detectors had forward proton and neutron taggers to detect low-angle diffractive production. In particular, their rear detectors had calorimeters placed at several points along the direction of the outgoing electron beam at distances up to 40 m from the interaction point. These were used to tag the electrons in photoproduction events over a narrower range in Q^2 and y. These features provided an ideal environment for the study of the exclusive final state photoproduction, where the scattered electron was either undetected or detected in the rear calorimeters at a very small scattering angle.

The HERA experiments pioneered the energy dependence of the exclusive vector meson (VM) photoproduction cross section, which is sensitive to the gluon density

in the proton at small x values. Perhaps the most precise measurements of the photoproduction data come from studies of decades of products of the two-prong decay of the VMs (e.g. $\rho \to \pi^+\pi^-$, $\phi \to \mathrm{K}^+\mathrm{K}^-$, $\mathrm{J}/\psi \to \mu^+\mu^-$).

A compilation of photoproduction for exclusive VM production as a function of the center-of-mass energy W is shown on the left of Fig. 1.5. The measured cross sections follow a power-law dependence, $\sigma \propto W^{\delta}$, where the exponent δ depends on the mass of the VM. For light VMs (e.g. ρ, ω, ϕ), the cross sections rise slowly with $\delta \approx 0.22$, while for heavy VMs (e.g. J/ψ, $\psi(2\mathrm{S})$, Υ), the cross sections rise rapidly with $\delta > 0.8$. These observations suggest that the production mechanism changes with the mass of the VM. In fact, the steepening of the dependence on W for the heavy VMs can be interpreted as the scale dependence of the gluon density at low x. The transition from soft to hard perturbative behavior can be seen more clearly by mapping the values of δ to the values of $Q^2 + M_{\mathrm{VM}}^2$, where M_{VM} is the mass of the VM, as shown on the right of Fig. 1.5. The figure includes data from both exclusive VM production and deeply virtual Compton scattering (DVCS) processes, $\gamma^*\mathrm{p} \to \gamma\mathrm{p}$, from the HERA experiments. The increase in δ with $Q^2 + M_{\mathrm{VM}}^2$ indicates that $Q^2 + M_{\mathrm{VM}}^2$ provides the appropriate hard scale, allowing the process to be described by perturbative QCD when $Q^2 + M_{\mathrm{VM}}^2$ is large, on the order of a few $10\,\mathrm{GeV}^2$.

In QCD models, the high-energy photon can fluctuate into a $\mathrm{q}\overline{\mathrm{q}}$ pair (a color dipole) before interacting with the proton by exchanging two gluons and emerging as a VM. Thus, the cross section of the exclusive VM photoproduction is sensitive to the square of the gluon density. The size of the color dipole is determined by the virtuality of the photon, Q^2, and the mass of the VM, M_{VM}. This can be seen by measuring the differential cross sections as a function of $|t|$. The clean environment of the exclusive final state enabled precise measurements of $|t|$, which is sensitive to the

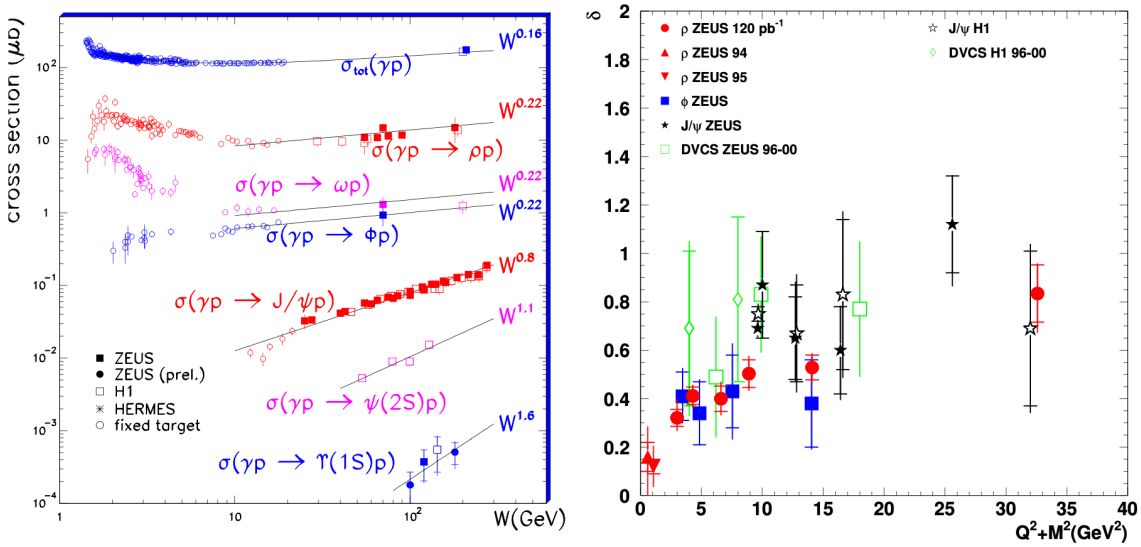

Figure 1.5 : A compilation of the exclusive VMs photoproduction cross section as a function of the center-of-mass energy W is shown on the left. The measured cross sections exhibit a power-law dependence, $\sigma \propto W^{\delta}$, where the power δ depends on the mass of the VM. The extracted δ as a function of the scale $Q^2 + M_{\mathrm{VM}}^2$ is shown on the right using data from both DVCS and exclusive VM production. Figure from the HERA experiments [11].

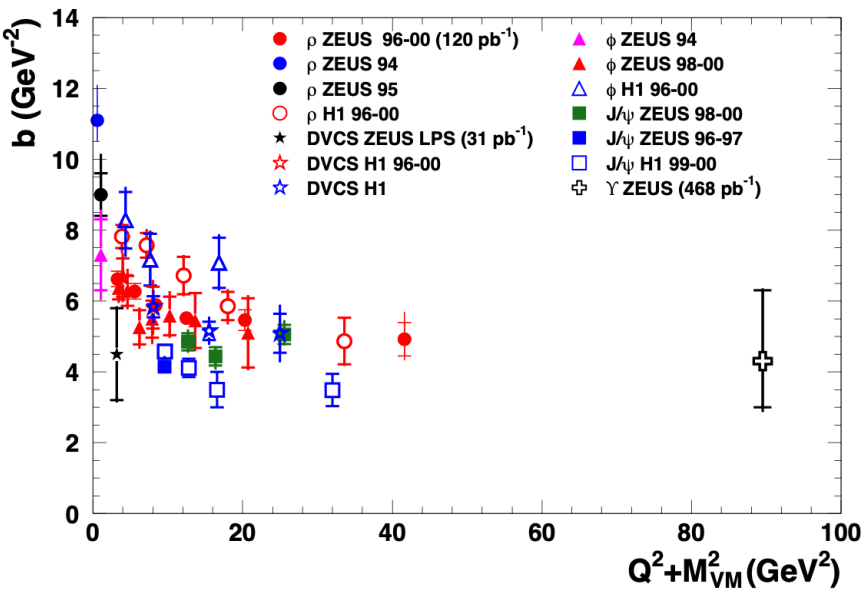

Figure 1.6 : A compilation of the HERA measurements of the slope parameter b as a function of the scale $Q^2 + M^2_{\rm VM}$ is shown. The asymptotic behavior of the slope parameter b is consistent with the size of the proton, $b \approx 4\,{\rm GeV}^{-2}$, for the heavy VMs. Figure from the ZEUS experiments [13].

transverse spatial distribution of partons in the proton. As can be seen in Fig. 1.6, the $|t|$ dependence of the differential cross section can be described by an exponential function, $\exp(-b|t|)$, where b is the slope parameter related to the transverse size of the interaction region. When the size of the color dipole is small (e.g. J/ψ, Υ), b should be approximately equal to that expected from the size of the proton. Interestingly, measurements at high $Q^2 + M^2_{\rm VM}$ suggest an effective proton size of approximately 0.6 fm, smaller than the 0.8 fm expected from the proton's electromagnetic form factor [12].

These measurements have suggestively shown that the exclusive J/ψ photoproduction is a powerful probe of the gluon density in the proton at small x values, being a reasonably large scale and experimentally clean.

1.5 The Big Picture

This thesis presents the first measurement of coherent J/ψ photoproduction, where a forward neutron tagging technique was used to disentangle the two-way ambiguity in determining the photon emitter and the target in ultraperipheral PbPb collisions at $\sqrt{s_{_{\mathrm{NN}}}} = 5.02\,\mathrm{TeV}$. The results provide new insights into the nuclear gluon density at small x values and reveal novel behavior in this regime.

Building upon the success of the J/ψ photoproduction study, the thesis also presents the first observation and measurement of coherent $\phi(1020)$ photoproduction via the $\phi \to \mathrm{K}^+\mathrm{K}^-$ decay channel in ultraperipheral PbPb collisions at $\sqrt{s_{_{\mathrm{NN}}}} = 5.36\,\mathrm{TeV}$. This offers new insights into the high-energy nuclear gluonic structure at the boundary between the perturbative and nonperturbative QCD regimes.

The thesis is organized as follows. In Ch. 1, we provided a brief overview of the structure of matter and the theory of QCD. In Ch. 2, we will discuss the concept of ultraperipheral collisions and how they can be used to study the gluon distribution in nuclei. In Ch. 3, we will discuss the Compact Muon Solenoid experiment at the LHC and how it is used to study the properties of the particles produced in high-energy collisions. In Ch. 4, we will discuss the production of the J/ψ meson in ultraperipheral collisions, where the nucleon was probed at an unprecedentedly high energy and revealed a novel behavior of the nuclear gluon density. In Ch. 5, we will discuss the first observation and studies of exclusive $\phi(1020)$ photoproduction in ultraperipheral collisions, providing new insights into the high-energy nuclear gluonic structure at a critical scale. Finally, in Ch. 6, we summarize the results and discuss their implications for our understanding of the structure of nuclear matter.

Chapter 2

Ultraperipheral Collisions

From Eq. 1.12, the saturation scale, Q_S^2, is inversely proportional to the Bjorken-x value and directly proportional to the nuclear mass number, A. Lower values of x can be achieved by increasing the center-of-mass energy, while higher nuclear mass numbers can be achieved by colliding heavier ions.

At the energies available at modern-day colliders such as the LHC (and the future Electron-Ion Collider (EIC) [7]), one way to probe the gluon saturation regime is by colliding heavy ions at high energies, where the gluon density in the nucleus is expected to be enhanced by a factor of $\sim A^{1/3}$ compared to the proton.

2.1 Physics of Ultraperipheral Collisions

A fast-moving charged particle generates an electric field pointing radially outward and magnetic fields circling it. At relativistic speeds, the electric field becomes Lorentz-contracted in the direction of motion, causing it to preferentially point in the transverse direction. In 1924, Enrico Fermi proposed that moving electromagnetic fields from relativistic charged particles could act as a source of high-energy photons [14]. At the HERA collider, the proton is probed by the photon emitted by the electron. Similarly, in ultraperipheral collisions (UPCs), the nucleus can be probed by photons emitted by heavy ions.

UPCs occur when relativistic heavy ions collide at impact parameters (b) greater

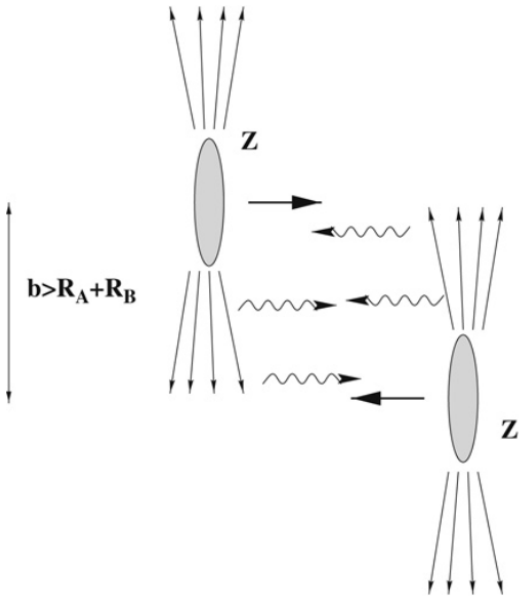

Figure 2.1 : Schematic diagram of ultraperipheral collisions (UPCs) of relativistic heavy ions. Figure from [17].

than the sum of their nuclear radii, $b > R_A + R_B$. Consequently, the ions do not interact hadronically. Instead, the ions interact electromagnetically via the exchange of virtual photons. These intense electromagnetic fields, proportional to the square of the charge of the colliding ions (Z^2), can be treated as a flux of linearly polarized quasi-real photons [15, 16]. A schematic diagram of the UPCs is shown in Fig. 2.1.

Because photons emitted by heavy ions are radiated by the entire nucleus, the minimum photon wavelength must exceed the nuclear radius. In the transverse plane, the uncertainty principle sets an upper limit on the transverse momentum of the photon:

$$p_{\mathrm{T}} < \frac{1}{R_A}. \tag{2.1}$$

In the longitudinal direction, the ions are boosted by the Lorentz factor, γ. The

photon longitudinal momentum, p_{L}, is limited to:

$$p_{\mathrm{L}} < \frac{\gamma}{R_A}. \tag{2.2}$$

For relativistic heavy ions, the Lorentz factor is large. It can be calculated as:

$$\gamma = \frac{E}{m} = \frac{A \cdot \sqrt{s_{_{\mathrm{NN}}}}/2}{A \cdot m_{\mathrm{N}}} = \frac{\sqrt{s_{_{\mathrm{NN}}}}}{2m_{\mathrm{N}}}. \tag{2.3}$$

For PbPb collisions at Run 2 energy $\sqrt{s_{_{\mathrm{NN}}}} = 5.02\,\mathrm{TeV}$, we have $\gamma \approx 2697$. Therefore, the photon transverse momentum is small compared to the longitudinal momentum, $p_{\mathrm{T}} \ll p_{\mathrm{L}}$.

From the energy-momentum relation, $E^2 = p^2 + m^2$, the energy of the photon can be approximated as:

$$E^2 = p_{\mathrm{T}}^2 + p_{\mathrm{L}}^2 \approx p_{\mathrm{L}}^2. \tag{2.4}$$

Thus, the photon virtuality is limited by the nuclear radius:

$$Q^2 = -q^2 = -(E^2 - p^2) = p_{\mathrm{T}}^2 + p_{\mathrm{L}}^2 - E^2 \approx p_{\mathrm{T}}^2 < 1/R_A^2. \tag{2.5}$$

For Pb ions with radius $R_{\mathrm{Pb}} \approx 7\,\mathrm{fm}$, we have a limit of:

$$Q^2 \approx p_{\mathrm{T}}^2 < \left(\frac{197\,\mathrm{MeV}\cdot\,\mathrm{fm}}{7\,\mathrm{fm}}\right)^2 \approx 0.8\,\mathrm{GeV}^2. \tag{2.6}$$

Because the photon virtuality is small, it can be treated as a quasi-real photon. The transverse linear polarization of photons in UPCs has been experimentally verified through the observation of angular modulation in $\mathrm{e}^+\mathrm{e}^-$ pair production [18].

2.2 Photon Flux in UPC

The electromagnetic field of relativistic heavy ions traveling along the longitudinal direction is described by [19]:

$$\begin{aligned} E_{\mathrm{L}}(t,b) &= -\frac{Ze\gamma vt}{(b^2+\gamma^2v^2t^2)^{3/2}}, \\ E_{\mathrm{T}}(t,b) &= -\frac{Ze\gamma \vec{b}}{(b^2+\gamma^2v^2t^2)^{3/2}}, \\ B_{\mathrm{L}}(t,b) &= 0, \\ B_{\mathrm{T}}(t,b) &= v/c \cdot E_{\mathrm{T}}, \end{aligned} \tag{2.7}$$

where L and T denote the longitudinal and transverse directions, respectively, e is the elementary charge, and t is the time.

The Fourier transform of the time-dependent fields to frequency-dependent fields gives:

$$\begin{aligned} E_{\mathrm{L}}(\omega,b) &= \sqrt{\frac{2}{\pi}}\frac{Ze\omega}{\gamma^2v^2}K_0(b\omega/\gamma v), \\ E_{\mathrm{T}}(\omega,b) &= \sqrt{\frac{2}{\pi}}\frac{Ze\omega}{\gamma v^2}K_1(b\omega/\gamma v), \\ B_{\mathrm{L}}(\omega,b) &= 0, \\ B_{\mathrm{T}}(\omega,b) &= v/c \cdot E_{\mathrm{T}}, \end{aligned} \tag{2.8}$$

where K_0 and K_1 are the modified Bessel functions.

$E_{\mathrm{T}}(\omega,b)$ and $B_{\mathrm{T}}(\omega,b)$ can be treated as a pulse of plane-polarized radiation (P_{L}) propagating along the longitudinal direction. Likewise, $E_{\mathrm{L}}(\omega,b)$ and $B_{\mathrm{L}}(\omega,b)$ can be treated as radiation (P_{T}) propagating along the transverse direction [20].

The energy per unit area per unit time carried by the electromagnetic field is described by the Poynting vector:

$$\vec{S} = \frac{c}{4\pi}|\vec{E}\times\vec{B}|. \tag{2.9}$$

Their energies per unit area per unit frequency are given by:

$$\begin{aligned} I_{\mathrm{L}}(\omega, b) &= \frac{c}{2\pi}|E_{\mathrm{T}}(\omega, b)|^2, \\ I_{\mathrm{T}}(\omega, b) &= \frac{c}{2\pi}|E_{\mathrm{L}}(\omega, b)|^2, \\ I(\omega, b) &= I_{\mathrm{L}}(\omega, b) + I_{\mathrm{T}}(\omega, b) \\ &= \frac{cZ^2e^2\omega^2}{\pi^2\gamma^2v^4}\left[K_1^2(b\omega/\gamma v) + \frac{1}{\gamma^2}K_0^2(b\omega/\gamma v)\right]. \end{aligned} \tag{2.10}$$

This expression shows that the intensity traveling in the transverse direction is suppressed by a factor of $1/\gamma^2$ compared to the intensity traveling in the longitudinal direction. When $\gamma \gg 1$, the field acts over a very short time interval:

$$\Delta t \approx \frac{b}{\gamma c}. \tag{2.11}$$

This puts a limit on the maximum photon energy:

$$\begin{aligned} E_{\max} &< \hbar/\Delta t = \gamma\hbar c/b = \gamma\hbar c/2R_A \\ &< \frac{\hbar c}{4m_{\mathrm{N}}R_A} \cdot \sqrt{s_{_{\mathrm{NN}}}}. \end{aligned} \tag{2.12}$$

For PbPb collisions with $R_{\mathrm{Pb}} \approx 7\,\mathrm{fm}$, the maximum photon energy is $E_{\max} < 0.75\% \cdot \sqrt{s_{_{\mathrm{NN}}}}$, which corresponds to 38 GeV at $\sqrt{s_{_{\mathrm{NN}}}} = 5.02\,\mathrm{TeV}$. For pp collisions with $R_{\mathrm{p}} \approx 1\,\mathrm{fm}$, the maximum photon energy is $E_{\max} < 5\% \cdot \sqrt{s_{_{\mathrm{NN}}}}$, which corresponds to 650 GeV at $\sqrt{s_{_{\mathrm{NN}}}} = 13\,\mathrm{TeV}$.

To calculate the energy in the target rest frame, we can take the average of the relationship between the boosted factor in the lab frame (γ) and the target rest frame (γ^*): $\gamma^* = 2\gamma^2 - 1$.

$$E^*_{\max} < \frac{\hbar c}{2R_A} \cdot \left(\frac{\sqrt{s_{_{\mathrm{NN}}}}^2}{2m_{\mathrm{N}}^2} - 1\right). \tag{2.13}$$

We have $E^*_{\max} < 200\,\mathrm{TeV}$ for PbPb collisions and $E^*_{\max} < 9.5\,\mathrm{PeV}$ for pp collisions. Finally, the maximum center-of-mass energy ($W^{\max}_{\gamma\mathrm{p}}$) of the photon-proton system is

given by:

$$W_{\gamma \mathrm{p}}^{\max} = \sqrt{m_{\mathrm{N}}^2 + 2 m_{\mathrm{N}} E_{\max}^*}. \tag{2.14}$$

This gives $W_{\gamma \mathrm{N}}^{\mathrm{Pb}} < 600\,\mathrm{GeV}$ for PbPb collisions and $W_{\gamma \mathrm{p}} < 4\,\mathrm{TeV}$ for pp collisions.

The number of equivalent photons per unit area per unit frequency is obtained by considering their equivalent energy:

$$\begin{aligned} I(\omega, b) d\omega &= \hbar\omega \cdot N(\hbar\omega, b) d(\hbar\omega), \\ N(\hbar\omega, b) &= \frac{1}{\hbar^2 \omega} I(\omega, b). \end{aligned} \tag{2.15}$$

Putting everything together and expressing in natural units, the number of equivalent photon flux in UPCs depends on the photon energy (k) and the impact parameter (b) [21]:

$$N(k, b) = \frac{Z^2 \alpha k^2}{\pi^2 \gamma^2 \beta^4} \left[K_1^2(x) + \frac{1}{\gamma^2} K_0^2(x) \right], \tag{2.16}$$

where α is the fine-structure constant, β is the velocity of the ions in units of the speed of light, K_0 and K_1 are the Bessel functions, and $x = kb/\gamma\beta$.

Integrating over the impact parameter and excluding the hadronic interaction, the photon flux is given by:

$$N(k) = \int db N(k, b) P_{0\mathrm{had}}(b), \tag{2.17}$$

where $P_{0\mathrm{had}}(b)$ is the probability that the ions do not interact hadronically at impact parameter b.

Compared to pp collisions, UPCs offer several advantages for studying photonuclear interactions:

- Large photon flux proportional to Z^2, compensating for the lower luminosity of heavy ion beams compared to the proton beam.

- Reduced photon virtuality limited by the nuclear radius.
- Possibility of multiphoton exchange, allowing for tagging of the photon emitter and the target.

2.3 Vector Meson Photoproduction

A photon, being a massless particle, can fluctuate into other particles through emission and reabsorption processes. It transfers its quantum numbers, $J^{PC} = 1^{--}$, to the target, resulting in the production of vector mesons (VMs) such as ρ, ω, ϕ, J/ψ, and Υ. The fluctuated $q\overline{q}$ pair interacts with the target nucleus via gluon exchange and emerges as real VMs in the final state. The lifetime of the photon fluctuating into a VM is very short, as determined by the energy-time uncertainty principle, $\Delta E \Delta t \approx \hbar$, and is given by

$$\Delta t \approx \frac{\hbar}{\sqrt{m_{\mathrm{VM}}^2 c^4 + Q^2 c^2}} \approx \frac{\hbar}{m_{\mathrm{VM}} c^2}. \tag{2.18}$$

In DIS, gluon distributions are not directly accessible because gluons do not carry electric or weak charges. However, in VM photoproduction, gluon distributions can be probed directly through the coupling of the photon-fluctuated $q\overline{q}$ pair, with transverse separation r, to the gluon density in the target nucleus [22, 21]. At small r, the photoproduction cross section can be described perturbatively. At larger r, the cross section is sensitive to any low-x saturation of the gluon density. Because gluons carry a color charge, two-gluon exchange is required to maintain color neutrality. A schematic diagram of VM photoproduction in PbPb UPCs is shown in Fig. 2.2.

In high-energy QCD, exclusive VM production can be factorized into the product of the photon wavefunction, the VM wavefunction, and the generalized parton distribution function (GPD) of the target nucleus. The interaction of the dipole with the

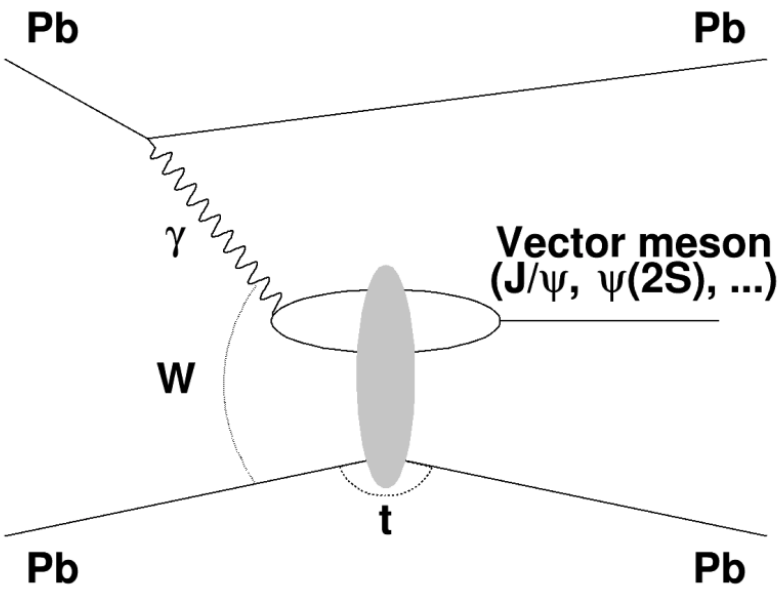

Figure 2.2 : Schematic diagram of VM photoproduction in PbPb UPCs. The shaded area represents the gluon exchange between the photon-fluctuated $q\overline{q}$ pair and the target nucleus. Figure from [23].

target nucleus is described by the area occupied by the dipole in the transverse plane in the target nucleus. In lowest-order pQCD, the forward scattering cross section is proportional to the square of the gluon density in the target nucleus:

$$\frac{\mathrm{d}\sigma(\gamma A \to VA)}{\mathrm{d}t}\Big|_{t=0} \propto \left(x g_A(x, \bar{Q}^2)\right)^2, \tag{2.19}$$

where $g_A(x, \bar{Q}^2)$ is the gluon density in the nucleus, $\bar{Q}^2 = (Q^2 + m_{\mathrm{VM}}^2)/4$ is the mass scale used to evaluate the gluon distribution, and Q^2 is the photon virtuality. The factor of 4 in the denominator is due to the two-gluon exchange, with each gluon assumed to carry half of the virtuality. Although the gluon density is squared to account for the two-gluon exchange, the two gluons do not necessarily have the same x value. In fact, the two gluons can have significantly different x values, with $x_1 \gg x_2$. However, the higher-x gluon is found to be the dominant contribution,

and the Bjorken-x of the dominant gluon can be calculated as in Eq. 2.32, as long as $x_1 \gg x_2$ [21].

The $\gamma A \to VA$ cross section can be expressed in terms of the observed $\gamma \mathrm{p} \to V\mathrm{p}$ cross sections. In particular, the observed $\gamma \mathrm{p} \to V\mathrm{p}$ cross sections were found to be well described by [24]:

$$\left.\frac{\mathrm{d}\sigma(\gamma \mathrm{p} \to V\mathrm{p})}{\mathrm{d}t}\right|_{t=0} = b_V \left(X \cdot W_{\gamma\mathrm{p}}^{\epsilon} + Y \cdot W_{\gamma\mathrm{p}}^{-\eta}\right), \tag{2.20}$$

where the constants b_V, X, Y, ϵ, and η are determined from the experimental data. In this expression, the X and ϵ terms represent Pomeron exchange, while the Y and η terms represent meson exchange. The Pomeron is a colorless object representing the exchange of two gluons, whereas meson exchange involves the exchange of a meson between the photon and the target proton. Since the processes contributing to the total cross section have very small p_{T}, the Pomeron is often referred to as the soft Pomeron and is responsible for the rise of the cross section with energy for light VMs. From Fig. 1.5, it can be seen that the Pomeron exchange term is well described by $\epsilon \approx 0.22$, as expected from the soft Pomeron exchange. For heavy VMs, the meson exchange is suppressed due to the large mass of the VMs, and the reaction occurs only through Pomeron exchange with $\epsilon > 0.22$.

The total cross section can be factorized into two components: the forward scattering amplitude and the form factor. In other words, the cross section contains two parts: the part that depends on the dynamics of the interaction and the part that depends on the spatial structure of the nucleus. Therefore, an integral over the form factor is required to obtain the total cross section:

$$\sigma(\gamma A \to VA) = \left.\frac{\mathrm{d}\sigma(\gamma A \to VA)}{\mathrm{d}t}\right|_{t=0} \int_{t_{\mathrm{min}}}^{\infty} \mathrm{d}t \left|F(t)\right|^2, \tag{2.21}$$

where $F(t)$ is the nuclear form factor, and t_{min} is the minimum value of t that can be

probed in the experiment.

For protons, the form factor is derived from the Fourier transform of the charge distribution and is well described by an exponential form, as observed in the HERA data:

$$|F(t)|^2 = \exp(-b|t|). \tag{2.22}$$

For heavy ions, the nucleon distribution is typically modeled using the Woods-Saxon distribution:

$$\rho(r) = \frac{\rho_0}{1 + \exp((r - R)/a)}, \tag{2.23}$$

where R is the nuclear radius, a is the skin thickness, and ρ_0 is the central density. Since the Fourier transform of the Woods-Saxon distribution lacks an analytic form, the form factor is often approximated as a convolution of a hard-sphere form factor with a Yukawa potential [25].

VM photoproduction, $\gamma A \to VA$, can occur either coherently or incoherently. In coherent production, the photon interacts with the entire nucleus. This puts a limit on the wavelength and transverse momentum of the photon, as shown in Eq. 2.6, to the order of $p_{\mathrm{T}} \sim 30\,\mathrm{MeV}$.

In incoherent production, the photon interacts with a single nucleon in the nucleus. Since the nucleon is much smaller than the heavy ion, the photon can have a much larger transverse momentum. The transverse momentum of the photon is typically on the order of $p_{\mathrm{T}} \sim 200\,\mathrm{MeV}$. Incoherent production is typically accompanied by nuclear breakup and produces forward neutrons, which can result in the VM having an even higher average transverse momentum above 1 GeV. Thus, coherent and incoherent VM production can be distinguished by the clear difference in the transverse momentum of the produced vector mesons.

In this thesis, we focus on the exclusive reaction $A + A \to A + A + V$, where the

VM is produced in the final state. This reaction proceeds via photon-Pomeron or photon-meson interactions.

The photoproduction cross section is expressed as a convolution of the photonuclear cross section and the photon flux:

$$\sigma_{\mathrm{VM}} = \int d\omega N(\omega)\sigma_{\gamma A\to VA}(\omega), \tag{2.24}$$

where $N(\omega)$ is the photon flux, and $\sigma_{\mathrm{VM}}(\omega)$ is the photonuclear cross section.

2.4 UPC Kinematics

In this section, we derive the relationship between the rapidity (y) of the produced VM, the photon energy (ω), the Bjorken-x, and the center-of-mass energy of the γp system ($W_{\gamma\mathrm{p}}$).

Consider the lab frame where the photon scatters off the proton to produce a VM, and let the 4-momentum be:

$$\begin{aligned} p_{\mathrm{p}} &= (E_{\mathrm{p}}, 0, 0, p_{\mathrm{p}}), \\ p_{\mathrm{VM}} &= (E_{\mathrm{VM}}, 0, 0, p_z), \end{aligned} \tag{2.25}$$

where the p_{T} of the VM is ignored in this calculation.

To derive the relationship between ω and y, we first assume that the VM is produced on-shell:

$$\begin{aligned} E_{\mathrm{VM}}^2 &= p_z^2 + m_{\mathrm{VM}}^2, \\ \implies E_{\mathrm{VM}} - p_z &= \frac{m_{\mathrm{VM}}^2}{E_{\mathrm{VM}} + p_z}. \end{aligned} \tag{2.26}$$

Assuming the meson is highly relativistic, $E_{\mathrm{VM}} \approx p_z$, we have:

$$\begin{aligned} E_{\mathrm{VM}} + p_z &\approx 2E_{\mathrm{VM}}, \\ E_{\mathrm{VM}} - p_z &\approx \frac{m_{\mathrm{VM}}^2}{2E_{\mathrm{VM}}}. \end{aligned} \tag{2.27}$$

Substituting the approximations back into the definition of rapidity, we have:

$$\begin{aligned} y &= \frac{1}{2}\ln\frac{E_{\mathrm{VM}}+p_z}{E_{\mathrm{VM}}-p_z} \\ &= \frac{1}{2}\ln\frac{2E_{\mathrm{VM}}}{m_{\mathrm{VM}}^2/2E_{\mathrm{VM}}} \\ &= \ln\frac{2E_{\mathrm{VM}}}{m_{\mathrm{VM}}} \\ &= \ln\frac{2\omega}{m_{\mathrm{VM}}} \\ \Longrightarrow \omega &= \frac{m_{\mathrm{VM}}}{2}\cdot e^{\pm y}. \end{aligned} \tag{2.28}$$

Here, $\omega \approx E_{\mathrm{VM}}$ is used in the last step because, in the lab frame, the photon transfers most of its energy to the VM. The $\pm$ sign accounts for the fact that in symmetric UPCs, the photon can be emitted from either nucleus, resulting in the rapidity of the produced VM being positive or negative.

To derive the relationship between W and y, consider the center-of-mass energy of the γp system:

$$\begin{aligned} W^2 = (\sqrt{s_{_{\mathrm{NN}}}})^2 &= (p_\gamma + p_{\mathrm{p}})^2 \\ &= p_\gamma^2 + p_{\mathrm{p}}^2 + 2p_\gamma\cdot p_{\mathrm{p}} \\ &= m_\gamma^2 + m_{\mathrm{p}}^2 + 2E_\gamma E_{\mathrm{p}} + 2E_\gamma p_{\mathrm{p}} \\ &= 4E_\gamma E_{\mathrm{p}} \\ &= 2\omega\cdot 2E_{\mathrm{p}} \\ &= 2\omega\cdot\sqrt{s_{_{\mathrm{NN}}}} \\ \Longrightarrow W^2 &= m_{\mathrm{VM}}\sqrt{s_{_{\mathrm{NN}}}}\cdot e^{\pm y}. \end{aligned} \tag{2.29}$$

In exclusive VM photoproduction, the VM is the sole particle produced in the

final state. To relate x and W, expand the definition of W in terms of x:

$$\begin{aligned} W^2 &= (p_{\mathrm{p}} + q)^2 \\ &= m_{\mathrm{p}}^2 + 2p_{\mathrm{p}} \cdot q + q^2 \\ &= Q^2(1/x - 1) + m_{\mathrm{p}}^2 \\ &\approx Q^2/x. \end{aligned} \tag{2.30}$$

In the high-energy photoproduction limit, $W^2 \gg m_{\mathrm{p}}^2$, and $Q^2 \approx m_{\mathrm{VM}}^2$. The relationship between x and W can be calculated as:

$$\begin{aligned} W^2 &= \frac{m_{\mathrm{VM}}^2}{x} \\ \implies x &= \frac{m_{\mathrm{VM}}}{\sqrt{s_{_{\mathrm{NN}}}}} \cdot e^{\mp y}. \end{aligned} \tag{2.31}$$

In summary, measuring the rapidity of the produced VM allows inference of the photon energy, Bjorken-x, and the center-of-mass energy of the system. The relationships between the variables and the measured rapidity of the VM are:

$$\begin{aligned} \omega &= \frac{m_{\mathrm{VM}}}{2} \cdot e^{\pm y}, \\ W^2 &= \sqrt{s_{_{\mathrm{NN}}}} m_{\mathrm{VM}} \cdot e^{\pm y}, \\ x &= \frac{m_{\mathrm{VM}}}{\sqrt{s_{_{\mathrm{NN}}}}} \cdot e^{\mp y}. \end{aligned} \tag{2.32}$$

2.5 Impulse Approximation

The Impulse Approximation (IA) is a method to calculate the photoproduction cross section, first introduced by Guzey, Kryshen, Strikman, and Zhalov [26]. Impulse is a quantity that defines how a force acting on a particle changes the linear momentum of that particle. In the context of particle scattering, IA refers to the case when the force exerted on the particle acts for a very short time and is much greater than any other forces present. Thus, one can effectively ignore all nuclear effects except

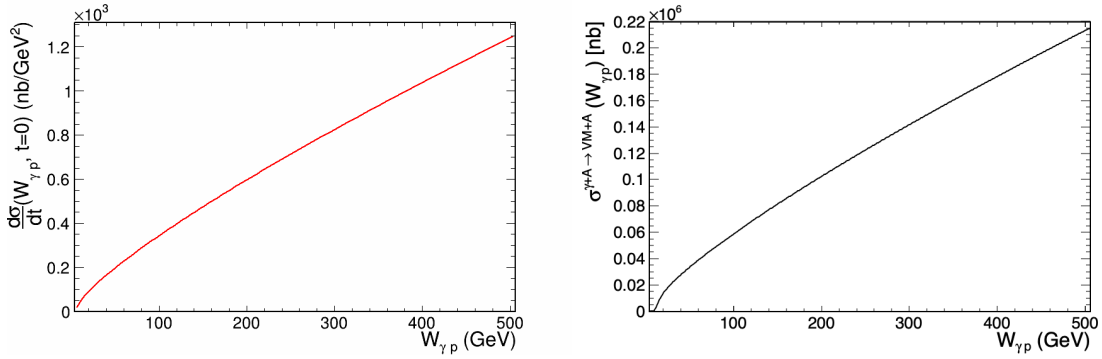

Figure 2.3 : The fit to the differential J/ψ photoproduction cross section data (left) and the calculated cross section from Eq. 2.33 using the fitted data (right).

coherence. The cross section is estimated as

$$\sigma^{\mathrm{IA}}_{\gamma A\to VA}(W_{\gamma\mathrm{p}}) = \frac{\mathrm{d}\sigma_{\gamma\mathrm{p}\to V\mathrm{p}}(W_{\gamma\mathrm{p}}, t=0)}{\mathrm{d}t}\Phi_A(t_{min}), \tag{2.33}$$

where $\mathrm{d}\sigma_{\gamma\mathrm{p}\to V\mathrm{p}}(W_{\gamma\mathrm{p}}, t=0)/\mathrm{d}t$ is the differential cross section of $\gamma\mathrm{p}\to V\mathrm{p}$ and can be extracted from $\mathrm{e}^{\pm}\mathrm{p}$ collisions at HERA and pPb collisions at the LHC; $\Phi_A(t_{min}) = \int_{t_{min}}^{\infty} dt\,|F_A(t)|^2$ and $F_A(t)$ is the elastic nuclear form factor from [24]. Fig. 2.3 shows the fitted $\mathrm{d}\sigma_{\gamma\mathrm{p}\to \mathrm{J}/\psi\mathrm{p}}(W_{\gamma\mathrm{p}}, t=0)/\mathrm{d}t$ determined from fitting worldwide experimental data using parameters cited in [26], and $\sigma^{\mathrm{IA}}_{\gamma A\to \mathrm{J}/\psi A}(W_{\gamma\mathrm{p}})$ from Eq. 2.33.

A detailed calculation of the multiple scattering series [22] for the $\gamma\mathrm{Pb}\to \mathrm{J}/\psi\mathrm{Pb}$ scattering amplitude in the leading twist theory of nuclear shadowing describes the leading order (LO) as the IA, next-to-leading order (NLO) as the double scattering, etc. At LO, nuclear forces between nucleons are ignored, so the scattering is effectively a superposition of scatterings on individual nucleons. In short, the origin of shadowing effects is the neglect of multiple scattering. The idea behind IA is that this cross section is based on experimental data and hence can serve as a model-independent comparison of nuclear structure to single-nucleon structure.

Note that the IA model is, to some extent, model independent, since the coher-

ent production cross section is determined by fitting all available experimental data measured in γp interactions. Consequently, to make a fair comparison of coherent production between γp and γPb, one should compare the coherent production in PbPb UPCs to the IA curve.

Chapter 3

The Compact Muon Solenoid Experiment

3.1 The Large Hadron Collider

The Large Hadron Collider (LHC) at the European Organization for Nuclear Research (CERN) in Geneva, Switzerland, is the world's largest and most powerful particle accelerator. It is a circular collider with a circumference of 27 km, situated 100 m underground near the French-Swiss border. A schematic of the LHC is shown in Fig. 3.1. Particles are accelerated through a series of linear and circular accelerators before injection into the LHC. The main stages of the LHC accelerator complex include the linear accelerators (LINAC2 and LINAC3), the Low Energy Ion Ring (LEIR), the Proton Synchrotron Booster (PSB), the Proton Synchrotron (PS), the Super Proton Synchrotron (SPS), and the LHC itself.

Modern circular collider facilities like the LHC host a variety of detectors at different interaction points (IPs) around the ring. The LHC has a total of 8 IPs, 4 of which host major experiments: ALICE, ATLAS, CMS, and LHCb. The LHC has two separate beam pipes. Particles are accelerated to nearly the speed of light in opposite directions and focused by superconducting quadrupoles to enhance the probability of collisions at the IPs.

The LHC is a proton–proton and heavy-ion collider designed to achieve high energies and luminosities, providing a unique opportunity to study both γp and γPb interactions at the TeV scale. For example, the LHC can achieve a maximum photon-

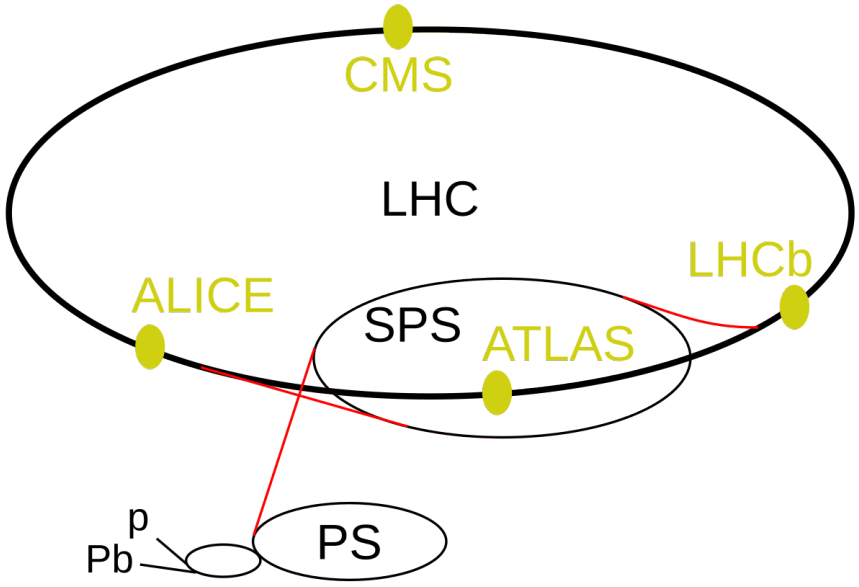

Figure 3.1 : Schematic of the LHC at CERN. The LHC is a circular collider with a circumference of 27 km, located 100 m underground near the French-Swiss border. Figure from [27].

nucleon center-of-mass energy of $W_{\gamma p} \approx 5.4\,\text{TeV}$ in pp collisions and $W_{\gamma N}^{\text{Pb}} \approx 700\,\text{GeV}$ in PbPb collisions [21], establishing it as an energy frontier for photonuclear interaction studies.

3.2 LHC Operation

LHC data-taking is organized into runs, with each run comprising a series of data-taking periods. During these periods, the LHC is filled with protons or heavy ions, and the beams are collided. Runs are separated by long shutdowns, during which the accelerator and experiments undergo upgrades and maintenance. Run 1 of the LHC took place from 2009 to 2012, Run 2 from 2015 to 2018, and Run 3 is scheduled to be 2022 to 2025.

In Run 2, the LHC operated at a center-of-mass energy per nucleon pair of $\sqrt{s_{\text{NN}}} = 13\,\text{TeV}$ for pp collisions and $\sqrt{s_{\text{NN}}} = 5.02\,\text{TeV}$ for PbPb collisions. During Run 3, these energies were increased to $\sqrt{s_{\text{NN}}} = 13.6\,\text{TeV}$ and $\sqrt{s_{\text{NN}}} = 5.36\,\text{TeV}$, respectively.

The difference in center-of-mass energy between the two collision systems arises from the additional neutrons in the lead nucleus, which do not participate in the electromagnetic acceleration process. For the Pb ions, the mass number and atomic number are $A = 208$ and $Z = 82$, respectively. This ratio is $Z/A = 0.394$. Therefore, the $\sqrt{s_{\text{NN}}}$ for PbPb collisions is given by

$$\sqrt{s_{\text{NN}}} \cdot Z/A = 13\,\text{TeV} \cdot 0.394 \approx 5.02\,\text{TeV}. \tag{3.1}$$

Instantaneous luminosity ($\mathcal{L}$) measures the collision rate and is defined as the number of particles per unit area per unit time, with units of $\text{cm}^{-2}\,\text{s}^{-1}$. An increase in instantaneous luminosity leads to more collisions per unit time, which in turn leads to more data collected. It can be thought of as representing the brightness of the beams. A brighter beam contains more particles per unit of cross-sectional area. The instantaneous luminosity is given by

$$\mathcal{L} = \frac{f N_1 N_2 N_b}{4\pi \sigma_x \sigma_y}, \tag{3.2}$$

where f is the revolution frequency of the particles, N_1 and N_2 are the number of particles in the two colliding beams, N_b is the number of bunches in each beam, and σ_x and σ_y are the effective transverse beam widths, assuming the beams are taken to have a Gaussian profile with width and height. Integrated luminosity is the time integral of instantaneous luminosity. Conventionally, it is expressed in terms of barns, where $1\,\text{b} = 10^{-24}\,\text{cm}^2$. In Run 2, the LHC achieved a peak instantaneous luminosity of $2.1 \times 10^{34}\,\text{cm}^{-2}\,\text{s}^{-1}$ for pp collisions and $6.4 \times 10^{27}\,\text{cm}^{-2}\,\text{s}^{-1}$ for PbPb

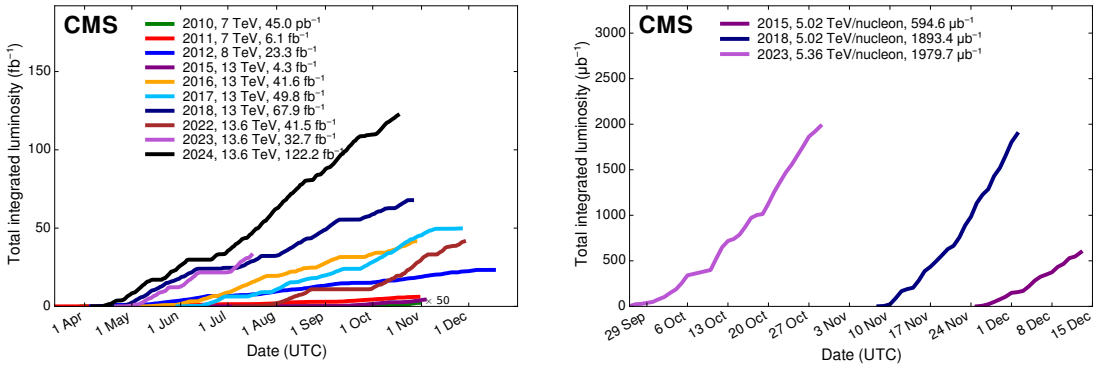

Figure 3.2 : Integrated luminosity delivered by the LHC to the CMS experiment during stable beams for collisions (left) and collisions (right) as a function of day. Figure from CMS public results page [29].

collisions [28]. Fig. 3.2 shows the integrated luminosity delivered by the LHC to the CMS experiment.

The transverse beam widths at the IP are determined by the focusing forces (from magnets) and the beam divergence (from particle momentum). Beam emittance characterizes the spread of particle positions and momenta in the beam. Beta star (β^*) quantifies the beam size at the IP. The beam width can be expressed in terms of ε and β^* as:

$$\sigma = \sqrt{\varepsilon/\gamma \cdot \beta^*}. \tag{3.3}$$

For example, during the LHC fill 7442 in the 2018 PbPb collision, the LHC had $N_b = 288$ colliding bunch pairs at IP5 with a bunch spacing of 150 ns. The LHC beam optics were adjusted to a β^* of 0.5 m, with the beams targeting a proton-equivalent transverse emittance of $\varepsilon = 3.5\,\mu$m. This leads to a $\sigma = 25\,\mu$m [30].

At the LHC, the total circumference is 27 km, and the beams are accelerated in opposite directions in two separate beam pipes. For particles traveling near the speed

of light, the revolution frequency is calculated as:

$$f_{\mathrm{LHC}} = \frac{L}{c} = \frac{27,000\,\mathrm{m}}{3 \times 10^{8}\,\mathrm{m/s}} \approx 11.24\,\mathrm{MHz}. \tag{3.4}$$

LHC detectors also record data from bunch crossings, referred to as zero-bias (ZB) events. These events are recorded using the ZB trigger. The ZB rate is determined by multiplying the number of bunches per beam by the LHC revolution frequency:

$$f_{\mathrm{ZB}} = N_b \cdot f_{\mathrm{LHC}}. \tag{3.5}$$

For example, during the 2018 pp (PbPb) run, the LHC collided 2556 (733) bunches per beam. This leads to a ZB rate of $f_{\mathrm{ZB}} \approx 28.7\,(8.2)\,\mathrm{MHz}$.

Within each run, data is further divided into periods called fills, which typically last a few hours. A fill refers to a complete cycle of injecting, accelerating, colliding, and eventually dumping the beams. The smallest division of data is the luminosity section (LS), which is defined as a fixed time interval of 23.31 seconds:

$$\mathrm{LS} = 23.31\,\mathrm{s} = 2^{18}\ \text{LHC revolutions}. \tag{3.6}$$

Each LS contains multiple events, which are the basic units of data in high-energy physics. After data collection, LSs are certified and deemed suitable for physics analysis through a good run list.

The typical number of protons in a proton bunch is $N_{\mathrm{p}} \sim 10^{11}$, while the number of Pb ions in a Pb bunch is $N_{\mathrm{Pb}} \sim 10^{8}$ [28]. However, only a very small fraction of these particles actually collide in each bunch crossing. If multiple proton pairs interact within a single bunch crossing, the average number of interactions per crossing is referred to as pileup. Pileup is calculated as the product of the instantaneous luminosity and the inelastic cross section, divided by the ZB rate:

$$\mathrm{Pileup} = \frac{\mathcal{L} \cdot \sigma_{\mathrm{pp}}}{f_{\mathrm{ZB}}}, \tag{3.7}$$

where $\sigma_{\mathrm{pp}} \approx 80\,\mathrm{mb}$ is the inelastic pp cross section at $\sqrt{s_{\mathrm{NN}}} = 13\,\mathrm{TeV}$ [31]. Typical pileup values for pp collisions at the LHC are around 50–60. However, for PbPb collisions, the pileup is much lower. This is because the Pb ion beam has 10 times fewer bunches, 4 times larger bunch spacing, and 1000 times fewer particles per bunch compared to the proton beam. The inelastic PbPb cross section is $\sigma_{\mathrm{PbPb}} \approx 7.7\,\mathrm{b}$ at $\sqrt{s_{\mathrm{NN}}} = 5.02\,\mathrm{TeV}$ [32]. Considering the differences in luminosity and cross section, the pileup in PbPb collisions is approximately:

$$\mathrm{Pileup}^{\mathrm{PbPb}} = \frac{\mathcal{L}^{\mathrm{PbPb}} \cdot \sigma_{\mathrm{PbPb}}}{f_{\mathrm{ZB}}^{\mathrm{PbPb}}} \sim 0.006. \tag{3.8}$$

3.3 The Compact Muon Solenoid Detector

The Compact Muon Solenoid (CMS) is a general-purpose detector located at IP5 of the LHC [33]. As the name suggests, the CMS detector is compact, with a length of 21.6 m, a diameter of 15 m, and a weight of 14,000 tons. Interestingly, the CMS detector weighs more than the Eiffel Tower, which weighs 10,100 tons. A schematic view of the CMS detector is shown in Fig. 3.3.

CMS is a cylindrical detector centered around a 3.8 T superconducting solenoid magnet, which generates a magnetic field to bend the trajectories of charged particles. The detector consists of several subsystems, each designed to measure the properties of particles produced in collisions. Particles passing through the detector leave signatures in each subsystem, which are used to reconstruct their trajectories, energies, and types. Fig. 3.4 shows a slice of the CMS detector, highlighting the different subsystems and the particle detection signatures they are sensitive to.

A detailed description of the CMS detector can be found elsewhere [33]. This section provides a brief overview of the main components of the CMS detector.

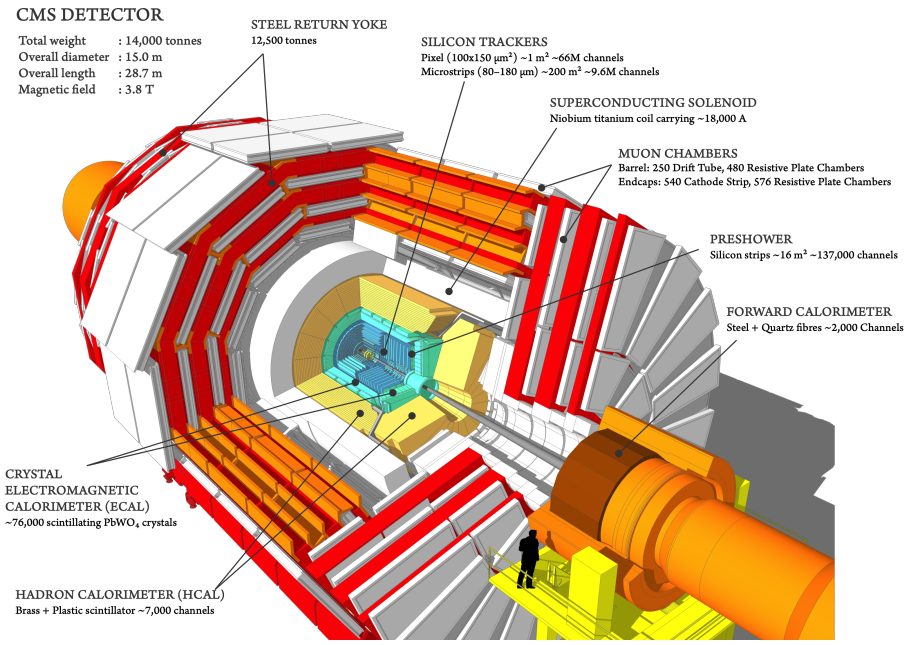

Figure 3.3 : An illustration of the CMS detector at the LHC. Figure from [34].

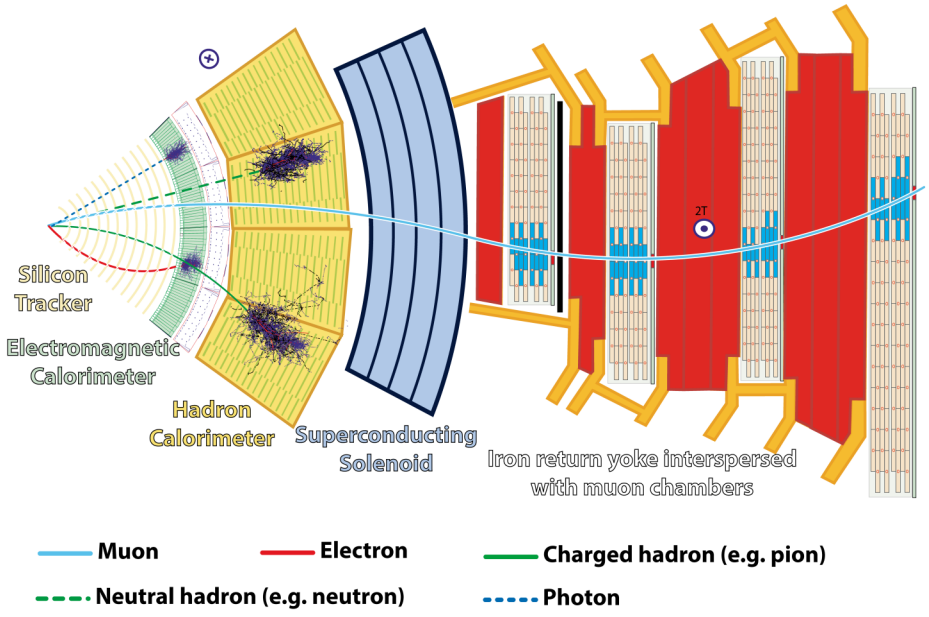

Figure 3.4 : A slice of the CMS detector showing the different subsystems and the particle detection signatures they are sensitive to. Figure from [34].

3.3.1 Tracker

A tracking detector registers the passage of charged particles through the detector. By reconstructing particle trajectories, the tracking detector determines the particle's momentum, charge, and vertex position. The CMS inner tracking system is composed of a pixel detector and a silicon strip tracker. They are made of silicon sensors, which are sensitive to the passage of charged particles.

The pixel detector is the innermost part of the tracking system and is used to measure the position of the particles with high precision [35]. The CMS detector has four layers of pixel detectors in the barrel region and three layers in the endcap region. In total, the pixel detector has 66 million pixels. The high granularity of the pixel detector ensures precise measurements, as all particles passing through the detector must first traverse its innermost layer. An accurate measurement of the passage of the particles through the smaller surface area of the pixel detector is essential for the reconstruction of the particle's trajectory and vertex position.

At larger radii, the silicon strip tracker is used to reduce the overall cost of the detector. Compared to the pixel detector, the silicon strip tracker has a coarser granularity, but it covers a larger area.

3.3.2 Electromagnetic Calorimeter

A calorimeter measures particle energy by stopping particles and recording the energy they deposit in the detector. High energy entering the calorimeter will produce a shower of particles, which will deposit energy in the detector. The electromagnetic calorimeter (ECAL) is used to measure the energy of electrons and photons. Electrons lose energy through bremsstrahlung radiation, which is proportional to the square of their charge and inversely proportional to their mass. Photons lose energy through

pair production, which depends on the square of the nucleus's charge and is inversely proportional to its mass.

The CMS ECAL is a homogeneous calorimeter made of lead tungstate ($PbWO_4$) crystals [36]. Homogeneous means the detector material is uniform and induces particle showers. The shower is initiated by the passage of electrons and photons through the crystals, which produce scintillation light that is collected by photodetectors to measure the energy of the particles. A preshower detector is placed in front of the ECAL to help distinguish between neutral pions and photons. This distinction is crucial because neutral pions decay into two photons, which could be misidentified as a single photon.

3.3.3 Hadronic Calorimeter

The hadronic calorimeter (HCAL) measures the energy of hadrons, particles composed of quarks. Since hadrons interact through the strong force, they will produce a shower of particles when they pass through the calorimeter. However, the particles in the hadronic shower are different from those in the electromagnetic shower. These particles primarily include pions, kaons, and protons, the lightest hadrons. They are stopped by nuclear interactions with the detector material.

The CMS HCAL is a sampling calorimeter made of alternating layers of brass and plastic scintillator [37]. Here, sampling means that the detector material is different from the material that induces the shower of particles. The shower is initiated by the passage of hadrons through the brass, which produces scintillation light that is collected by photodetectors to measure the energy of the particles. Because the nuclear interaction length exceeds the radiation length, the HCAL is thicker than the ECAL.

3.3.4 Muon System

As the name "Compact Muon Solenoid" implies, detecting muons is one of the primary purposes of the CMS detector. Muons are the only charged particles capable of penetrating the calorimeters to reach the outermost part of the detector. Therefore, the muon system is placed outside the calorimeters to measure the momentum of muons. The muon system operates similarly to the tracker but has a larger radius and lower granularity. Muons are bent by the magnetic field of the solenoid, and the curvature of the muon trajectory is used to measure the muon's momentum.

The CMS muon system is composed of three types of detectors: drift tubes (DTs), cathode strip chambers (CSCs), and resistive plate chambers (RPCs) [38]. The DTs are used in the barrel region, the CSCs are used in the endcap region, and the RPCs are used in both regions. RPCs provide a fast trigger signal for the muon system.

3.4 CMS Data Processing

The number of particle interactions produced at the LHC is enormous. However, the vast majority of these interactions are not relevant for physics analysis. At the LHC, the initial bunch crossing rate is 40 MHz. Selecting interesting events has been a long-standing challenge in high-energy physics. This selection process is managed by the trigger system. At CMS, the trigger system is divided into two levels: the Level-1 trigger (L1) and the High-Level Trigger (HLT) [39].

3.4.1 Level-1 Trigger

The L1 trigger is a hardware-based system that decides whether to keep or discard an event based on the available information. The purpose of the L1 trigger is to reduce

the event rate from 40 MHz to 100 kHz. The L1 trigger is based on custom electronics that are designed to be fast and efficient. The L1 trigger selects events containing interesting physics objects, such as detector signals consistent with the passage of a high-energy electron, photon, muon, or jet.

3.4.2 High-Level Trigger

The HLT is a software-based system that makes decisions using predefined algorithms. The HLT is designed to reduce the event rate from 100 kHz to 1 kHz. The HLT uses a large network of CPUs and full detector information to decide whether to keep or discard an event. The HLT is based on a set of algorithms that are designed to be fast and efficient.

3.4.3 Offline Data Processing

Experimental data processing is organized into several stages. The first stage involves detector readout, where raw data is collected from the detector electronics via the data-acquisition system (DAQ). The data is then passed through a software trigger. The events that pass the trigger are then stored on disk for offline processing. The resulting raw data is then passed through a reconstruction process, where the raw data is converted into a format that can be used for analysis. Once the data is reconstructed, it is passed through a series of analysis steps, where the data is filtered and analyzed to extract the physics information. Unlike online reconstruction, offline reconstruction is not time-critical, can be performed on a larger scale, and can be repeated when new algorithms are developed. The basic output of the reconstruction step is a very detailed event record. A partially reduced version of the event record is called an analysis object data format (AOD). The AOD is a compact representation

of the event record, containing only the information necessary for analysis.

Chapter 4

Coherent J/ψ Meson Photoproduction

4.1 Approaching the Gluon Saturation Regime

Coherent J/ψ meson photoproduction is motivated by the observed deviation of the J/ψ meson production cross section from the expected soft pomeron exchange ($\delta \approx 0.22$) in HERA data (Fig. 1.5). The mass of the J/ψ meson provides a hard scale for perturbative QCD (pQCD) calculations. The observed steepening of the cross section with energy suggests an increased gluon density in the proton at leading order. Exclusive photoproduction of charmonium off protons serves as a clean probe for investigating saturation effects, which are expected at high energy and low Bjorken-x. A reduction in the cross section, deviating from the linear increase with $W_{\gamma\mathrm{p}}$, would signal the onset of gluon saturation [40].

ALICE and LHCb have measured the coherent J/ψ meson photoproduction cross section ($\sigma_{\gamma\mathrm{p}\to\mathrm{J}/\psi\mathrm{p}}$) in pp and pPb collisions at the LHC, probing the proton gluon distribution at $x \sim 10^{-5}$. The $\sigma_{\gamma\mathrm{p}\to\mathrm{J}/\psi\mathrm{p}}$ as a function of γp center-of-mass energy, $W_{\gamma\mathrm{p}}$, is shown in Fig. 4.1. Together with HERA data, these measurements map the $W_{\gamma\mathrm{p}}$ dependence of the cross section up to $W_{\gamma\mathrm{p}} \approx 1000\,\mathrm{GeV}$ [41, 42, 43, 44, 45, 46, 47]. However, the cross section continues to increase linearly with $W_{\gamma\mathrm{p}}$ at LHC energies, indicating that gluon saturation has not yet been reached.

Coherent J/ψ meson photoproduction in heavy-ion UPCs offers a promising avenue for exploring gluon saturation phenomena [9, 10]. Compared to pp collisions, PbPb

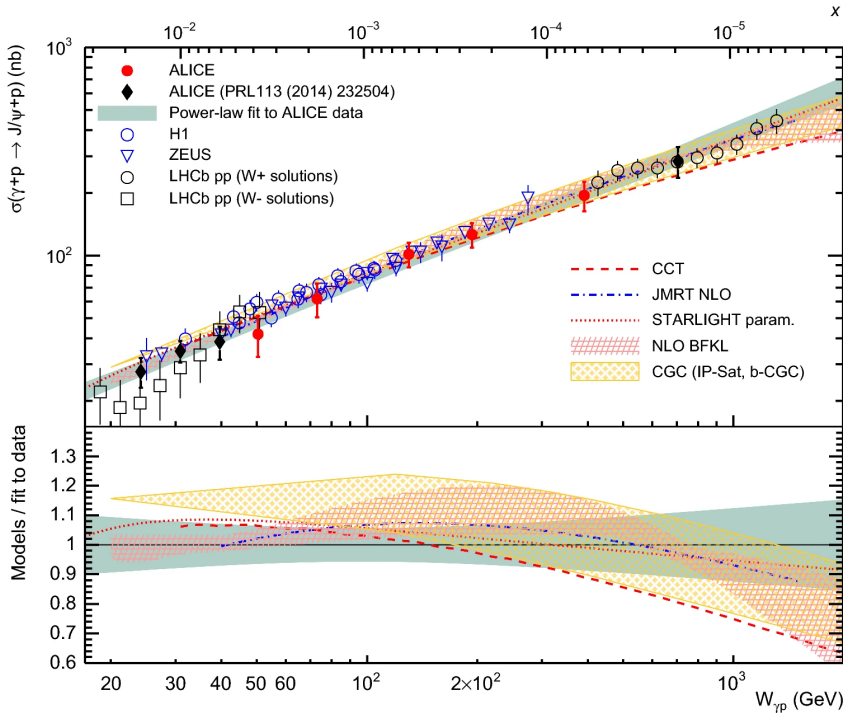

Figure 4.1 : The coherent J/ψ meson photoproduction cross section as a function of $W_{\gamma \mathrm{p}}$ from HERA and LHC experiments. The LHC data are from ALICE and LHCb experiments in pp and pPb collisions. The data are compared to HERA results and pQCD predictions. Figure from Ref. [47].

UPCs provide several advantages:

- Enhanced photon flux due to the high charge of Pb ions.
- Reduced photon virtuality owing to the larger Pb ion radius.
- Neutron tagging capability, which helps resolve the ambiguity in identifying which nucleus acts as the photon emitter and which as the photon target in photon-nucleus interactions.

However, complications arise in UPCs because the photon can be emitted from either nucleus, resulting in a two-way ambiguity as to which nucleus emitted the photon and which served as the target [22]. The measured differential cross section is thus a combination of coherent J/ψ meson photoproduction from both nuclei. Fig. 4.2 schematically illustrates this two-way ambiguity. This ambiguity arises because, in symmetric heavy-ion collisions, both nuclei are equally likely to emit the photon or act as the target.

This two-way ambiguity is also evident in Eq. 2.24, where the measured differential coherent J/ψ meson photoproduction cross section ($\mathrm{d}\sigma_{\mathrm{J}/\psi}/\mathrm{d}y$) in UPCs is proportional to the photon flux, $N_{\gamma A}$, and the single photon-nucleus cross section, $\sigma_{\gamma\mathrm{Pb}\to\mathrm{J}/\psi\mathrm{Pb}}$.

Eq. 2.24 can be rewritten in terms of the experimentally measurable rapidity of the produced J/ψ meson, y. Using the relation between photon energy and the rapidity of the produced VM in Eq. 2.32, the cross section can be expressed as:

$$\frac{\mathrm{d}\sigma_{\mathrm{J}/\psi}}{\mathrm{d}y} = N_{\gamma\mathrm{Pb}}(y)\,\sigma_{\gamma\mathrm{Pb}\to\mathrm{J}/\psi\mathrm{Pb}}(y) + N_{\gamma\mathrm{Pb}}(-y)\,\sigma_{\gamma\mathrm{Pb}\to\mathrm{J}/\psi\mathrm{Pb}}(-y), \tag{4.1}$$

where the two terms on the right-hand side of Eq. 4.1 reflect the ambiguity in symmetric PbPb UPCs. Thus, $\mathrm{d}\sigma_{\mathrm{J}/\psi}/\mathrm{d}y$ is a combination of high-energy and low-energy photon-nucleus interactions.

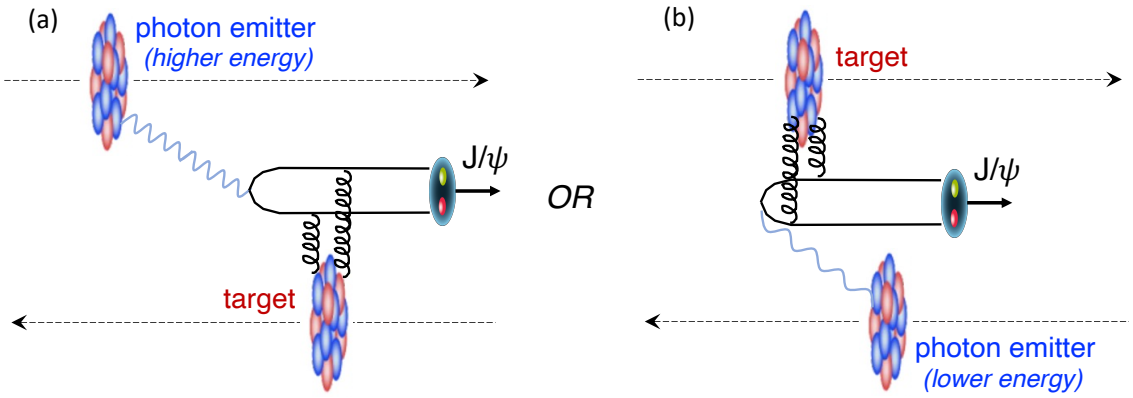

Figure 4.2 : Schematic diagram of coherent J/ψ meson photoproduction in UPCs. The photon can be emitted from either nucleus, resulting in ambiguity as to which nucleus emitted the photon and which was the target.

For decades, LHC experiments have not been able to resolve this two-way ambiguity in UPCs, measuring only the differential cross section as a function of rapidity in Run 1 and Run 2 [48, 49, 50, 51, 52, 53, 54]. Prior to this analysis, the ALICE experiment reported $\mathrm{d}\sigma_{\mathrm{J}/\psi}/\mathrm{d}y$ in PbPb UPCs at $\sqrt{s_{_{\mathrm{NN}}}} = 5.02\,\mathrm{TeV}$. Fig. 4.3 shows the coherent J/ψ meson photoproduction cross section as a function of rapidity from the ALICE experiment.

The observed $\mathrm{d}\sigma_{\mathrm{J}/\psi}/\mathrm{d}y$ exhibits significant nuclear suppression compared to the Impulse Approximation (IA) prediction, which assumes the nucleus is a collection of independent nucleons; see Sec. 2.5.

Theoretical predictions incorporating saturation or shadowing effects fail to fully describe the data, highlighting gaps in our understanding of the underlying mechanisms. Little is known about the nuclear gluon distribution at low Bjorken-x. Resolving this ambiguity and extracting the energy dependence of the coherent J/ψ meson photoproduction cross section are crucial for understanding the nuclear gluon distribution and the onset of gluon saturation phenomena.

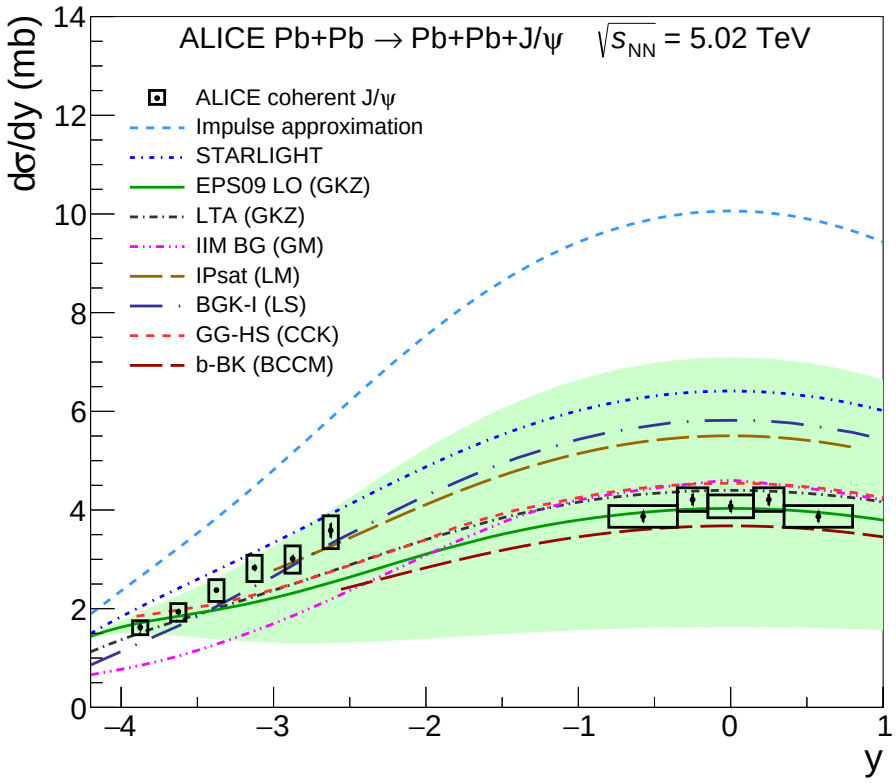

Figure 4.3 : Coherent J/ψ meson photoproduction cross section as a function of rapidity from the ALICE experiment. The data are compared to various theoretical models. Figure from Ref. [51].

4.2 Disentangling the Two-Way Ambiguity

A key to resolving the two-way ambiguity in UPCs lies in the possibility of multiphoton exchange [55, 17]. Since the photon flux surrounding heavy ions is proportional to the square of the ion charge, Z^2, additional photon exchanges between a single ion pair can accompany photon-nuclear interactions. These exchanges can lead to electromagnetic dissociation (EMD), where protons and neutrons oscillate collectively and decay by emitting one or more neutrons. These neutrons, with very low p_{T} and beam rapidity, can be detected by the zero-degree calorimeters (ZDC) with nearly 100% efficiency. By analyzing the energy deposited in the ZDCs, the neutron multiplicity can be determined.

The neutron multiplicity provides a way to classify UPC events into different impact parameter (b) ranges [22, 56]. The condition of neutron emission modifies the photon flux as:

$$N_{\gamma A}^{\mathrm{injn}}(\omega) = \int_{2R_A}^{\infty} d^2b\, N_{\gamma/A}(\omega, b)\, P^{\mathrm{injn}}(b), \tag{4.2}$$

where $P^{\mathrm{injn}}(b)$ is the impact parameter-dependent probability of different neutron emission configurations. The subscript injn indicates the neutron multiplicity class, which can be 0n0n, 0nXn, or XnXn, defined as follows:

- **0n0n:** No neutrons emitted from either nucleus.
- **0nXn:** At least one neutron emitted from one nucleus, none from the other.
- **XnXn:** At least one neutron emitted from both nuclei.

For each neutron multiplicity class, the excitation probability can be expressed

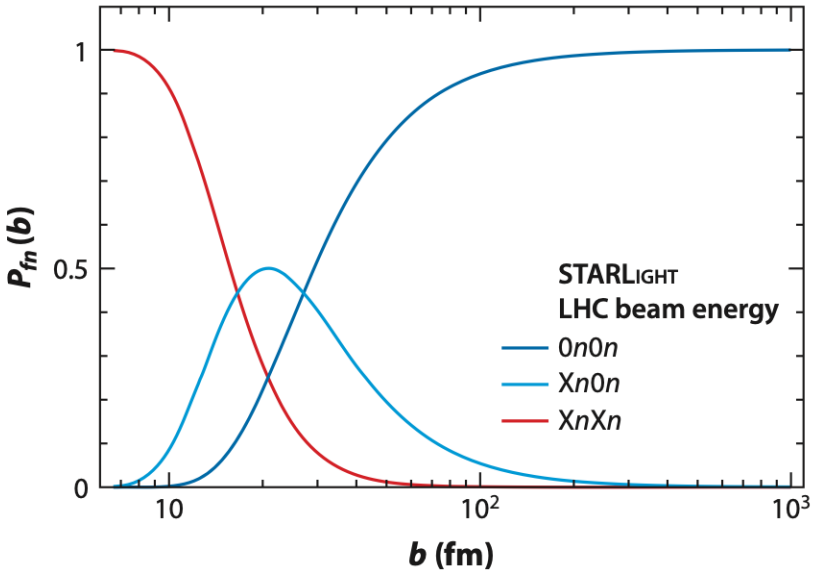

Figure 4.4 : Neutron emission probability as a function of impact parameter for the neutron multiplicity classes 0n0n, 0nXn, and XnXn, estimated using the STARLIGHT MC simulation [21].

as:

$$\begin{aligned} P^{\mathrm{0n0n}}(b) &= P_1(b)P_2(b), \\ P^{\mathrm{0nXn}}(b) &= P_1(b)(1-P_2(b)), \\ P^{\mathrm{XnXn}}(b) &= (1-P_1(b))(1-P_2(b)), \end{aligned} \tag{4.3}$$

where $P_1(b)$ and $P_2(b)$ are the probabilities of neutron emission from nuclei 1 and 2, respectively. In general, $P_1(b) \sim P_2(b) \sim 1/b^2$. These probabilities can be estimated using the STARLIGHT Monte Carlo (MC) simulation. Fig. 4.4 shows the neutron emission probability as a function of impact parameter for the neutron multiplicity classes 0n0n, 0nXn, and XnXn.

High neutron multiplicity corresponds to small $\langle b \rangle$, while low neutron multiplicity corresponds to large $\langle b \rangle$:

- **0n0n:** $\langle b \rangle \gtrsim 40\,\mathrm{fm}$

- **0nXn:** $\langle b \rangle \sim 20\,\text{fm}$
- **XnXn:** $\langle b \rangle \lesssim 15\,\text{fm}$

Eq. 4.1 can be rewritten in terms of neutron multiplicity as:

$$\begin{aligned}
\frac{\mathrm{d}\sigma^{\mathrm{0n0n}}_{\mathrm{J}/\psi}}{\mathrm{d}y} &= N^{\mathrm{0n0n}}_{\gamma\mathrm{Pb}}(y)\,\sigma_{\gamma\mathrm{Pb}\to\mathrm{J}/\psi\mathrm{Pb}}(y) + N^{\mathrm{0n0n}}_{\gamma\mathrm{Pb}}(-y)\,\sigma_{\gamma\mathrm{Pb}\to\mathrm{J}/\psi\mathrm{Pb}}(-y), \\
\frac{\mathrm{d}\sigma^{\mathrm{0nXn}}_{\mathrm{J}/\psi}}{\mathrm{d}y} &= N^{\mathrm{0nXn}}_{\gamma\mathrm{Pb}}(y)\,\sigma_{\gamma\mathrm{Pb}\to\mathrm{J}/\psi\mathrm{Pb}}(y) + N^{\mathrm{0nXn}}_{\gamma\mathrm{Pb}}(-y)\,\sigma_{\gamma\mathrm{Pb}\to\mathrm{J}/\psi\mathrm{Pb}}(-y), \\
\frac{\mathrm{d}\sigma^{\mathrm{XnXn}}_{\mathrm{J}/\psi}}{\mathrm{d}y} &= N^{\mathrm{XnXn}}_{\gamma\mathrm{Pb}}(y)\,\sigma_{\gamma\mathrm{Pb}\to\mathrm{J}/\psi\mathrm{Pb}}(y) + N^{\mathrm{XnXn}}_{\gamma\mathrm{Pb}}(-y)\,\sigma_{\gamma\mathrm{Pb}\to\mathrm{J}/\psi\mathrm{Pb}}(-y).
\end{aligned} \tag{4.4}$$

By solving the system of equations in Eq. 4.4, the relative contributions of low- and high-energy photons to the measured $\mathrm{d}\sigma_{\mathrm{J}/\psi}/\mathrm{d}y$ can be separated without ambiguity.

In this chapter, coherent J/ψ meson photoproduction in PbPb UPCs is studied using the forward neutron tagging technique. The differential cross section is measured for the first time as a function of rapidity in different neutron multiplicity classes (0n0n, 0nXn, and XnXn). Additionally, the energy dependence of the coherent J/ψ meson photoproduction cross section is extracted, and the cross section suppression ratio is measured as a function of x. These results provide the first evidence of stronger suppression towards $x \approx 6 \times 10^{-5}$.

4.3 Datasets and MC Samples

The analysis is performed using data collected by the CMS detector during the 2018 PbPb run at $\sqrt{s_{_{\mathrm{NN}}}} = 5.02\,\text{TeV}$, with an integrated luminosity of approximately $1.7\,\text{nb}^{-1}$. Good run selection and luminosity determination are based on the CMS official muon physics JSON file.

MC samples are generated using the STARLIGHT generator [25] and are simulated with the CMS GEANT4 framework [57] to model the full detector response. Details

of the simulation samples are listed in Tab. 4.1 and can be found on the CMS official simulation request page.

4.4 Event Selection

4.4.1 Online Event Selection

The online event selection uses the following HLT trigger, optimized to select events with at least one muon track from UPC PbPb collisions:

- **Trigger:**
  - HLT_HIUPC_SingleMuOpen_NotMBHF2AND_v
- **Requirements:**
  - At least one hadronic forward calorimeter (HF, $2.9 < |\eta| < 5.2$) must have no signal above the noise threshold.
  - At least one Level 1 (L1) muon must be reconstructed in the muon chambers.
  - The L1 muon must fire at least two muon stations and has no p_{T} threshold requirement. This trigger selects exclusive-type events containing muon tracks with no activity in either HF detector.

4.4.2 Offline Event Selection

The offline event selection is performed using the standard CMS event selection criteria, designed to suppress background processes such as hadronic PbPb collisions and beam scraping events. The criteria are as follows:

Table 4.1 : MC samples for coherent/incoherent J/ψ and ψ(2S) measurements in 2018 PbPb collisions at $\sqrt{s_{\rm NN}} = 5.02\,\text{TeV}$.

Generator	Events	Physics process	Event content
STARLIGHT	5 M	Coherent J/$\psi \to \mu^+\mu^-$	AODSIM
STARLIGHT	4 M	Coherent J/$\psi \to \mu^+\mu^-$ (0n0n)	AODSIM
STARLIGHT	2 M	Coherent J/$\psi \to \mu^+\mu^-$ (0nXn)	AODSIM
STARLIGHT	2 M	Coherent J/$\psi \to \mu^+\mu^-$ (XnXn)	AODSIM
STARLIGHT	1 M	Coherent ψ(2S) $\to \mu^+\mu^-$	AODSIM
STARLIGHT	2.5 M	Coherent ψ(2S) $\to$ J/$\psi \to \mu^+\mu^-$	AODSIM
STARLIGHT	2.5 M	Incoherent J/$\psi \to \mu^+\mu^-$	AODSIM
STARLIGHT	1 M	Incoherent ψ(2S) $\to \mu^+\mu^-$	AODSIM
STARLIGHT	2.5 M	$\gamma\gamma \to \mu^+\mu^-$ ($2 < m_{\mu^+\mu^-} < 8\,\text{GeV}/c^2$)	AODSIM
STARLIGHT	10 M	Coherent J/$\psi \to \mu^+\mu^-$	GENSIM
STARLIGHT	8 M	Coherent J/$\psi \to \mu^+\mu^-$ (0n0n)	GENSIM
STARLIGHT	4 M	Coherent J/$\psi \to \mu^+\mu^-$ (0nXn)	GENSIM
STARLIGHT	4 M	Coherent J/$\psi \to \mu^+\mu^-$ (XnXn)	GENSIM
STARLIGHT	2 M	Coherent ψ(2S) $\to \mu^+\mu^-$	GENSIM
STARLIGHT	5 M	Incoherent J/$\psi \to \mu^+\mu^-$	GENSIM

Table 4.2 : Event selection criteria.

Event Selection Criteria
pprimaryVertexFilter & pclusterCompatibilityFilter
$HF^{\text{leading}}_{\text{plus}} \leq 7.3\,\text{GeV}$ & $HF^{\text{leading}}_{\text{minus}} \leq 7.6\,\text{GeV}$
$N^{\text{HP}}_{\text{trk}} == 2$
runID ≥ 326776

- A primary vertex passing the standard "pprimaryVertexFilter" filter is required to ensure valid vertex reconstruction.

- The cluster shapes in the pixel detector must be compatible with those expected from a heavy-ion collision ("pclusterCompatibilityFilter" filter) to suppress beam scraping events.

- All tower energies in the HF detectors must be below noise thresholds (7.3 GeV on the plus side and 7.6 GeV on the minus side) to suppress inclusive hadronic interactions [58]. These thresholds are determined from empty bunch crossing ("No BPTX") events and correspond to the 99% position of the leading tower energy spectrum, as shown by the green lines in Fig. 4.5.

- Events must contain exactly two high-purity tracks and no additional activity.

- The zero-degree calorimeter (ZDC, $|\eta| > 8.3$) must be functional, which is ensured for runs with runID ≥ 326776.

After applying the run number selection, the total integrated luminosity is reduced to $1520.3\,\mu\text{b}^{-1}$. The event selection criteria are summarized in Tab. 4.4.2.

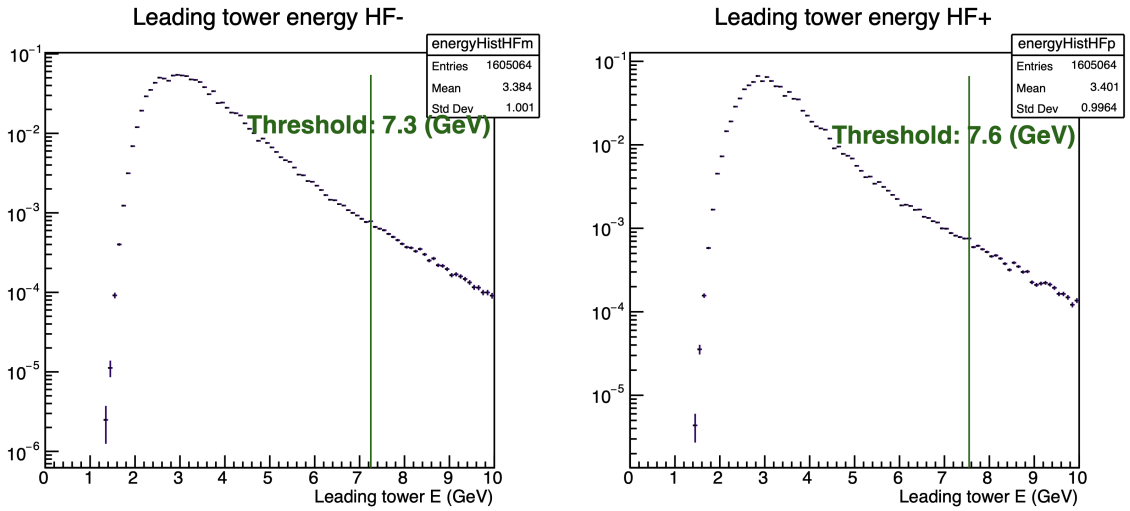

Figure 4.5 : Leading tower energy distributions from empty bunch crossing events in HF Minus (left) and HF Plus (right). The corresponding thresholds used in this analysis are shown as green vertical lines.

4.5 Muon Selection

4.5.1 Muon Selection

Muon candidates are reconstructed using the standard CMS muon reconstruction algorithm. Two types of muons are used in this analysis: "Soft Muon" and "Triggered Muon," as defined by the CMS Muon POG [59].

- **Soft Muon:**
  - Tracks must be high-purity.
  - At least 6 tracker layers in the silicon tracker.
  - At least one hit in the silicon pixel detector and matched with at least one segment in any muon station for both X and Y coordinates within 3σ.
  - The track's distance from the closest primary vertex must be less than 20 cm longitudinally and 3 mm transversely.

- **Triggered Muon:**
  - Must satisfy all "Soft Muon" criteria.
  - Must fire at least two muon stations at L1 trigger and pass trigger matching.

All muons in this analysis must pass the "Soft Muon" selection, with "Triggered Muons" being a subset of "Soft Muons."

4.5.2 Muon Kinematic Acceptance

The typical p_{T} of coherent J/ψ mesons is around 60 MeV/c, resulting in their decay muons being nearly back-to-back with a p_{T} of approximately 1.5 GeV/c. These muons are undetectable at mid-rapidity in CMS, as they cannot reach the muon detectors. Therefore, this analysis focuses on forward coherent J/ψ meson production.

The kinematic cut boundaries are approved by the CMS Muon POG. Fig. 4.6 shows the kinematic (p_{T}, η) distributions of soft muons (left) and triggered muons (right) compared to their respective acceptance cut boundaries. All reconstructed muon candidates are selected from J/ψ candidates with $2 < M_{\mu^+\mu^-} < 5$ GeV and rapidity within $1.6 < |y_{\mu^+\mu^-}| < 2.4$.

4.6 Event Classification

Coherent J/ψ meson photoproduction in PbPb UPCs is classified into three neutron multiplicity classes based on the number of neutrons emitted from the two colliding nuclei. This thesis follows the strategy in Ref. [58] to define the neutron multiplicity classes.

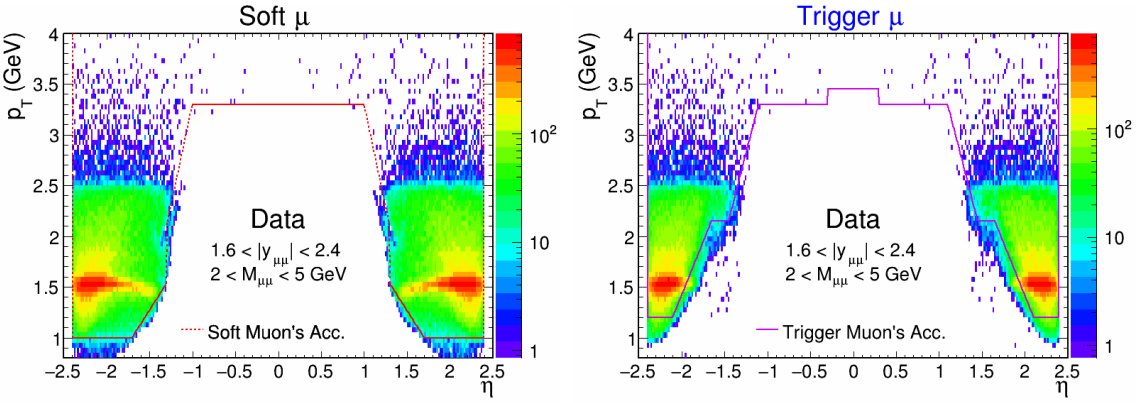

Figure 4.6 : Kinematic (p_{T}, η) distributions of soft muons (left) and triggered muons (right) compared to their acceptance cut boundaries. Reconstructed muon candidates are selected from J/ψ candidates with $2 < M_{\mu^+\mu^-} < 5\,\mathrm{GeV}$ and $1.6 < |y_{\mu^+\mu^-}| < 2.4$. The magenta curve represents the triggered muon acceptance boundary, while the red curve represents the soft muon acceptance boundary.

4.6.1 Neutron Multiplicity Classes

Forward neutron multiplicities are determined by analyzing the energy distributions (recorded as ADC) of neutrons deposited in the ZDCs. The ZDCs, located at $|\eta| > 8.3$, detect neutrons emitted from the colliding nuclei and consist of two detectors, one on each side of the interaction point.

The ZDC ADC distributions are fitted with multi-Gaussian functions. Fig. 4.7(a) shows the ADC distributions of the ZDC detectors: minus direction vs. plus direction for events containing at least one $\mu^+\mu^-$ pair. The plus and minus ZDC ADC distributions, fitted to multi-Gaussian functions, are shown in Figs. 4.7(b) and 4.7(c), respectively.

The fit assumes that the width of the 3n peak is no smaller than that of 2n. However, only 0n, 1n, and 2n can be reliably distinguished, as higher neutron peaks are not separable. The fit parameters indicate that the peak positions (μ_2) of 2n are

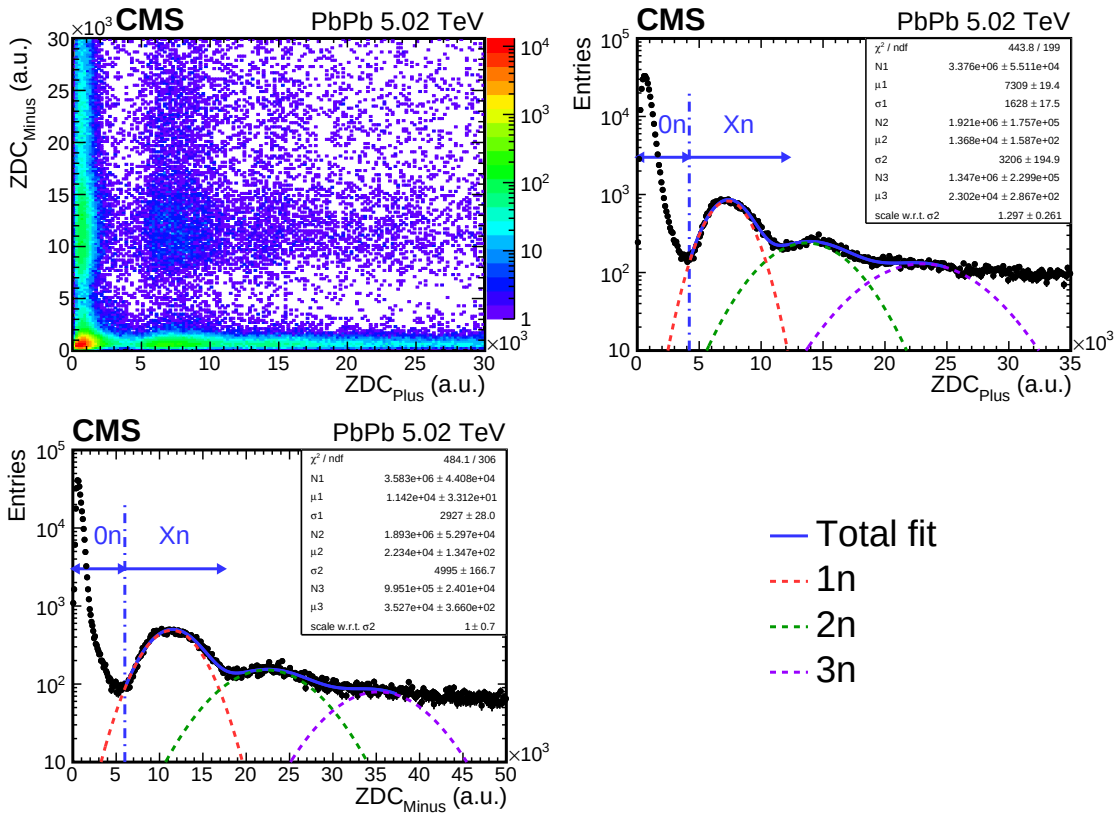

Figure 4.7 : (a) Minus vs. plus ZDC ADC distributions for events containing at least one $\mu^+\mu^-$ pair. (b) Plus ZDC ADC distributions fitted to multi-Gaussian functions. (c) Minus ZDC ADC distributions fitted to multi-Gaussian functions. Dashed lines indicate the fit ranges in plus and minus ZDC ADC distributions.

twice those of 1n, while the widths (σ_2) are approximately $\sqrt{2}$ to 2 times larger than those of 1n.

The ZDC noise distributions are studied using empty bunch crossing events triggered by no bunch crossing trigger. The noise contribution to the 1n peak is found to be $< 0.02\%$ for either side. Due to this negligible noise contribution, noise components are excluded from the fit used to extract neutron multiplicities.

4.6.2 Neutron Class Purity

The purity of neutron multiplicity classes is defined as the fraction of events in a given neutron multiplicity class that are correctly classified. The purity is determined by the ZDC ADC cuts. Since the efficiency and purity of 0n are nearly 100%, only the ADC cut for selecting 1n needs optimization.

The optimal cut is chosen to maximize the signal significance (proportional to efficiency $\times$ purity). Fig. 4.8 shows the ADC cut scan results for 1n purity and purity $\times$ efficiency as functions of efficiency on both sides. As purity is more relevant for this analysis, the optimal 1n ADC cut is further tightened to increase purity while maintaining efficiency above 90%.

4.6.3 Pileup due to EMD

When classifying events into different neutron multiplicity classes, pileup contributions from multiple electromagnetic dissociation (EMD) of PbPb pairs within the same bunch crossing become inevitable. The total hadronic cross section of PbPb ($\sigma_{\mathrm{PbPb}} \approx 7.7\,\mathrm{b}$) [32] is much smaller than the forward neutron production cross section from EMD ($\sigma_{\mathrm{EMD}} \approx 200\,\mathrm{b}$) [60, 61], making EMD the dominant source of pileup. These effects are studied using zero bias (ZB) events recorded under the same run conditions during the 2018 5.02 TeV PbPb collisions [58].

The single muon UPC trigger used in this analysis sampled the full luminosity. The ZB trigger, operating at a constant rate with a large pre-scale factor, is independent of luminosity and tied to the LHC clock. Consequently, the ZB trigger sampled luminosity has the same shape as the UPC trigger but is scaled by the pre-scale factor.

To estimate luminosity-dependent pileup effects in the UPC trigger, the ZB trigger

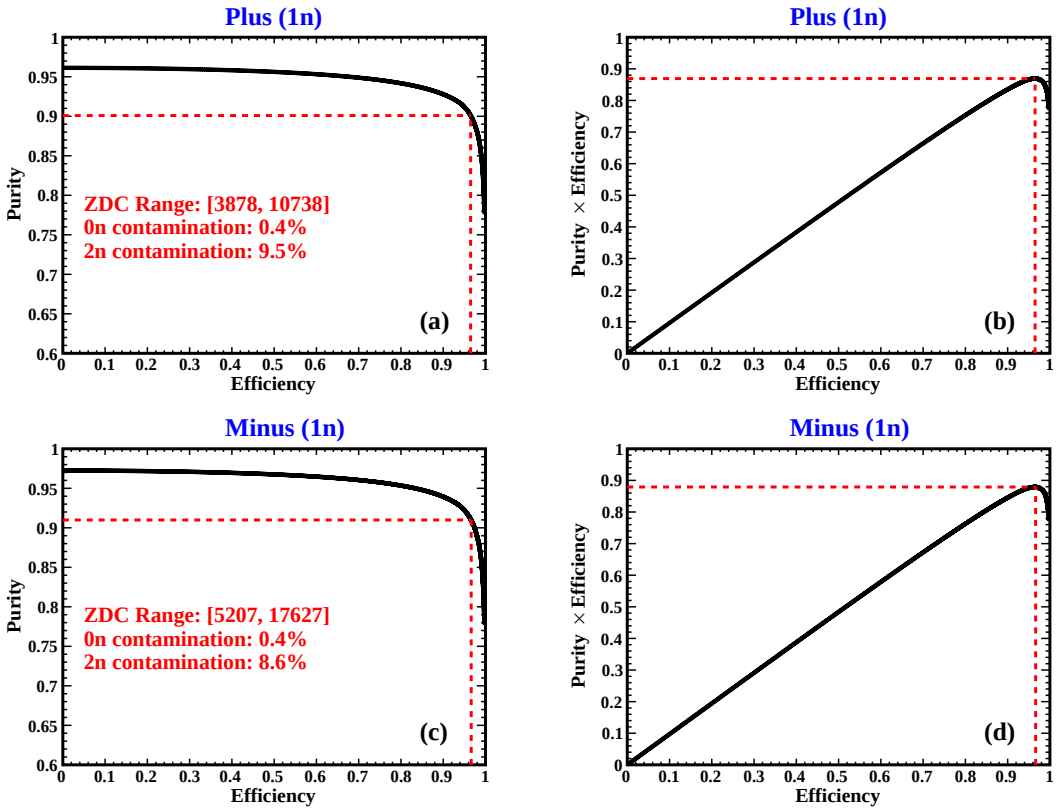

Figure 4.8 : (a) Purity as a function of efficiency for selected 1n with various plus ZDC ADC cuts. (b) Purity × Efficiency as a function of efficiency for selected 1n with various plus ZDC ADC cuts. (c) Purity as a function of efficiency for selected 1n with various minus ZDC ADC cuts. (d) Purity × Efficiency as a function of efficiency for selected 1n with various minus ZDC ADC cuts. Red dashed lines indicate the optimal ADC cut values.

Table 4.3 : Selection criteria for ZB events.

Event Selection Criteria
pprimaryVertexFilter & pclusterCompatibilityFilter
$HF^{\text{leading}}_{\text{Plus}} \leq 7.3\,\text{GeV}$ & $HF^{\text{leading}}_{\text{Minus}} \leq 7.6\,\text{GeV}$
$N^{\text{HP}}_{\text{trk}} == 0$
runID ≥ 326776

sampled luminosity is weighted to match the UPC trigger sampled luminosity for each luminosity section in every analyzed run. The weighted ZB events are selected using the criteria listed in Tab. 4.3 to suppress contributions from photon interactions and hadronic collisions. The ZDC response on both the plus and minus sides is then analyzed. If no Pb dissociation occurs in the selected ZB events, the ZDC should show no activity. Otherwise, the probability of forming neutron multiplicity bins from pure Pb dissociation (excluding $\gamma\gamma$ or γPb interactions) can be derived.

4.6.4 EMD Pileup Correction

The pileup contributions from EMD can be corrected using the migration matrix method. The migration matrix describes the probability of an event being classified into a certain neutron multiplicity class given its true neutron multiplicity. It is defined as:

$$\begin{pmatrix} N^{00} \\ N^{0X} \\ N^{X0} \\ N^{XX} \end{pmatrix}^{\textbf{Obs}} = \begin{pmatrix} P^{00}_{00} & 0 & 0 & 0 \\ P^{0X}_{00} & P^{0X}_{0X} & 0 & 0 \\ P^{X0}_{00} & 0 & P^{X0}_{X0} & P^{X0}_{XX} \\ P^{XX}_{00} & P^{XX}_{0X} & P^{XX}_{X0} & P^{XX}_{XX} \end{pmatrix} \begin{pmatrix} N_{00} \\ N_{0X} \\ N_{X0} \\ N_{XX} \end{pmatrix}^{\textbf{True}} . \tag{4.5}$$

Table 4.4 : Fractions of events detected as 0n0n, 0nXn, Xn0n, or XnXn in ZB events under the requirements listed in Tab. 4.3. These ZB events are weighted to match the luminosity shape of UPC-triggered events.

	f_{00}	f_{0X}	f_{X0}	f_{XX}
Fraction	0.8898	0.0531	0.0508	0.0063

Here, N^{ij} is the observed neutron multiplicity, N_{kl} is the true neutron multiplicity, and P_{kl}^{ij} is the migration matrix element describing the probability of an event with true neutron multiplicity kl being classified as ij. The migration matrix is estimated using ZB-triggered events and can be inverted to derive the true neutron multiplicity from the observed neutron multiplicity.

The ZDC response in selected ZB events (without any activity in the CMS tracker) is analyzed, and the corresponding fractions of ZB events are listed in Tab. 4.4.

The migration matrix elements (Eq. 4.5) can be estimated from the fractions in Tab. 4.4 as follows:

$$\begin{aligned}
P_{00}^{00} &= f_{00}, \\
P_{00}^{0X} &= f_{0X}, \quad P_{0X}^{0X} = f_{00} + f_{0X}, \\
P_{00}^{X0} &= f_{X0}, \quad P_{X0}^{X0} = f_{00} + f_{X0}, \\
P_{00}^{XX} &= f_{XX}, \quad P_{0X}^{XX} = f_{X0} + f_{XX}, \quad P_{X0}^{XX} = f_{0X} + f_{XX}, \\
P_{XX}^{XX} &= f_{00} + f_{0X} + f_{X0} + f_{XX} = 1.
\end{aligned} \tag{4.6}$$

For example, the migration matrix element P_{0X}^{XX} represents the probability of measuring XnXn when the true neutron multiplicity is 0nXn. This occurs in two cases: (1) 0nXn and Xn0n occur simultaneously, or (2) 0nXn and XnXn occur simultaneously. The probabilities for these cases are derived from the fractions f_{X0} and

f_{XX}, respectively. Other migration probabilities can be calculated similarly.

4.6.5 EMD Pileup Correction Method 2

Another method to estimate the pileup contributions from EMD is to use the Poisson distribution. The average numbers of 0nXn and XnXn events can be determined based on the fractions of events in the selected ZB events. The probability of observing k 0nXn or XnXn events within one bunch crossing follows the Poisson distribution:

$$\begin{aligned} P_{0X}[k] &= \frac{\mu_{0X}^k}{k!}\exp(-\mu_{0X}), \\ P_{XX}[k] &= \frac{\mu_{XX}^k}{k!}\exp(-\mu_{XX}), \end{aligned} \tag{4.7}$$

where μ_{0X} and μ_{XX} are the mean rates of 0nXn and XnXn events per bunch crossing, respectively. If no 0nXn or XnXn events occur in a bunch crossing, the probabilities are $P_{0X}[0] = \exp(-\mu_{0X})$ and $P_{XX}[0] = \exp(-\mu_{XX})$. Conversely, the probabilities of at least one 0nXn or XnXn event are $P_{0X} = 1-\exp(-\mu_{0X})$ and $P_{XX} = 1-\exp(-\mu_{XX})$.

The fractions of ZB events classified as 0n0n, 0nXn, and XnXn are given by:

$$\begin{aligned} f_{00} &= (1-P_{0X})^2 \cdot (1-P_{XX}), \\ f_{0X} &= P_{0X}(1-P_{XX})(1-P_{0X}), \\ f_{X0} &= f_{0X}, \\ f_{XX} &= P_{XX} + (1-P_{XX}) \cdot P_{0X}^2. \end{aligned} \tag{4.8}$$

The fractions f_{00}, f_{0X}, and f_{XX} can be measured in the selected ZB events. Solving these equations yields the probabilities and mean rates:

$$\begin{aligned} P_{0X} = 0.0552, \quad \mu_{0X} = 0.0568, \\ P_{XX} = 0.00371, \quad \mu_{XX} = 0.00371. \end{aligned} \tag{4.9}$$

This implies that, on average, there are 0.0568 0nXn events and 0.00371 XnXn events per bunch crossing. Using these probabilities, the relationship between the ob-

served and true numbers of events for 0n0n, 0nXn, and XnXn classes can be expressed as:

$$\begin{pmatrix} N^{00} \\ N^{0X} \\ N^{XX} \end{pmatrix} = \begin{pmatrix} (1-P_{0X})^2 \cdot (1-P_{XX}) & 0 & 0 \\ 2P_{0X}(1-P_{XX})(1-P_{0X}) & (1-P_{0X})(1-P_{XX}) & 0 \\ P_{XX}+P_{0X}^2-P_{XX}P_{0X}^2 & P_{XX}+P_{0X}(1-P_{XX}) & 1 \end{pmatrix} \begin{pmatrix} N_{00} \\ N_{0X} \\ N_{XX} \end{pmatrix}. \tag{4.10}$$

The true number of events or signal counts for each neutron class can be obtained by applying the inverse of this matrix to the observed counts.

4.7 Acceptance And Efficiency Corrections

The final measured J/ψ and ψ(2S) raw yields are corrected for detector acceptance and reconstruction efficiency. These correction factors are estimated using STARLIGHT + CMS GEANT4 simulation samples.

The acceptance correction factor is defined as the ratio of the number of events passing the acceptance cuts to the total number of generated events:

$$Acc(\mathrm{J}/\psi) = \frac{N_{\mathrm{Acc}}(\mathrm{J}/\psi)}{N_{\mathrm{Gen}}(\mathrm{J}/\psi)}. \tag{4.11}$$

The muon reconstruction and trigger efficiencies are derived from MC simulations and corrected using scaling factors obtained through the data-driven tag-and-probe (TnP) technique:

$$Eff(\mathrm{J}/\psi) = \epsilon(\mathrm{evtSel}) \times \epsilon_{\mathrm{MC}}(\mathrm{J}/\psi) \otimes \frac{\epsilon(\mu^+)^{\mathrm{TnP}}_{\mathrm{Data}} * \epsilon(\mu^-)^{\mathrm{TnP}}_{\mathrm{Data}}}{\epsilon(\mu^+)^{\mathrm{TnP}}_{\mathrm{MC}} * \epsilon(\mu^-)^{\mathrm{TnP}}_{\mathrm{MC}}}. \tag{4.12}$$

Here, ϵ(evtSel) represents the event-level selection efficiency, defined as the fraction of events passing the selection criteria. The J/ψ reconstruction efficiency, estimated from MC samples, is denoted as $\epsilon_{\mathrm{MC}}(\mathrm{J}/\psi)$ and defined as:

$$\epsilon_{\mathrm{MC}}(\mathrm{J}/\psi) = \frac{N^{\mathrm{muID,Trig,Mass}}_{\mathrm{Acc}}}{N_{\mathrm{Acc}}}. \tag{4.13}$$

Reconstructed signal events are those where the trigger fired, both muons are within the detector's kinematic acceptance (as defined in Eq. 4.11), and all muon quality selection cuts are satisfied. The denominator includes generated dimuons where both daughter muons are within the kinematic acceptance.

The $\otimes$ symbol in Eq. 4.12 indicates that data-to-MC ratios of single-muon efficiencies, obtained via the TnP method as functions of η and p_{T}, are applied to both muons (partner and triggered) as scale factors to reweight the reconstructed dimuons in the MC.

The final rapidity window, $1.6 < |y| < 2.4$, is chosen based on constraints from both reconstruction efficiency and detector acceptance corrections. Efficiency at mid-rapidity ($y < 1.6$) is nearly zero, while $|y| < 2.4$ is limited by the muon trigger acceptance.

The acceptance and efficiency correction factors are detailed in Sections 4.7.1 and 4.7.2.

4.7.1 Acceptance correction factor

Fig. 4.9 and Fig. 4.10 show the acceptance correction factors (Eq. 4.11) for the inclusive coherent J/ψ (AnAn) and ψ(2S) (AnAn) events. The corresponding factors for other neutron multiplicity classes (e.g., 0n0n, 0nXn, XnXn) can be calculated similarly.

4.7.2 Efficiency correction factor

Fig. 4.11 and Fig. 4.12 show the efficiency correction factors (Eq. 4.12) for the inclusive coherent J/ψ (AnAn) and ψ(2S) (AnAn) events. The corresponding factors for other neutron multiplicity classes (e.g., 0n0n, 0nXn, XnXn) can be calculated similarly.

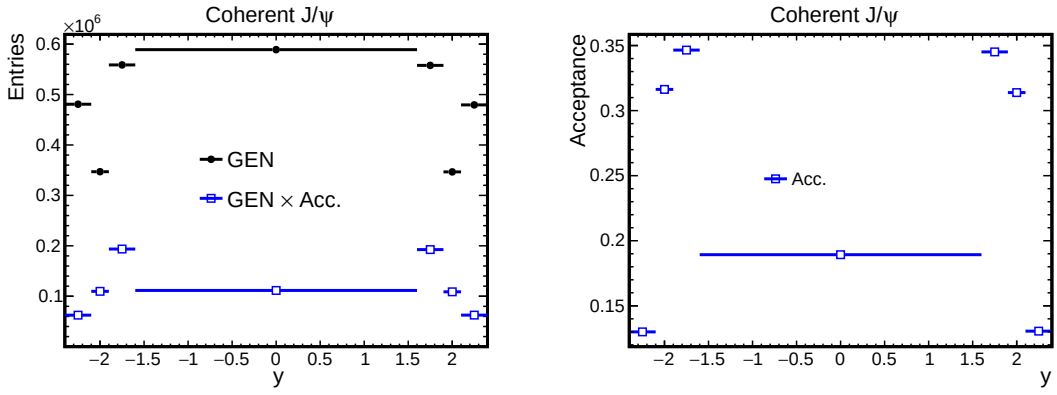

Figure 4.9 : Distributions (left) and acceptance correction factors (right) for inclusive coherent J/ψ (AnAn).

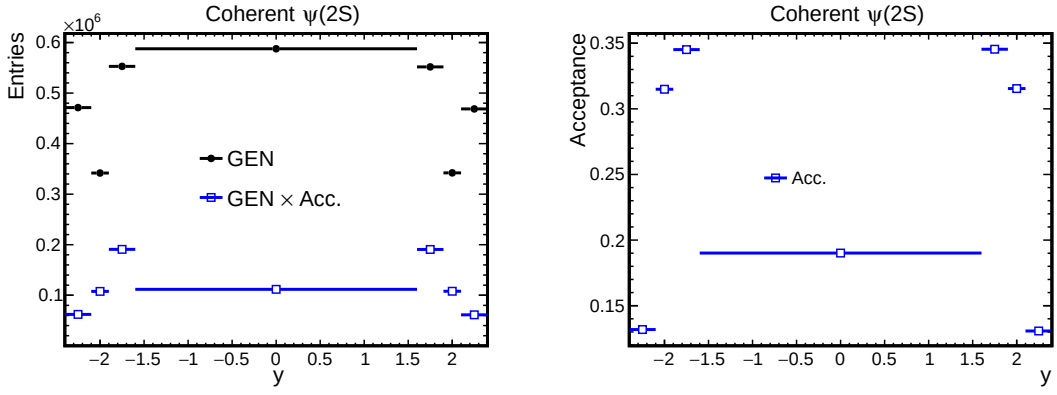

Figure 4.10 : Distributions (left) and acceptance correction factors (right) for inclusive coherent ψ(2S) (AnAn).

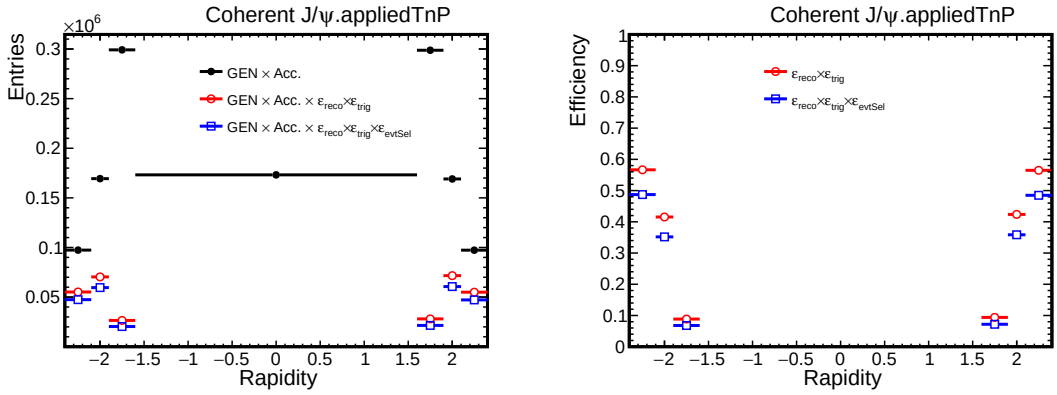

Figure 4.11 : Distributions (left) and efficiency correction factors (right) for the inclusive coherent J/ψ (AnAn).

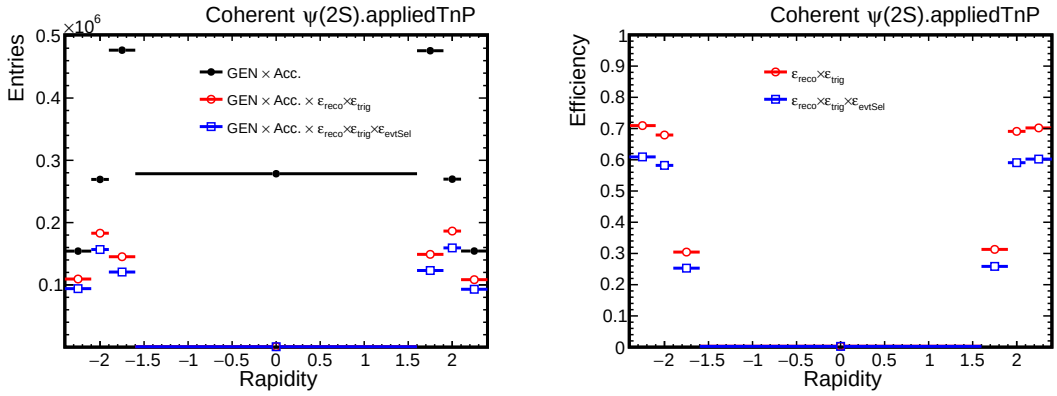

Figure 4.12 : Distributions (left) and efficiency correction factors (right) for the inclusive coherent ψ(2S) (AnAn).

The efficiency factors before and after the TnP correction are shown in Fig. 4.13.

4.8 Raw Signal Yields and Disentangling Strategy

4.8.1 Raw Signal Yields

After selecting pure muon candidates, we reconstruct the $\mu^+\mu^-$ pair to measure the J/ψ meson. The $\mu^+\mu^-$ pairs are formed within the same event, requiring exactly

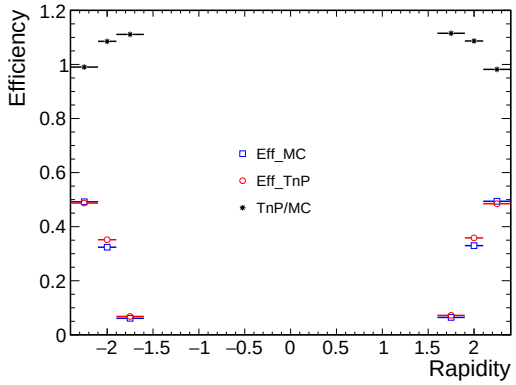

Figure 4.13 : Comparison of efficiency correction factors before and after the TnP correction. The ratio between the two is also shown.

two muon candidates. Wrong-sign pairs are negligible in this analysis, as UPC events ($\sim 100\%$) do not produce same-sign muon pairs. The main requirements for the muon pair are as follows:

- At least one muon must be a triggered muon.
- The two muons must form a valid vertex with a probability greater than 10^{-6}.
- The pair's kinematics (p_{T} and mass) must lie within the defined acceptance region.
- $|y_{\mu^+\mu^-}| < 2.4$.

4.8.2 Strategy to Disentangle Different Physics Processes

In this analysis, the J/ψ and ψ(2S) signals are extracted within an invariant mass window of $2.60 < M_{\mu^+\mu^-} < 4.2\,\mathrm{GeV}/c^2$ (approximately -11σ to $+24\sigma$ from the J/ψ mean peak). Several known contribution sources exist in this range. The contributing physics processes are:

- Direct coherent J/$\psi \to \mu^+\mu^-$
- Direct coherent ψ(2S) $\to \mu^+\mu^-$
- Direct incoherent J/$\psi \to \mu^+\mu^-$ with nucleon dissociation
- Direct incoherent J/$\psi \to \mu^+\mu^-$ without nucleon dissociation
- Direct incoherent ψ(2S) $\to \mu^+\mu^-$ with nucleon dissociation
- Direct incoherent ψ(2S) $\to \mu^+\mu^-$ without nucleon dissociation
- Feeddown J/ψ from coherent ψ(2S) $\to$ J/$\psi \to \mu^+\mu^-$
- Feeddown J/ψ from incoherent ψ(2S) $\to$ J/$\psi \to \mu^+\mu^-$
- $\gamma\gamma \to \mu^+\mu^-$, dimuon continuum (pure QED process)

Although there are eight distinct contribution sources, the invariant mass spectra can be grouped into three main components: J/ψ, ψ(2S), and the QED dimuon continuum. Full disentanglement of these contributions is achieved by analyzing the p_{T} spectra within the J/ψ mass window ($2.95 < M_{\mu^+\mu^-} < 3.25\,\mathrm{GeV}/c^2$).

The raw inclusive invariant mass distribution is fitted using the Crystal Ball function, defined as:

$$f(x;\alpha,n,\mu,\sigma) = N \cdot \begin{cases} \exp\left(-\frac{(x-\mu)^2}{2\sigma^2}\right), & \frac{x-\mu}{\sigma} > -\alpha \\ A \cdot (B - \frac{x-\mu}{\sigma})^{-n}, & \frac{x-\mu}{\sigma} \leqslant -\alpha \end{cases}, \tag{4.14}$$

where:

$$A = \left(\frac{n}{|\alpha|}\right)^n \cdot \exp\left(-\frac{|\alpha|^2}{2}\right), \quad B = \frac{n}{|\alpha|} - |\alpha|\,,$$

$$N = \frac{1}{\sigma(C+D)}, \quad C = \frac{n}{|\alpha|} \cdot \frac{1}{n-1} \cdot \exp\left(-\frac{|\alpha|^2}{2}\right), \quad D = \sqrt{\frac{\pi}{2}}\left(1 + \mathrm{erf}\left(\frac{|\alpha|}{\sqrt{2}}\right)\right).$$

The tail-related parameters are shared between J/ψ and ψ(2S), as they are primarily determined by the J/ψ raw signal due to its higher yield. The mean of the ψ(2S) mass distribution is constrained by the J/ψ mean mass and their mass ratio: $\mu_{\psi(2S)} = \mu_{J/\psi} \times (M_{\psi(2S)}/M_{J/\psi})$. Similarly, the width of the ψ(2S) mass distribution is constrained as $\sigma_{\psi(2S)} = \sigma_{J/\psi} \times (M_{\psi(2S)}/M_{J/\psi})$. The QED continuum is smoothly distributed across the mass region and is modeled using a third-degree polynomial. The J/ψ Crystal Ball function parameters are initialized using MC shapes, incorporating CMS detector acceptance, efficiency, and momentum resolution.

The p_{T} fitting is performed in the J/ψ signal-dominant mass region ($2.95 < M_{\mu^+\mu^-} < 3.25\,\mathrm{GeV}/c^2$). Each source has a distinct p_{T} shape, which is key to disentangling their contributions. The p_{T} fitting algorithm, established in previous coherent J/ψ measurements, uses template fitting. Each source contributes its own distribution shape to the overall p_{T} distribution. Templates for direct coherent J/ψ, feeddown J/ψ from coherent ψ(2S), incoherent J/ψ without nucleon dissociation, and feeddown J/ψ from incoherent ψ(2S) are simulated using STARlight + CMS Geant4. The incoherent J/ψ with nucleon dissociation is modeled using the H1 and ALICE shape $\mathrm{d}N/\mathrm{d}p_{\mathrm{T}} \sim p_{\mathrm{T}} \cdot (1 + (b_{\mathrm{pd}}/n_{\mathrm{pd}}) \cdot p_{\mathrm{T}}^2)^{-n_{\mathrm{pd}}}$. Unlike ALICE and H1, where b_{pd} and n_{pd} are fixed, these parameters are left free in this analysis, as acceptance, efficiency, and kinematics affect the p_{T} shapes.

STARlight templates are not perfect for describing data in the low-p_{T} region ($p_{\mathrm{T}} < 0.20\,\mathrm{GeV}/c^2$), as demonstrated in this and previous studies (e.g., ALICE [62, 51]). In this analysis, p_{T} fitting performance in the coherent J/ψ dominant region is improved by using coherent J/ψ p_{T} templates simulated with an increased Pb radius of 1 fm. This accounts for the increased effective diffraction radius of VM photonuclear coherent production due to quantum interference effects [63].

4.8.3 Signal Extraction

Although the different sources have distinct p_{T} distributions, relying solely on these shapes is insufficient for disentangling them. A better approach is to utilize the significant mass distributions of J/ψ, ψ(2S), and QED, allowing us to control the normalization of each component. The p_{T} distribution is then fitted with these normalization constraints and templates to decouple different sources. The normalizations of coherent J/ψ, incoherent J/ψ, and incoherent J/ψ with nucleon dissociation are treated as free parameters in the fitting. The QED dimuon continuum yield can be determined from the mass fit, using the sideband close to the J/ψ mass for its p_{T} distribution. The normalization of coherent and incoherent feeddown J/ψ is constrained by the normalization of primary coherent and incoherent J/ψ, according to the feeddown fractions (f_{D}) extracted from raw inclusive J/ψ and ψ(2S) yields in the invariant mass fit. Feeddown contributions are important not only for the coherent J/ψ measurement but also for the incoherent J/ψ measurement. Thus, we first need to obtain f_{D}. The invariant mass fit for pairs with $p_{\mathrm{T}} < 0.20\,\mathrm{GeV}/c^2$, where the coherent J/$\psi$ contribution is dominant, is performed to extract the raw inclusive yields of N(J/ψ) and $N(\psi(2\mathrm{S}))$, as well as the raw ratio factors R_N, f_{D}, and the physics ratio factor R. The ratio of raw inclusive ψ(2S) over raw inclusive J/ψ is defined as:

$$R_N = \frac{N(\psi(2\mathrm{S}))}{N(\mathrm{J}/\psi)}. \tag{4.15}$$

This ratio can be expressed in terms of their production cross sections, reconstruction efficiencies, and associated decay branching ratios:

$$R_N = \frac{\sigma_{\psi(2\mathrm{S})} \cdot \mathcal{B}_{\psi(2\mathrm{S})\to\mu^+\mu^-} \cdot \epsilon_{\psi(2\mathrm{S})}}{\sigma_{\mathrm{J}/\psi} \cdot \mathcal{B}_{\mathrm{J}/\psi\to\mu^+\mu^-} \cdot \epsilon_{\mathrm{J}/\psi} + \sigma_{\psi(2\mathrm{S})} \cdot \mathcal{B}_{\psi(2\mathrm{S})\to\mathrm{J}/\psi} \cdot \epsilon_{\psi(2\mathrm{S})\to\mathrm{J}/\psi} \cdot \mathcal{B}_{\mathrm{J}/\psi\to\mu^+\mu^-}}. \tag{4.16}$$

With the R_N factor, we can derive the physics ratio R of coherent ψ(2S) over

coherent J/ψ:

$$R = \frac{\sigma_{\psi(2S)}}{\sigma_{J/\psi}}. \tag{4.17}$$

Expressing R as a function of R_N, efficiencies, and decay branching ratios gives:

$$R = \frac{R_N \cdot \mathcal{B}_{J/\psi\to\mu^+\mu^-} \cdot \epsilon_{J/\psi}}{\mathcal{B}_{\psi(2S)\to\mu^+\mu^-} \cdot \epsilon_{\psi(2S)} - R_N \cdot \mathcal{B}_{\psi(2S)\to J/\psi} \cdot \epsilon_{\psi(2S)\to J/\psi} \cdot \mathcal{B}_{J/\psi\to\mu^+\mu^-}}. \tag{4.18}$$

Then, the feeddown fraction of coherent J/ψ from coherent ψ(2S) can be calculated based on the R factor and their corresponding efficiency and decay branching ratio as follows:

$$f_D = \frac{N(J/\psi \text{ from coherent } \psi(2S) \text{ feeddown})}{\text{primary coherent } J/\psi} = R \cdot \frac{\epsilon_{\psi(2S)\to J/\psi}}{\epsilon_{J/\psi}} \cdot \mathcal{B}_{\psi(2S)\to J/\psi}. \tag{4.19}$$

The reconstruction efficiencies can be obtained using well-established simulation techniques, while the decay branching ratios are quoted from the 2022 PDG [64]:

- $\mathcal{B}_{J/\psi\to\mu^+\mu^-} = 5.961 \pm 0.033\%$.
- $\mathcal{B}_{\psi(2S)\to\mu^+\mu^-} = 0.809 \pm 0.06\%$.
- $\mathcal{B}_{\psi(2S)\to J/\psi} = 61.6 \pm 0.6\%$.

Thus, by fitting the mass region dominated by coherent production, we obtain the raw inclusive yields of N(J/ψ) and $N(\psi(2S))$, as well as the raw ratio factors R_N, f_D, and the physics ratio factor R. We can then proceed to the p_T fit as the final step in disentangling the different physics processes.

The details of how to constrain the fitting parameters in the p_T fitting are as follows:

- The number of coherent ψ(2S) decayed J/ψ is constrained by: $N^{coh}_{\text{feeddown J/}\psi} = N^{coh}_{J/\psi} \cdot f_D$.

- The number of incoherent $\psi(2S)$ decayed J/ψ is constrained by: $N^{\rm incoh}_{\rm feeddown\ J/\psi} = N^{\rm incoh}_{\rm J/\psi} \cdot f_{\rm D}$.

- Three free normalization parameters:

  - Number of coherent J/ψ $N^{\rm coh}_{\rm J/\psi}$.
  - Number of incoherent J/ψ $N^{\rm incoh}_{\rm J/\psi}$ without nucleon dissociation.
  - Number of incoherent J/ψ $N^{\rm incoh}_{\rm J/\psi}$ with nucleon dissociation.

- The QED dimuon continuum yield $N_{\rm QED}$ can be well determined by fitting the full-$p_{\rm T}$ invariant mass distribution, while its $p_{\rm T}$ distribution can be obtained from the sideband close to the J/ψ mass.

In the $p_{\rm T}$ fitting, the main goal is to extract the incoherent J/ψ contribution in the coherent J/ψ mass dominant region. After fitting the $p_{\rm T}$ distribution, we calculate the total fraction of incoherent J/ψ, including both with and without nucleon dissociation, within the $p_{\rm T} < 0.20\,{\rm GeV}/c^2$ region. This fraction is defined as:

$$f_{\rm I} = \frac{\text{incoherent J/}\psi}{\text{coherent J/}\psi}. \tag{4.20}$$

The final coherent J/ψ production cross section is then calculated as:

$$\frac{{\rm d}\sigma^{\rm coh}_{\rm J/\psi}}{{\rm d}y} = \frac{N^{\rm coh}_{\phi}}{(1+f_{\rm I}+f_{\rm D})\cdot\epsilon_{\rm J/\psi}\cdot\mathcal{B}_{\rm J/\psi\to\mu^+\mu^-}\cdot\mathcal{L}_{int}\cdot\Delta y}. \tag{4.21}$$

Similarly, the coherent $\psi(2S)$ production cross section is:

$$\frac{{\rm d}\sigma^{\rm coh}_{\psi(2S)}}{{\rm d}y} = \frac{N^{\rm coh}_{\psi(2S)}}{(1+f_{\rm I})\cdot\epsilon_{\psi(2S)}\cdot\mathcal{B}_{\psi(2S)\to\mu^+\mu^-}\cdot\mathcal{L}_{int}\cdot\Delta y}. \tag{4.22}$$

The mass fits for the signals within $p_{\rm T} < 0.20\,{\rm GeV}/c^2$ for each neutron class are shown in Fig. 4.14.

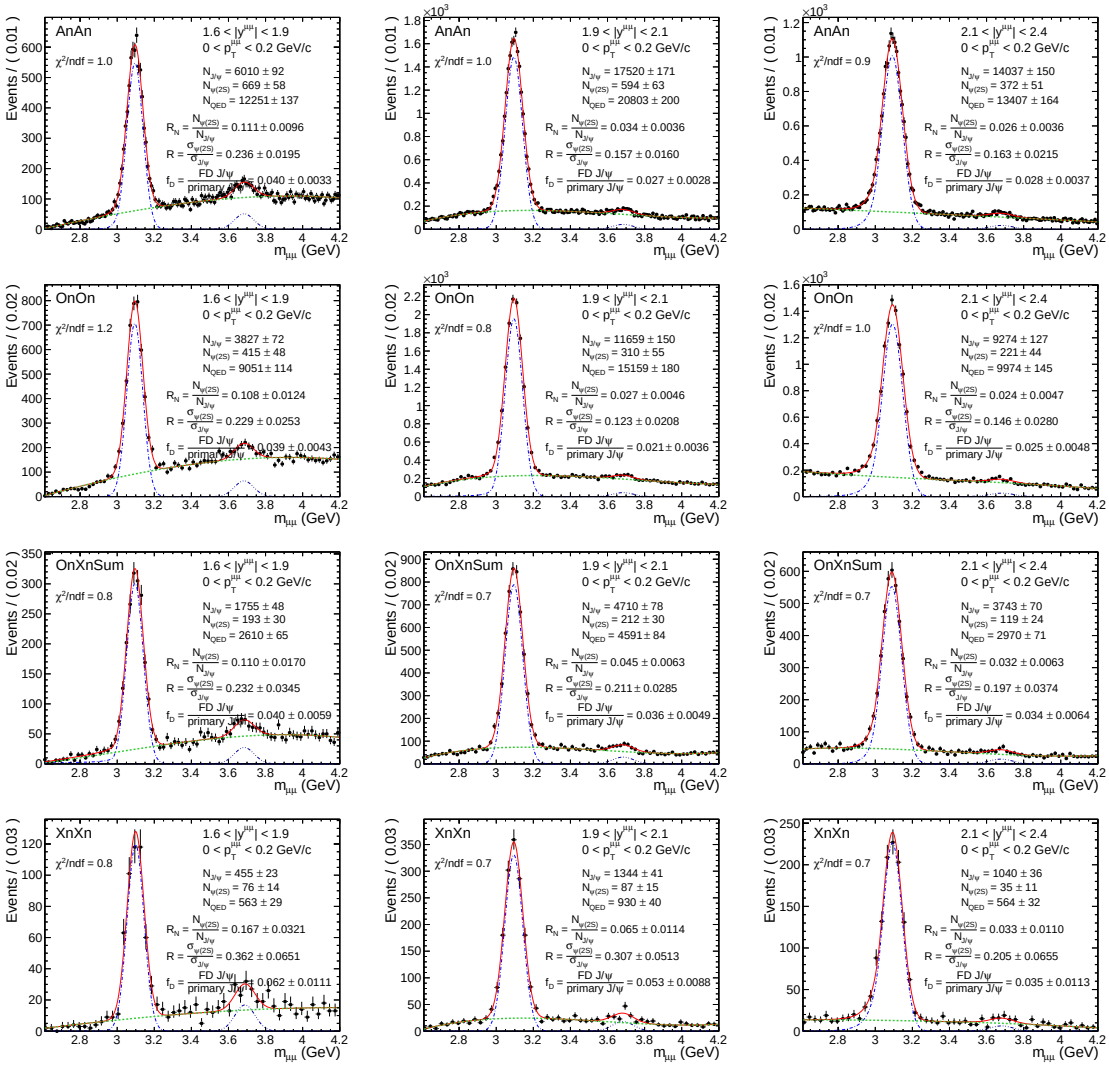

Figure 4.14 : Mass fit of signals within $p_{\mathrm{T}} < 0.20\,\mathrm{GeV}/c$ for the neutron class AnAn, 0n0n, 0nXnSum (0nXn+Xn0n), and XnXn.

4.8.4 p_{T} Fit Within the J/ψ Mass Window

Fig. 4.15 shows the p_{T} fit of signals within the J/ψ mass window ($2.95 < M_{\mu^+\mu^-} < 3.25\,\mathrm{GeV}/c^2$). The average fraction of incoherent J/ψ contributions is about 3%, increasing from 0n0n ($\sim 0.5\%$) to XnXn ($\sim 10\%$). The fitting performance is generally very good, as indicated by the χ^2/ndf and the pull histogram, especially for the neutron classes 0nXn and XnXn. However, the data around $p_{\mathrm{T}} \approx 0.30\,\mathrm{GeV}/c$ are higher than the fitting curves for the neutron classes AnAn and 0n0n. This small "bump" structure was also observed in previous ALICE publications [62, 51]. Considering that the coherent J/ψ is dominated by the 0n0n class for AnAn, while the 0nXn and XnXn classes have relatively larger contributions from incoherent J/ψ, this bump structure is more significant when the coherent J/ψ contributions are relatively higher.

To assess the impact of this imperfect fitting on the coherent J/ψ signal extraction, we changed the coherent J/ψ dominant p_{T} range to $p_{\mathrm{T}} < 0.30\,\mathrm{GeV}/c$ from $p_{\mathrm{T}} < 0.20\,\mathrm{GeV}/c$. The resulting uncertainties are found to be smaller than 2% on the coherent J/ψ yield extraction, as expected, since the yield of the bump is about two orders of magnitude lower than the main coherent J/ψ p_{T} peak.

4.9 Photon Flux

STARLIGHT is used to calculate the photon flux distribution for the J/ψ and ψ(2S) photoproduction processes. As STARLIGHT is open-source software, we modified the source code to print out the photon flux for our analysis. We run STARLIGHT with Run 2 energy to simulate the photoproduction and decay of J/ψ VM final states through the $\mu^+\mu^-$ channel. In nucleus–nucleus collisions, the flux values generated by STARLIGHT depend on the nucleon–nucleon interaction cross-section $\sqrt{s_{\mathrm{NN}}}$ and

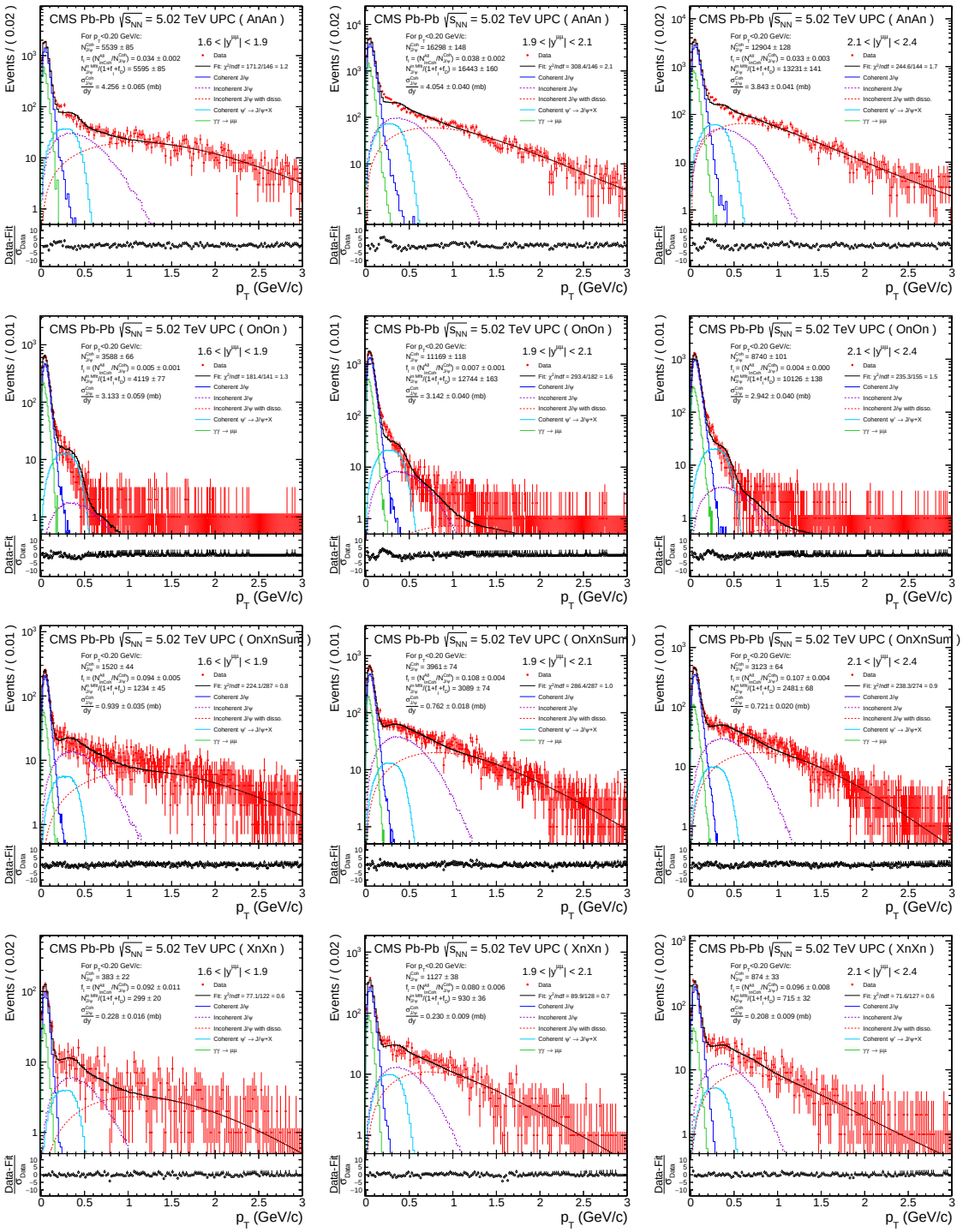

Figure 4.15 : p_{T} fit of $\mu^{+}\mu^{-}$ pairs falling within the J/ψ mass window ($2.95 < m_{\mu^{+}\mu^{-}} < 3.25\,\mathrm{GeV}/c^{2}$) for the neutron classes AnAn, 0n0n, 0nXnSum (0nXn+Xn0n), and XnXn.

the nuclear overlap function calculated from the nuclear density profiles [25]. In STARLIGHT, the nuclear densities are assumed to follow the Woods–Saxon distribution in Eq. 2.23. Since the outcome of this analysis highly depends on the calculation of the flux and its uncertainty, we made the following changes, taking the updated values and uncertainties from [65], with respect to the default values in STARLIGHT:

- $\sigma_{\mathrm{NN}} = 68.3 \pm 1.2\,\mathrm{mb}$
- $R = 6.67 \pm 0.03\,\mathrm{fm}$
- $a = 0.56 \pm 0.03\,\mathrm{fm}$

In STARLIGHT, one may require that one or both nuclei break up. This requirement is handled by the input parameter `BREAKUP_MODE` [25]:

- `BREAKUP_MODE = 2`: Requires Coulomb break-up of both nuclei, with no restriction on the number of neutrons emitted by either nucleus (XnXn).
- `BREAKUP_MODE = 4`: Requires no Coulomb break-up (0n0n).
- `BREAKUP_MODE = 5`: No restriction on Coulomb break-up (AnAn).
- `BREAKUP_MODE = 7`: Requires at least one Coulomb break-up on only one of the nuclei (0nXn + Xn0n).

Different `BREAKUP_MODE` settings affect the photon flux, as shown in Fig. 4.16.

4.10 Systematic Uncertainties

The systematic uncertainties on the coherent J/ψ photoproduction cross section and nuclear suppression factor are summarized in this section.

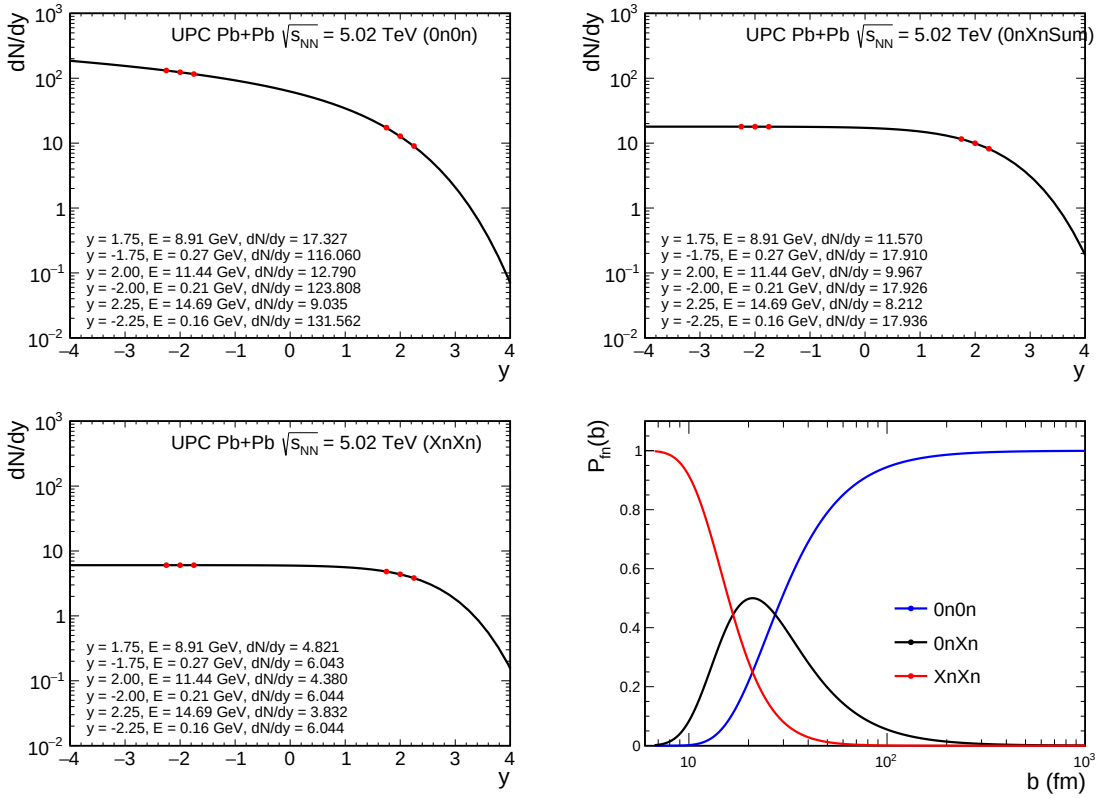

Figure 4.16 : The photon flux $N(y)$ for neutron configurations 0n0n, 0nXnSum (0nXn+Xn0n), and XnXn from STARLIGHT. The bottom right plot shows the impact parameter–dependent probability of a particular forward neutron configuration from STARLIGHT.

The systematic uncertainties in this analysis are categorized into several sources, each contributing to the total uncertainty in the measured quantities: the rapidity differential cross section ($\mathrm{d}\sigma/\mathrm{d}y$), the photoproduction cross section per photon-nucleus interaction (σ), and the nuclear suppression factor (R). The total systematic uncertainty is obtained by summing the individual contributions in quadrature. Below is a summary of the key sources of systematic uncertainties:

- **Luminosity:** The uncertainty in the integrated luminosity is estimated to be 1.5% [30].
- **Neutron pileup corrections:** The difference in the final results obtained using two different methods for neutron pileup corrections, discussed in Sec. 4.6.4 and Sec. 4.6.5, is taken as the systematic uncertainty.
- **Decay branching ratio:** The uncertainty in the decay branching ratio of J/ψ to $\mu^+\mu^-$ is taken from the PDG value, which is approximately 0.55% [64].
- **Efficiency corrections:** The uncertainties associated with the efficiency corrections are derived from the official CMS TnP scale factors.
- **HF threshold:** The uncertainty due to the HF threshold is estimated by loosening the HF cuts and taking the differences as the uncertainty.
- **IA:** A constant uncertainty of 5.4% is determined from fitting worldwide experimental data [26].
- **Photon flux:** The uncertainties in photon flux are estimated by varying the Pb nucleus radius ($R = 6.67 \pm 0.03\,\mathrm{fm}$) and nuclear skin thickness ($a = 0.56 \pm 0.03\,\mathrm{fm}$) [65]. Additionally, an uncertainty of 5.5% is considered due to the EM dissociation cross section [66].

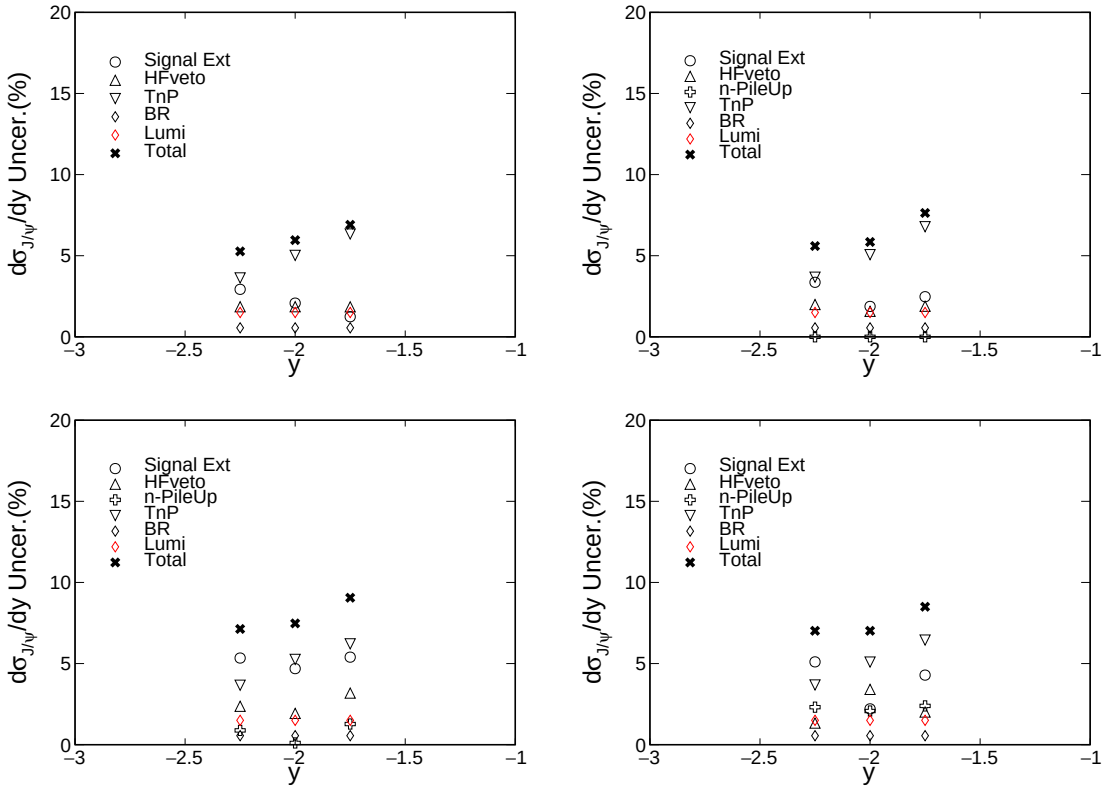

Figure 4.17 : Systematic uncertainties for the rapidity differential photoproduction cross section $\mathrm{d}\sigma/\mathrm{d}y$ in the neutron configurations AnAn, 0n0n, 0nXnSum, and XnXn.

- **Signal extraction:** The systematic uncertainties from signal extraction include variations in signal shape, signal parameters, mass fitting range, background shape, QED p_{T} shape, p_{T} template, and p_{T} cut window for coherent J/ψ yield counting.

The systematic uncertainties for the rapidity differential cross section are shown in Fig. 4.17. The total systematic uncertainty is summarized in Fig. 4.18.

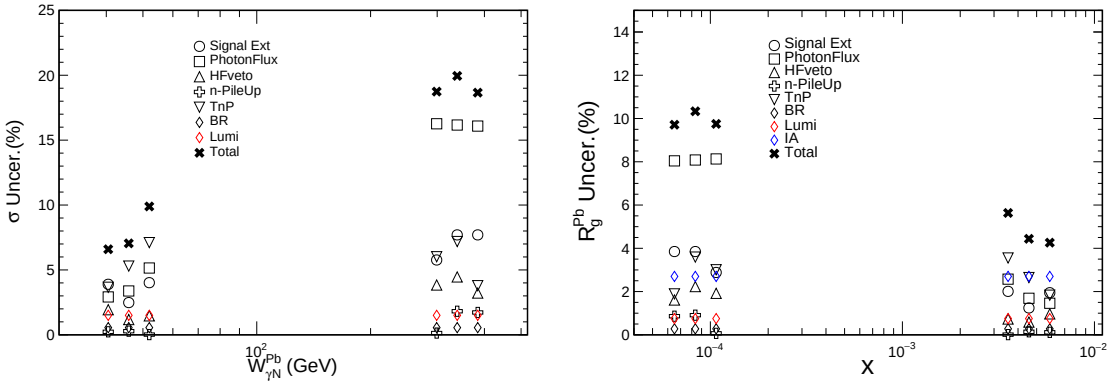

Figure 4.18 : Each source of systematic uncertainty for σ (left) and R (right).

4.10.1 Covariance Matrix

The covariance matrix for the systematic uncertainties is calculated to quantify the correlations between different sources of uncertainty. The covariance matrix is constructed using the following equations:

$$V_{ij} = \left|\sigma_i^{\text{nominal}} - \sigma_i^{\text{varied}}\right| \cdot \left|\sigma_j^{\text{nominal}} - \sigma_j^{\text{varied}}\right|, \tag{4.23}$$

for fully correlated uncertainties, and

$$V_{ij} = \left(\sigma_i^{\text{nominal}} - \sigma_i^{\text{varied}}\right)\left(\sigma_j^{\text{nominal}} - \sigma_j^{\text{varied}}\right), \tag{4.24}$$

for partially correlated uncertainties. The covariance matrix for the statistical uncertainties is extracted from the TF2 fitting and is shown in Fig. 4.19. The summed covariance matrix for σ is also shown in Fig. 4.19. Fig. 4.19 displays the covariance matrix for the statistical uncertainties (left), extracted from the TF2 fitting, and the summed covariance matrix for σ (right), which includes all sources of systematic and statistical uncertainties.

The covariance matrix for the photon flux is calculated by multiplying the differences of flux values with respect to the default flux value used in this analysis.

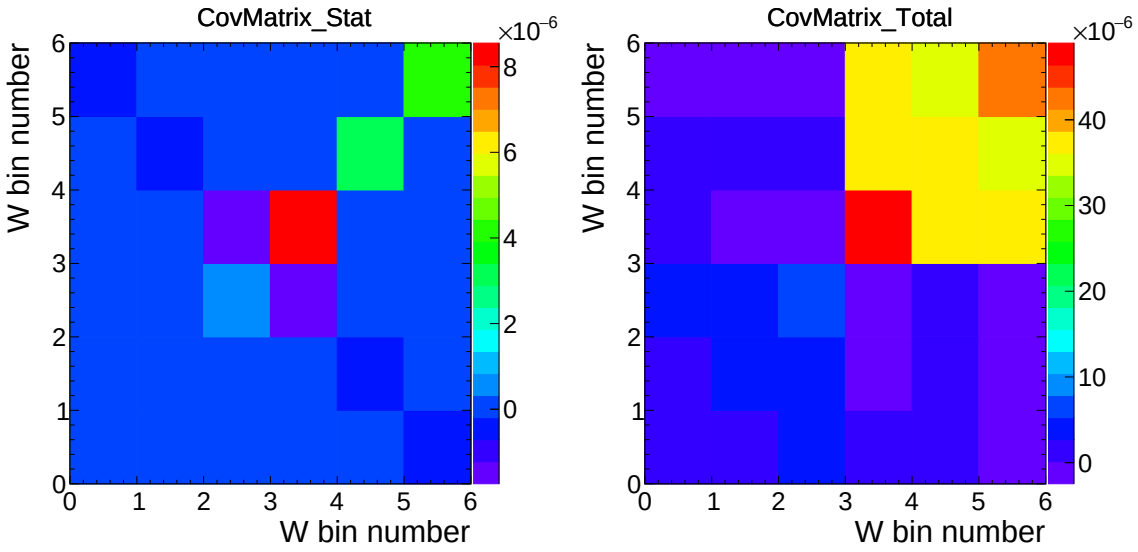

Figure 4.19 : The statistical covariance matrix for σ (left) and the summed covariance matrix for σ (right).

The absolute flux errors are determined by taking the largest difference between the flux values for each of the two sources separately. The final errors are summed in quadrature, and the covariance matrix is obtained as the outer product of the final errors. The covariance matrix for the photon flux is shown in Fig. 4.20.

4.11 Results

4.11.1 Coherent $d\sigma_{J/\psi}/dy$ in Different Neutron Classes

The first experimental measurements of the coherent J/ψ production cross section as a function of rapidity in different neutron multiplicity classes are reported in Fig. 4.21. The CMS data are compared to various theoretical model calculations and to experimental data from ALICE [50, 51] and LHCb [53] for inclusive neutron multiplicities.

For the AnAn case, the CMS data follow the trend observed in the ALICE and LHCb forward rapidity data, while also covering a previously unexplored rapidity

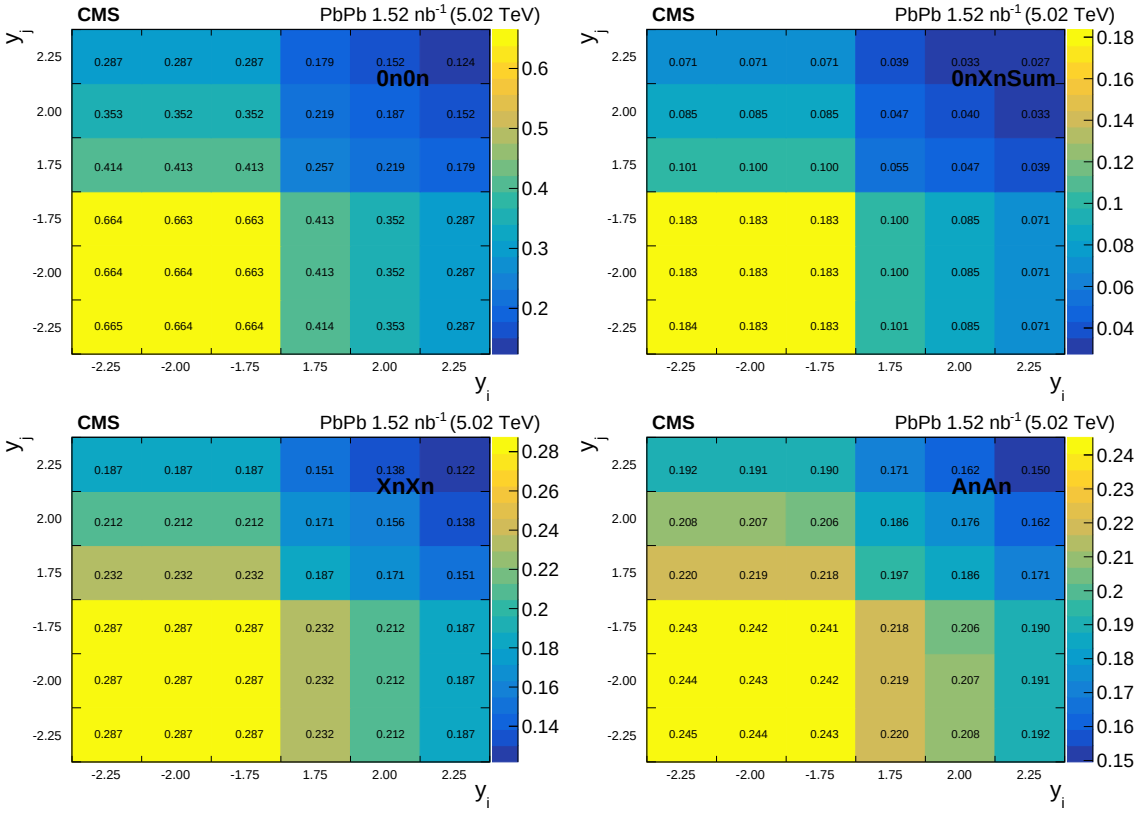

Figure 4.20 : The covariance matrix for the photon flux.

region. The leading twist perturbative QCD approach (LTA) [56], which accounts for nuclear shadowing effects, provides predictions for each neutron multiplicity class, for both weak and strong shadowing scenarios. The LTA calculations tend to underestimate the data for all neutron multiplicity classes, particularly for the strong shadowing scenario. Calculations based on the color dipole model and gluon saturation effects [67] can describe experimental data in the forward rapidity region for inclusive neutron multiplicities but fail to describe the data at midrapidity.

4.11.2 Coherent $\sigma_{\gamma\mathrm{Pb}\to\mathrm{J/\psi Pb}}$ Results

Based on the measured $\mathrm{d}\sigma_{\mathrm{J/\psi}}/\mathrm{d}y$ of coherent J/ψ in the 0n0n, 0nXn, and XnXn classes, together with the photon flux calculated in STARLIGHT, the cross section of coherent J/ψ photoproduction at a given photon-nucleon center-of-mass energy, $W^{\mathrm{Pb}}_{\gamma\mathrm{N}}$, can be extracted following the method suggested in [22].

At $y \approx 0$, Eq. 4.1 can be rewritten as:

$$\frac{\mathrm{d}\sigma_{\mathrm{J/\psi}}}{\mathrm{d}y} = 2N_{\gamma\mathrm{Pb}}(0) \cdot \sigma_{\gamma\mathrm{Pb}\to\mathrm{J/\psi Pb}}(0). \tag{4.25}$$

On the other hand, based on the expectation that the high-photon energy contribution can be considered negligible at very forward rapidity ($-4.5 < y < -3.5$) [22, 56], Eq. 4.1 can be rewritten as:

$$\frac{\mathrm{d}\sigma_{\mathrm{J/\psi}}}{\mathrm{d}y} = N_{\gamma\mathrm{Pb}}(y) \cdot \sigma_{\gamma\mathrm{Pb}\to\mathrm{J/\psi Pb}}(y). \tag{4.26}$$

Therefore, $\mathrm{d}\sigma_{\mathrm{J/\psi}}/\mathrm{d}y$ at lower $W^{\mathrm{Pb}}_{\gamma\mathrm{N}}$ can be approximated using ALICE and LHCb data.

Fig. 4.22 shows the extracted $\sigma_{\gamma\mathrm{Pb}\to\mathrm{J/\psi Pb}}$ as a function of $W^{\mathrm{Pb}}_{\gamma\mathrm{N}}$, compared to ALICE and LHCb very forward rapidity data [50, 54] and the mid-rapidity data [51].

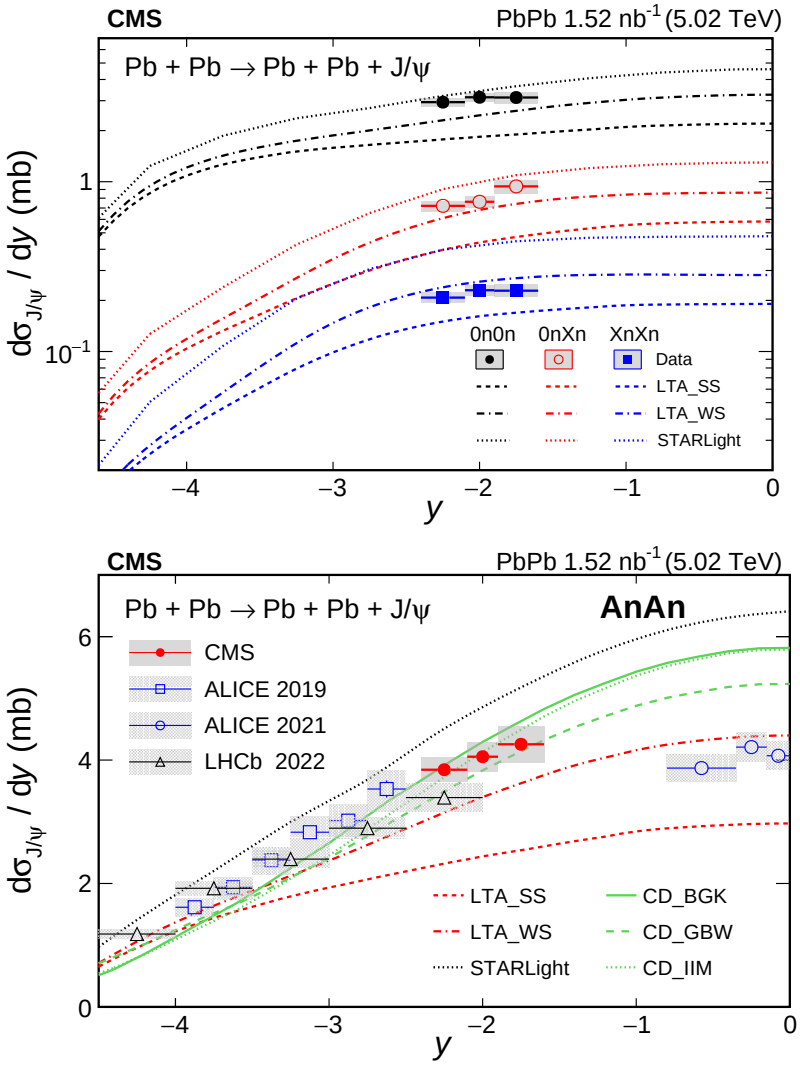

Figure 4.21 : Differential J/ψ cross section as a function of rapidity in different neutron multiplicity classes (top) and in the inclusive neutron multiplicity class (bottom). Vertical bars and shaded boxes around data points represent the statistical and systematic uncertainties, respectively. Theoretical predictions from LTA weak/strong shadowing [56] and the color dipole model [67] are shown as colored curves. All inclusive data are compared to ALICE data [50, 51] and LHCb data [54].

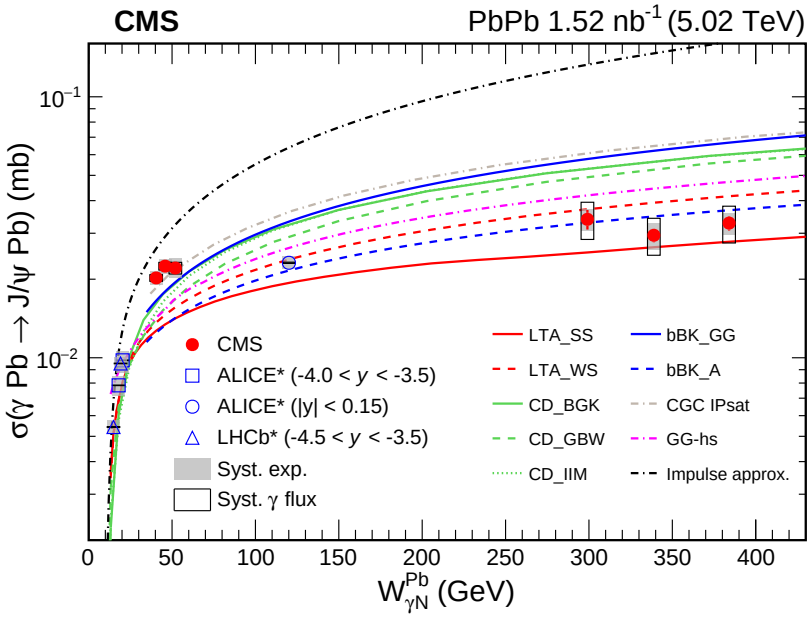

Figure 4.22 : Exclusive photoproduction of J/ψ off Pb as a function of the centre-of-mass energy of the γPb system, $W_{\gamma \mathrm{N}}^{\mathrm{Pb}}$, measured in 5.02 TeV PbPb UPC by the CMS experiment, compared to ALICE and LHCb very forward rapidity data [50, 54] and mid-rapidity data [51]. Theoretical model calculations [22, 68, 69, 56, 70, 67] are shown as colored curves.

At low $W_{\gamma N}^{Pb}$ up to 40 GeV, the extracted $\sigma_{\gamma Pb \to J/\psi Pb}$ shows a rapid rise with increasing $W_{\gamma N}^{Pb}$, consistent with the expectation of a fast increase in gluon density in the nucleus (e.g., from the IA model). However, the most striking feature of the data is a nearly flat plateau with little increase over a wide $W_{\gamma N}^{Pb}$ range from 40 to 400 GeV. This observation could imply the onset of saturation of the Pb nucleus starting at the corresponding Bjorken-x values. However, higher-order perturbative QCD corrections (e.g., quark-antiquark exchange) [71, 72] could complicate the interpretation of the data. Alternatively, the observed trend could also be interpreted as the onset of the black disk limit (BDL) [73, 74, 75, 40]. In this novel regime, the target nucleus becomes completely absorptive to projectile photons because of extremely high gluon density at small Bjorken-x. The photon-nucleus cross section approaches the unitarity limit allowed by the geometrical size of the nucleus. There is still a tendency for a slow rise of the cross section from 40 to 400 GeV toward the BDL, which may suggest that the edge of the nucleus has not become "black" but is gradually approaching the BDL as the energy increases.

Theoretical models based on established QCD approaches, including the leading twist pQCD approach, color dipole models, and color glass condensate models, all fail to predict the observed trend in the data. All these models show a continuously rising trend of the cross section with $W_{\gamma N}^{Pb}$, although they do predict a certain level of suppression of the cross section with respect to the IA baseline. The BDL, as indicated by the data, is a new domain of QCD, where established theoretical techniques are no longer applicable and new methods need to be developed to study the behavior of high-energy interactions near the unitarity limit.

4.11.3 Nuclear Suppression of Gluonic Structure

In the leading twist pQCD framework, the coherent J/ψ photoproduction cross section is proportional to the square of the gluon PDF, as supported by experimental data on exclusive J/ψ photoproduction off protons in ep, pPb, and pp collisions, as summarized in Ref. [47]. This is also known as the scenario of weak absorption and color transparency. The nuclear suppression factor of the gluon PDF, $R_{\mathrm{g}}^{\mathrm{Pb}}$, can be defined as the square root of the ratio of the measured coherent J/ψ production cross section to that from the IA model in the absence of any nuclear effects [26]:

$$R_{\mathrm{g}}^{\mathrm{Pb}} = \sqrt{\frac{\sigma_{\mathrm{J/\psi}}}{\sigma_{\mathrm{J/\psi}}^{\mathrm{IA}}}}. \tag{4.27}$$

The extracted $R_{\mathrm{g}}^{\mathrm{Pb}}$ results are shown in Fig. 4.23 as a function of Bjorken-x.

The nuclear suppression factor in the high-x (low $W_{\gamma\mathrm{N}}^{\mathrm{Pb}}$) region of $x > 5 \times 10^{-3}$ is approximately constant at 0.8–0.9. However, moving toward the very small x region of $x \sim 10^{-5}$–10^{-4}, the suppression factor drops dramatically to $\sim$ 0.4–0.5, indicating stronger suppression of the observed gluon density by high-energy photons in a nucleus than in free nucleons. However, if the BDL of strong absorption is reached for $x < 5 \times 10^{-3}$ or $W_{\gamma\mathrm{N}}^{\mathrm{Pb}} > 40\,\mathrm{GeV}$, the relationship between the measured VM cross section and the single gluon PDF in the weak absorption limit does not hold anymore. The sensitivity to the single gluon PDF is lost in the BDL. As mentioned earlier, new theoretical methods are needed in this new domain of QCD studies to understand the gluonic structure and dynamics at extreme densities.

More recently, the ALICE and STAR collaborations have reported new measurements of coherent J/ψ photoproduction in PbPb and AuAu collisions [76, 77]. Fig. 4.24 shows the updated comparison with ALICE and STAR data. Together with the new data, the CMS results are consistent with all other measurements, confirming

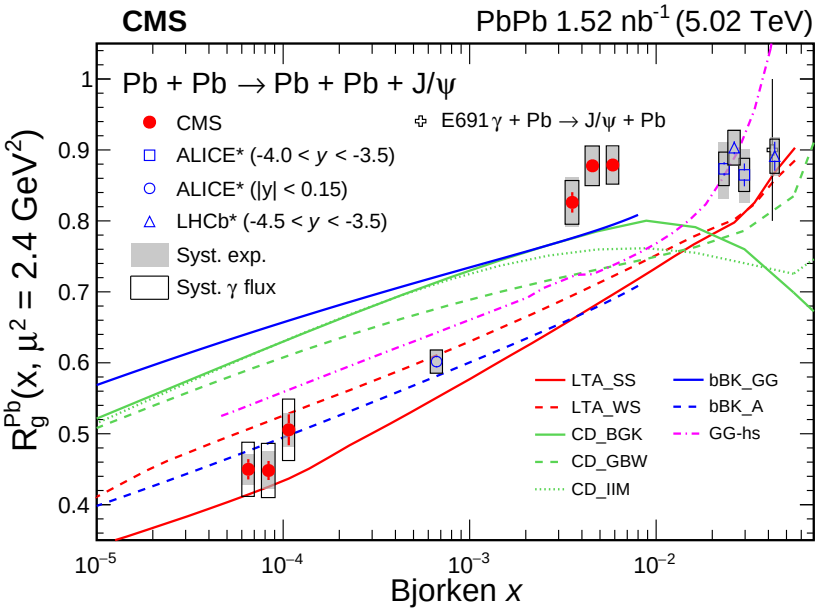

Figure 4.23 : The nuclear suppression factor of coherent J/ψ photoproduction: ratio of the production cross section in photon-nuclear interaction over the IA model [26]. Vertical bars and shaded boxes around data points represent the statistical and systematic uncertainties, respectively. Theoretical model calculations are shown as colored curves.

the surprising trend of $\sigma_{\gamma\mathrm{Pb}\to\mathrm{J}/\psi\mathrm{Pb}}$ with increasing $W_{\gamma\mathrm{N}}^{\mathrm{Pb}}$.

4.11.4 Data Driven Prediction

So far in our analysis, we have focused on obtaining $\sigma_{\gamma\mathrm{Pb}\to\mathrm{J}/\psi\mathrm{Pb}}$ from the measured $\mathrm{d}\sigma_{\mathrm{J}/\psi}/\mathrm{d}y$. As we have already seen, the coherent J/ψ cross section as a function of $W_{\gamma\mathrm{N}}^{\mathrm{Pb}}$ shows no tension between ALICE/CMS forward rapidity data and ALICE mid-rapidity data. A natural question arises: what would it look like if we did the reverse–obtaining a data-driven prediction of $\mathrm{d}\sigma_{\mathrm{J}/\psi}/\mathrm{d}y$ from the fitted $\sigma_{\gamma\mathrm{Pb}\to\mathrm{J}/\psi\mathrm{Pb}}$ using the ALICE and CMS data distribution versus $W_{\gamma\mathrm{N}}^{\mathrm{Pb}}$ and the associated photon flux values? Please note that this test was performed not for physics figures but only as an internal check.

For this simple test, we used a Gompertz curve to fit $\sigma_{\gamma\mathrm{Pb}\to\mathrm{J}/\psi\mathrm{Pb}}$ versus $W_{\gamma\mathrm{N}}^{\mathrm{Pb}}$. The Gompertz function is a type of sigmoid function that describes growth as being slowest at the start and end of a given period. It is defined as follows in Eq. 4.28:

$$f(x) = a + (b - a) \cdot \exp(-\exp(c(x - d))). \tag{4.28}$$

The use of Eq. 4.28 is arbitrary; we chose it because it fits the data points very well, although it is not perfect for capturing the slowly increasing trend at high $W_{\gamma\mathrm{N}}^{\mathrm{Pb}}$.

The result of the fit is shown in Fig. 4.25 (left), and the corresponding data-driven prediction using Eq. 4.1 with the fitted Eq. 4.28 and flux is shown in Fig. 4.25 (right). As can be seen, the data-driven prediction curve reproduces the distribution of $\mathrm{d}\sigma_{\mathrm{J}/\psi}/\mathrm{d}y$ vs. y well for the entire applicable rapidity range.

4.11.5 Coherent $\mathrm{d}\sigma_{\psi(2\mathrm{S})}/\mathrm{d}y$ in Different Neutron Classes

As in Sec. 4.11.1, the first measurements of the coherent ψ(2S) production cross section as a function of rapidity in different neutron multiplicity classes are shown

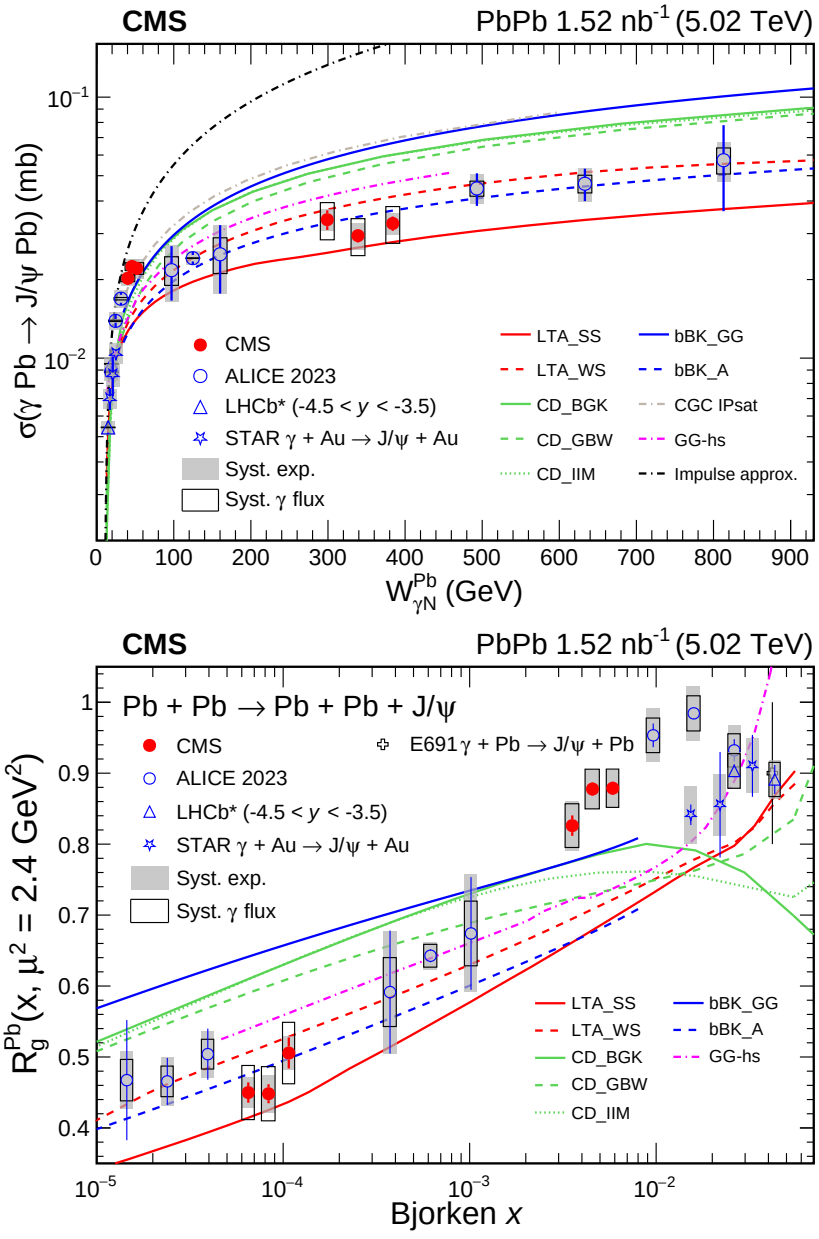

Figure 4.24 : Updated comparison of $\sigma_{\gamma \mathrm{Pb} \to \mathrm{J}/\psi \mathrm{Pb}}$ as a function of $W_{\gamma \mathrm{N}}^{\mathrm{Pb}}$ (top) and $R_{\mathrm{g}}^{\mathrm{Pb}}$ as a function of Bjorken-x (bottom) with the latest ALICE and STAR data [76, 77].

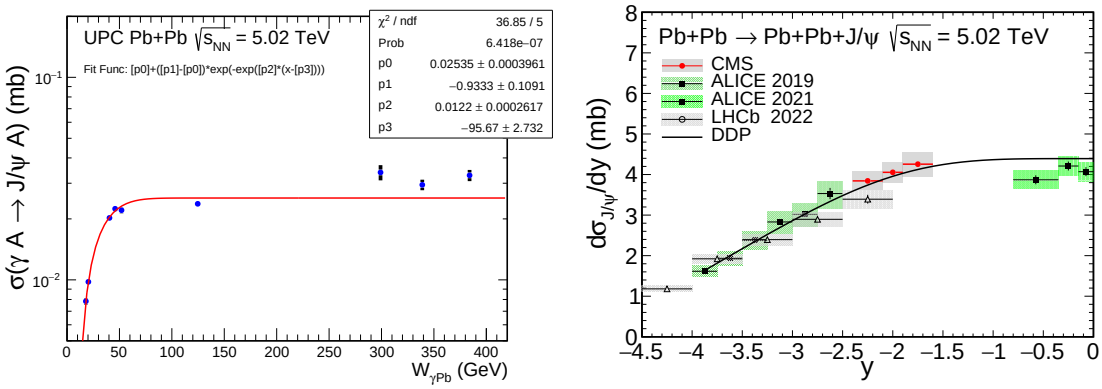

Figure 4.25 : The fitted $\sigma_{\gamma \mathrm{Pb} \to \mathrm{J}/\psi \mathrm{Pb}}$ using Eq. 4.28 with both CMS and ALICE data points is shown on the left. The red curve shows the fit. The data-driven prediction of $\mathrm{d}\sigma_{\mathrm{J}/\psi}/\mathrm{d}y$ from the fitted $\sigma_{\gamma \mathrm{Pb} \to \mathrm{J}/\psi \mathrm{Pb}}$ is shown on the right, with the black curve representing the prediction.

in Fig. 4.26. The CMS data are compared to various theoretical model calculations and to experimental data from ALICE [50, 51] and LHCb [53] for inclusive neutron multiplicities. For the AnAn case, the CMS data follow the trend observed in the ALICE and LHCb forward rapidity data, while also covering a previously unexplored rapidity region.

4.11.6 $(\mathrm{d}\sigma_{\psi(2S)}/\mathrm{d}y)/(\mathrm{d}\sigma_{\mathrm{J}/\psi}/\mathrm{d}y)$ Ratio

The differential cross section ratio was calculated. Many uncertainties cancel, making it a useful quantity to compute. A precise measurement will help constrain theoretical predictions (e.g., VM wavefunctions). Fig. 4.27 shows the differential cross section ratio as a function of rapidity.

4.11.7 Coherent $\sigma_{\gamma \mathrm{Pb} \to \psi(2S) \mathrm{Pb}}$ Results

As in Sec. 4.11.2, the first measurement of the coherent $\psi(2\mathrm{S})$ photoproduction cross section at a given $W_{\gamma \mathrm{N}}^{\mathrm{Pb}}$ can be extracted from the measured $\mathrm{d}\sigma_{\psi(2\mathrm{S})}/\mathrm{d}y$ in the 0n0n,

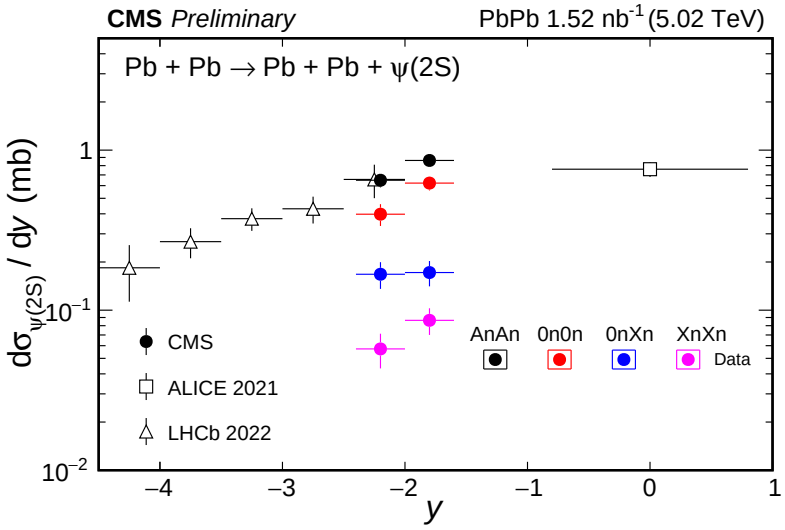

Figure 4.26 : Rapidity differential coherent $\psi(2S)$ production cross section as a function of rapidity in different neutron multiplicity classes: 0n0n, 0nXn, XnXn, and AnAn.

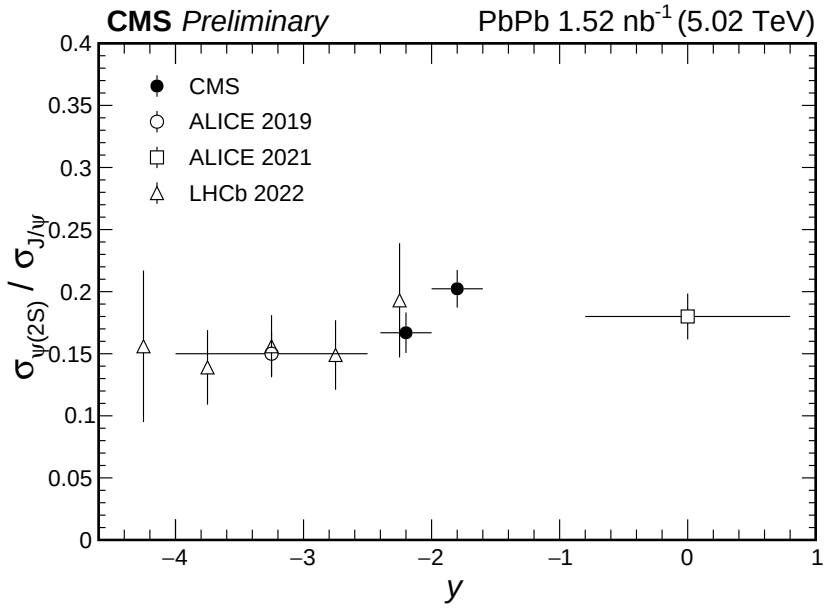

Figure 4.27 : Differential cross section ratio as a function of y.

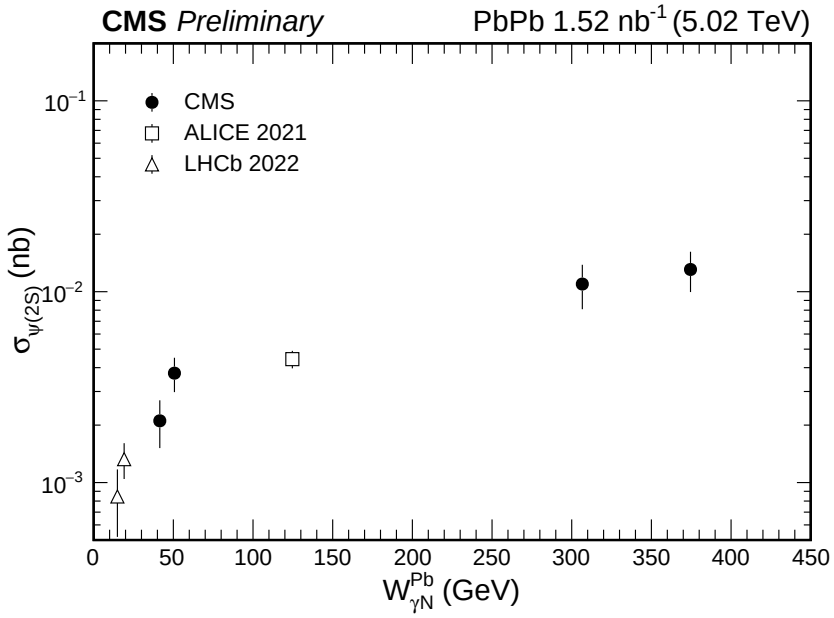

Figure 4.28 : Exclusive photoproduction of $\psi(2S)$ off Pb as a function of $W_{\gamma N}^{Pb}$, measured in 5.02 TeV PbPb UPCs by the CMS experiment, compared to ALICE and LHCb very forward rapidity data [50, 54] and mid-rapidity data [51].

0nXn, and XnXn classes, together with the photon flux calculated using STARLIGHT.

Based on the calculation from Eq. 4.25 and Eq. 4.26, $d\sigma_{\psi(2S)}/dy$ at lower $W_{\gamma N}^{Pb}$ can be approximated using ALICE and LHCb data, and is shown together with the CMS data.

Chapter 5

Coherent $\phi(1020)$ Meson Photoproduction

5.1 Approaching the Non-Perturbative Regime

As shown in Eq. 2.19, the cross section for coherent vector meson (VM) production scales as $\sigma_{\mathrm{VM}} \propto (xG(x, Q^2))^2$. The VM mass ($m_{\mathrm{VM}}$) is a key determinant of the energy scale in QCD calculations. The onset of gluon saturation and the applicability of perturbative QCD (pQCD) are highly sensitive to this scale, motivating the studies in Ch. 4. However, observed trends in coherent J/ψ meson photoproduction reveal discrepancies with all available models, including those incorporating gluon and nuclear shadowing. These inconsistencies highlight gaps in our understanding of the underlying processes and motivate further exploration of nuclear gluonic structure from a new perspective.

The J/ψ meson, with its heavy mass providing a hard scale of a few GeV^2, has been widely used to probe nuclear gluonic structure within the pQCD regime. A natural extension of this study is to investigate lighter VMs. The ϕ meson, consisting of a strange quark-antiquark pair and a mass of 1.019 GeV, uniquely resides at the transition between pQCD and non-pQCD regimes. Fig. 5.1 shows the Feynman diagram for coherent ϕ photoproduction in PbPb UPCs.

Theoretical calculations for exclusive photoproduction cross sections are typically modeled using the color dipole formalism, constrained by dipole parametrizations fitted to DIS data from HERA. When studying light mesons, sensitivity to the non-

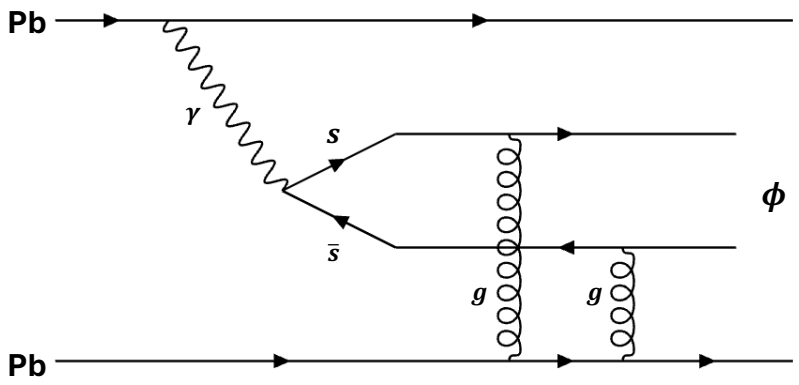

Figure 5.1 : Feynman diagram of coherent ϕ meson photoproduction in UPCs.

perturbative regime increases, making extrapolation from hard processes to the soft regime challenging. Thus, studying exclusive photoproduction of light mesons, such as the ϕ meson, provides unique insights into the non-perturbative regime of strong interactions and advances our understanding of the interplay between gluon saturation and nuclear shadowing.

Interestingly, coherent ϕ mesons had not been observed prior to this analysis. This is primarily because they decay predominantly via $\phi \to \mathrm{K}^+\mathrm{K}^-$ with $\mathcal{B}_{\phi\to\mathrm{K}^+\mathrm{K}^-} = (49.1 \pm 0.5)\%$, and the $\mathrm{K}^+\mathrm{K}^-$ system's mass is very close to the ϕ meson mass. Additionally, coherently produced ϕ mesons have very low transverse momentum ($p_\mathrm{T} \sim 60\,\mathrm{MeV}/c$), meaning their decay products typically have $p_\mathrm{T}^\mathrm{trk} < 0.15\,\mathrm{GeV}/c$. In the CMS detector, kaons leave only a few hits in the pixel detectors, posing significant challenges for experimental detection and explaining the lack of observation in UPCs for decades.

In 2020, as a new PhD student in Professor Wei Li's group, we discussed his vision of detecting ϕ mesons with the CMS detector. The CMS Phase-1 pixel detector upgrade added an additional barrel layer to the innermost pixel detector, resulting in four barrel layers closest to the interaction point. With ϕ-decayed kaons requiring just 4–5 hits for successful reconstruction, detecting coherent ϕ mesons with the CMS detector became feasible. Now, nearly half a decade later, we present the analysis details of the first observation and measurement of coherent ϕ mesons in heavy-ion UPCs. For each rapidity bin, the differential cross section $\mathrm{d}\sigma_\phi/\mathrm{d}y$ was measured for the first time in UPCs.

5.2 Datasets and Monte Carlo Samples

This analysis is based on PbPb UPC data recorded in 2023, corresponding to an integrated luminosity of approximately $1.68\,\mu\mathrm{b}^{-1}$. Good run selection and luminosity determination are based on the official CMS muon physics JSON file.

The dataset is processed using a new CMSSW era modifier designed for low-p_T object reconstruction. Key modifications include:

- Reducing the minimum p_T of tracks to $0.05\,\mathrm{GeV}/c$.
- Reducing the minimum E_T of electrons/photons to $1\,\mathrm{GeV}$.
- Run3_2023_UPC:
  - Reducing the minimum p_T of lowPtGsfElectrons and hiPixelTracks to $0.05\,\mathrm{GeV}/c$.
  - Adjusting pixelPairStepTrackingRegions.originRadius to 0.015.

Table 5.1 : MC samples for coherent/incoherent ϕ photoproduction in UPC PbPb at 5.36 TeV.

Generator	N events	Physics process	Event content
STARLIGHT	26 M	Coherent $\phi \to K^+K^-$	AODSIM
STARLIGHT	26 M	Coherent $\phi \to K^+K^-$ (modified)	AODSIM
STARLIGHT	26 M	Incoherent $\phi \to K^+K^-$	AODSIM

Table 5.2 : Modified nuclear parameters in STARlight MC samples.

Parameter	Value
Woods-Saxon skin depth	0.56
Woods-Saxon nuclear radius	8.67
Inelastic nucleon-nucleon cross section	68.3

- Filtering clusters: number of pixel clusters $< 10{,}000$; number of strip clusters $< 30{,}000$.
- Adding hiPixelTracks, hiCentrality, ZDC digis, and miniAOD χ^2 maps.
- Removing miniAOD selections for electrons, muons, and PF candidates.
- Setting the miniAOD minimum p_{T} for slimmed calo jets to $5\,\mathrm{GeV}/c$.

MC samples are generated using STARLIGHT and processed with CMS GEANT4 for full detector simulation. Details are provided in Tab. 5.1. Modified nuclear parameters for STARLIGHT are listed in Tab. 5.2.

For HF noise thresholds, empty bunch crossing data are used to determine the energy thresholds for HF towers.

5.3 Event Selection

The event selection follows a methodology similar to that in Ch. 4, with modifications to meet the specific requirements of the ϕ analysis.

5.3.1 Online Event Selections

- **Trigger:**
  - HLT_HIUPC_ZeroBias_SinglePixelTrackLowPt_MaxPixelCluster400
- **Requirements:**
  - Pixel clusters are filtered with a maximum size of 400 and a minimum of 1 cluster to avoid empty events.
  - At least one reconstructed pixel track with $p_{\mathrm{T}} > 0.045\,\mathrm{GeV}/c$ is required.
- The trigger is optimized for low-p_{T} tracks, requiring at least one charged particle from UPCs.

5.3.2 Offline Event Selections

To suppress background processes, the following criteria are applied:

- A valid primary vertex is required using the "pprimaryVertexFilter" with at least two general tracks satisfying $|Dxy| < 2\,\mathrm{cm}$ and $|Dz| < 25\,\mathrm{cm}$.
- Pixel cluster shapes must match expectations for heavy-ion collisions ("pclusterCompatibilityFilter").
- HF tower energy thresholds are set to 9.2 GeV (plus) and 8.6 GeV (minus), based on empty bunch crossing data.

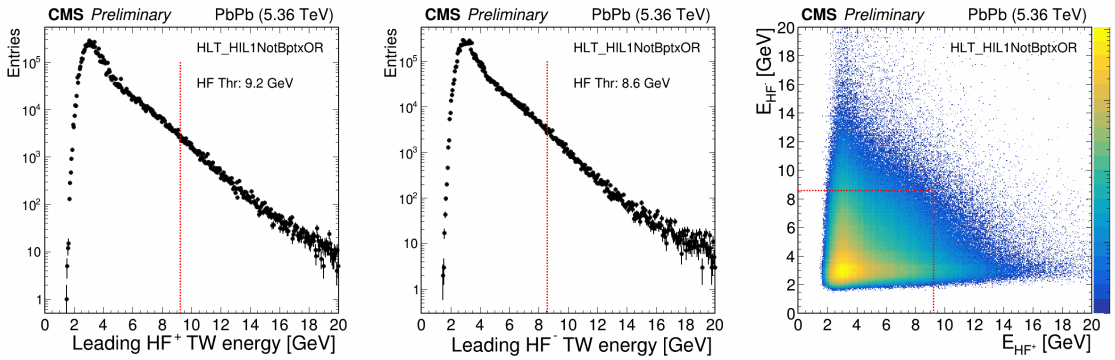

Figure 5.2 : Leading tower energy distributions in HF Plus (left), HF Minus (middle), and 2D distribution (right). Red lines indicate 99% thresholds.

Table 5.3 : Event selection criteria.

Event Selection Criteria
pprimaryVertexFilter & pclusterCompatibilityFilter
$HF^{\text{leading}}_{\text{plus}} \leq 9.2\,\text{GeV}$ & $HF^{\text{leading}}_{\text{minus}} \leq 8.6\,\text{GeV}$
$N^{\text{HP}}_{\text{trk}} == 2$
HLT Trigger

- Events must contain exactly two high-purity tracks and no additional activity.

An example event display is shown in Fig. 5.3.

5.4 Kaon Selection

The K candidates are selected using the "generalTracks" collection, which is the most inclusive set of tracks identified by CMSSW reconstruction. These tracks are reconstructed using both the pixel detector and the strip tracker.

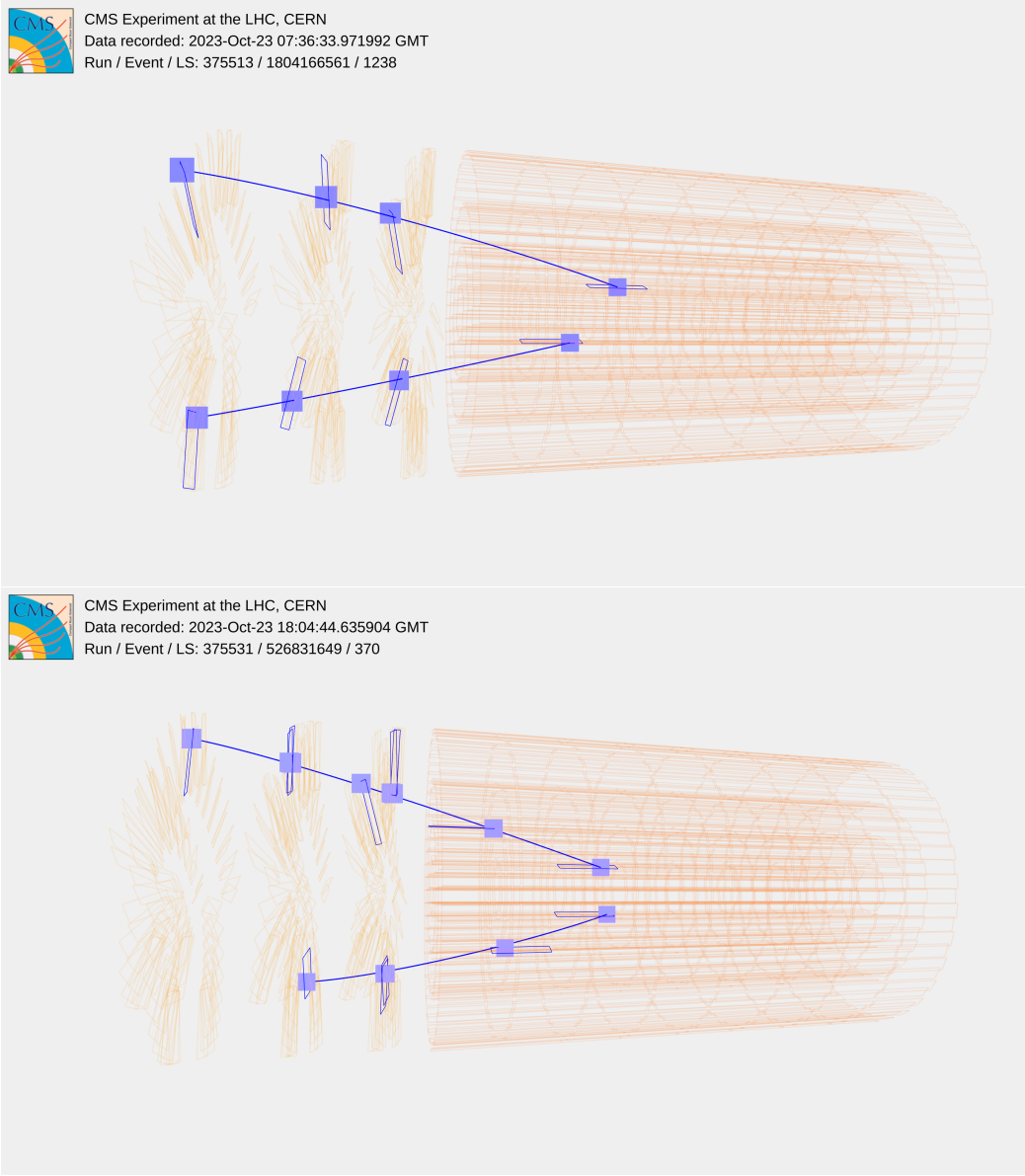

Figure 5.3 : Event display of selected candidates in the CMS detector. High-purity tracks are shown in blue.

5.4.1 Track Selection

Track selection is based on the "generalTracks" collection and requires tracks to pass the "highPurity" quality flag. The official CMS highPurity [78] definition is used, which has slightly lower efficiency but significantly reduces background. Track selection is applied to the two high-purity tracks in each analyzed event. Both tracks must satisfy the impact parameter significance criteria: $|d_{xy}|/\sigma_{d_{xy}} < 3$ and $|d_z|/\sigma_{d_z} < 3$, where d_{xy} and d_z are the distances of closest approach to the primary vertex in the transverse and longitudinal directions, respectively. The corresponding uncertainties are denoted as $\sigma_{d_{xy}}$ and σ_{d_z}.

The track selection criteria are summarized as follows:

- Tracks must be high-purity.
- Tracks must be within the detector acceptance of $|\eta| < 2.4$.
- Tracks must have $p_{\mathrm{T}} > 0.05\,\mathrm{GeV}/c$.
- Tracks must satisfy $|d_{xy}|/\sigma_{d_{xy}} < 3$ and $|d_z|/\sigma_{d_z} < 3$.

5.4.2 Particle Identification

The K candidates are required to pass particle identification (PID) selection. PID is based on the $\mathrm{d}E/\mathrm{d}x$ information in the pixel detector, as described in Ref. [79, 80]. The $\mathrm{d}E/\mathrm{d}x$ represents the energy loss per unit path length of a charged particle and is calculated from the energy deposited in the pixel detector. Due to the long-tailed Landau distribution of energy loss, the mean $\mathrm{d}E/\mathrm{d}x$ is unreliable for particle identification. Instead, the most probable (MP) energy loss is used, as it is less sensitive to fluctuations.

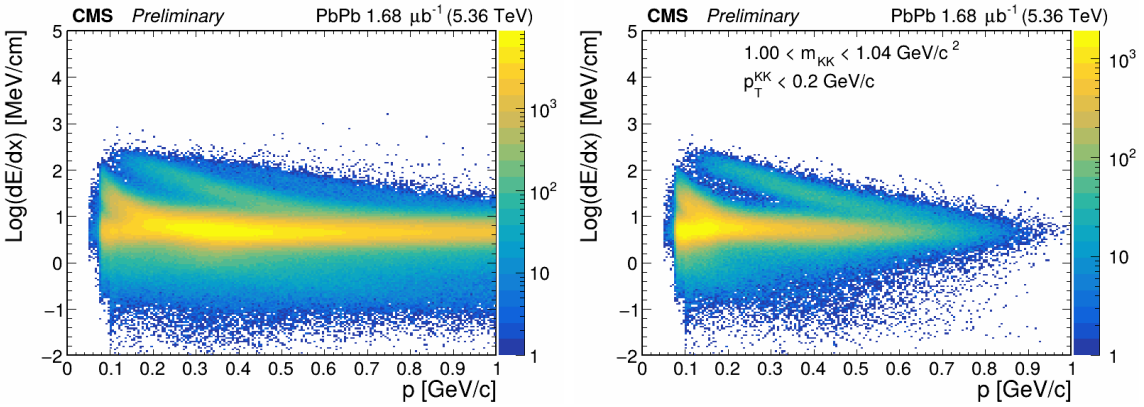

Figure 5.4 : Distribution of $\mathrm{d}E/\mathrm{d}x$ as a function of momentum after event and tracking selections. The left panel shows the raw $\mathrm{d}E/\mathrm{d}x$ distribution. The right panel shows the $\mathrm{d}E/\mathrm{d}x$ distribution with additional kinematic cuts on the di-track ($p_{\mathrm{T}} < 0.20\,\mathrm{GeV}/c$ and $1.00 < m_{\mathrm{K}^+\mathrm{K}^-} < 1.04\,\mathrm{GeV}/c^2$). The K band is clearly visible and well separated from the π and e bands at low momentum.

The Harmonic-2 estimator is employed to calculate the MP $\mathrm{d}E/\mathrm{d}x$. This estimator combines individual $\mathrm{d}E/\mathrm{d}x$ measurements along the particle trajectory into a single value, suppressing anomalously high charges. The Harmonic-2 estimator is defined as:

$$I^{\text{Harm-2}} = \left(\frac{1}{N} \sum_{i=1}^{N} \left(\frac{\Delta E}{\Delta x} \right)_i^k \right)^{1/k}, \quad k = -2. \tag{5.1}$$

Fig. 5.4 shows the $\mathrm{d}E/\mathrm{d}x$ distribution as a function of momentum after event and tracking selections. The right panel includes additional kinematic cuts compared to the left panel. The K band is clearly visible and well separated from the π and e bands at low momentum. At high momentum, the K band overlaps with the π band, making PID more challenging.

The PID selection models the probability density functions (PDFs) of $\mathrm{d}E/\mathrm{d}x$ values as a function of momentum for K and π. The PDFs are modeled as Gaussian

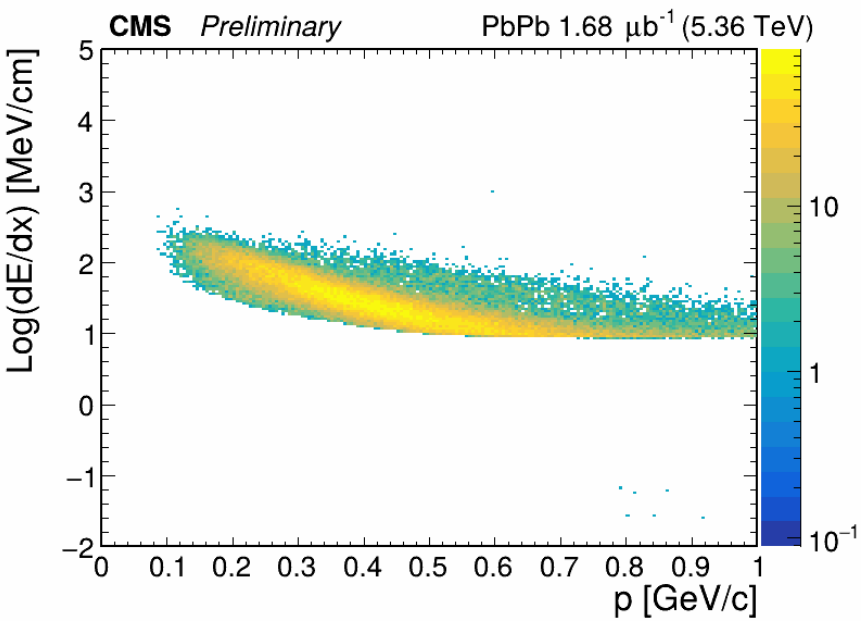

Figure 5.5 : Distribution of $\mathrm{d}E/\mathrm{d}x$ as a function of momentum after event, tracking, and PID selections.

distributions:

$$P_k(\varepsilon|p) = \frac{1}{\sqrt{2\pi}\sigma_k} \exp\left(-\frac{(\varepsilon-\mu_k)^2}{2\sigma_k^2}\right). \tag{5.2}$$

Here, $\varepsilon = \log(\mathrm{d}E/\mathrm{d}x)$, and μ_k and σ_k are the momentum-dependent mean and width of the ε distribution for particle species k. Since the pair production of p and $\overline{\mathrm{p}}$ is strongly suppressed due to the lack of coupling to VM photoproduction in UPC events [17], the selected two-track events mainly contain e, K, and π. To select high-quality $\mathrm{K}^+\mathrm{K}^-$ events, each track must satisfy:

$$P_{\mathrm{K}}(\varepsilon|p) > 10P_{\pi}(\varepsilon|p). \tag{5.3}$$

The PID selection is applied to both positive and negative tracks. The results are shown in Fig. 5.5.

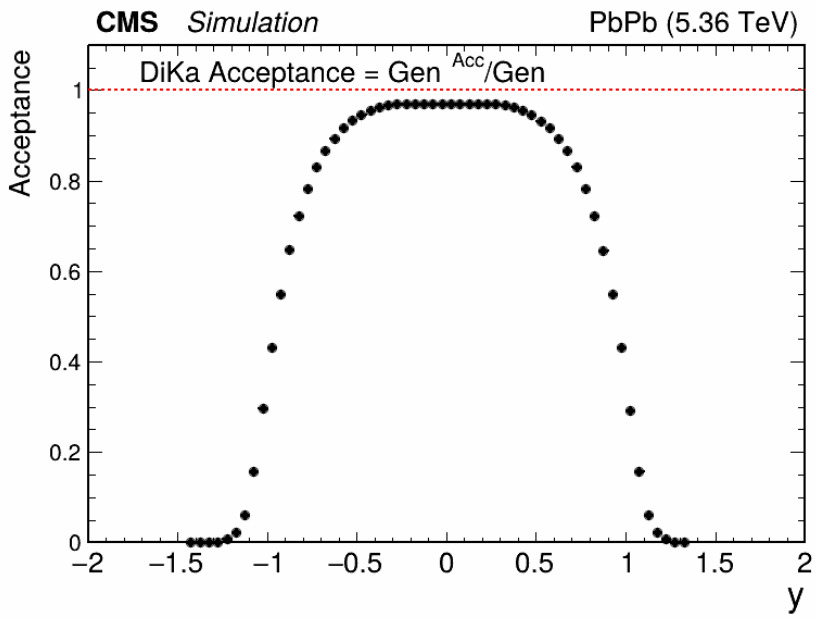

Figure 5.6 : Acceptance correction factors as a function of ϕ rapidity, evaluated from the MC simulation.

5.5 Reconstruction Acceptance and Efficiency Corrections

The data must be corrected for both detector acceptance and reconstruction efficiency. The acceptance and efficiency correction factors are estimated using STARLIGHT + CMS GEANT4 simulation samples processed with the same reconstruction as the data. The acceptance correction factors are calculated from the MC simulation using the formula:

$$Acc(\phi) = \frac{N_{\mathrm{Acc}}(\phi)}{N_{\mathrm{Gen}}(\phi)}. \tag{5.4}$$

Here, $N_{\mathrm{Acc}}(\phi)$ is the number of generated ϕ mesons within the detector's kinematic acceptance, and $N_{\mathrm{Gen}}(\phi)$ is the total number of generated ϕ mesons. The detector's kinematic acceptance is defined as the region where both K are within the pseudorapidity range $|\eta| < 2.4$. The acceptance correction factors are shown in Fig. 5.6.

The final ϕ reconstruction efficiencies are calculated using MC simulations and scaling factors derived from the data-driven tag-and-probe (TnP) method:

$$AccEff(\phi) = \epsilon_{\mathrm{MC}}(\phi) \otimes \frac{\epsilon(\mathrm{K}^+)^{\mathrm{TnP}}_{\mathrm{Data}} * \epsilon(\mathrm{K}^-)^{\mathrm{TnP}}_{\mathrm{Data}}}{\epsilon(\mathrm{K}^+)^{\mathrm{TnP}}_{\mathrm{MC}} * \epsilon(\mathrm{K}^-)^{\mathrm{TnP}}_{\mathrm{MC}}} \otimes SF^{\mathrm{TnP}}_{\mathrm{HLT}}. \tag{5.5}$$

Here, $\epsilon_{\mathrm{MC}}(\phi)$ represents the acceptance times efficiency factors obtained from the MC simulation, as defined in Eq. 5.6. The terms $\epsilon(\mathrm{K}^+)^{\mathrm{TnP}}_{\mathrm{Data}}$ and $\epsilon(\mathrm{K}^-)^{\mathrm{TnP}}_{\mathrm{Data}}$ are the single K efficiencies from the TnP method in data. Similarly, $\epsilon(\mathrm{K}^+)^{\mathrm{TnP}}_{\mathrm{MC}}$ and $\epsilon(\mathrm{K}^-)^{\mathrm{TnP}}_{\mathrm{MC}}$ are the single K efficiencies from the TnP method in MC. The $SF^{\mathrm{TnP}}_{\mathrm{HLT}}$ is the scale factor from the TnP method to correct for trigger efficiency. The $\otimes$ symbol indicates that the data-to-MC ratios of single K efficiencies, as functions of η and p_{T}, are applied as scale factors to reweight the reconstructed ϕ mesons in the MC.

$$\epsilon_{\mathrm{MC}}(\phi) = \frac{N^{\mathrm{Evt,Trk,PID}}_{\mathrm{Acc}}}{N_{\mathrm{Gen}}}. \tag{5.6}$$

The MC reconstruction efficiency $\epsilon_{\mathrm{MC}}(\phi)$ is defined as the ratio of reconstructed signals to generated signals. Reconstructed signal events are those where the trigger fired, both K are within the detector's kinematic acceptance (Eq. 5.4), and all track quality and PID selections are satisfied. These selections are identical to those applied to the data, as summarized in Section 5.3. The denominator is the number of generated dikaons in the STARLIGHT + CMS GEANT4 simulation samples. The combined correction factors, which account for TnP scale factors, are shown in Fig. 5.7. The final correction factors are rebinned to match the rapidity binning of the measured ϕ differential cross section. These factors are shown in Fig. 5.8. The final rapidity window is determined to be $0.3 < |y| < 1.0$, constrained by both reconstruction efficiency and detector acceptance. At $|y| > 1.0$, the efficiency approaches zero due to limited K acceptance.

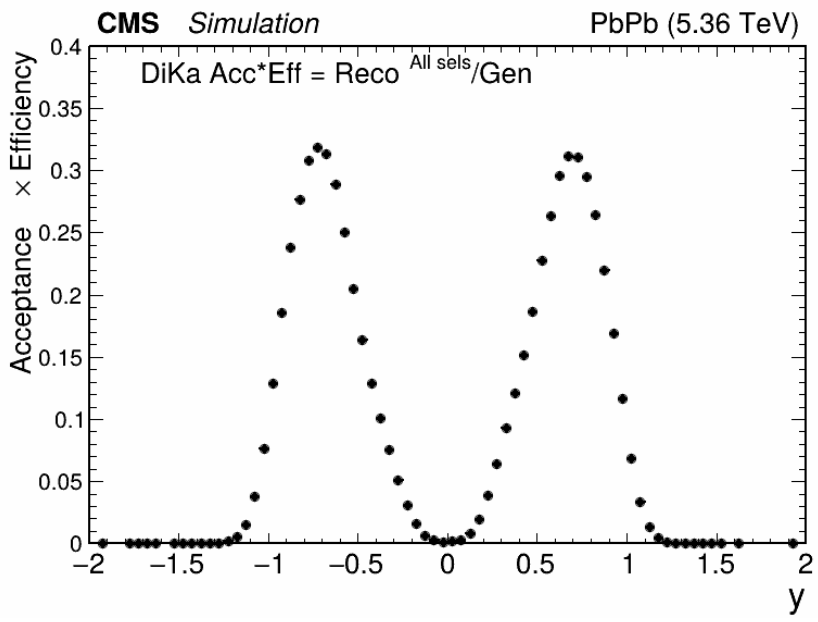

Figure 5.7 : Acceptance times efficiency correction factors as a function of ϕ rapidity, evaluated from the MC simulation with TnP scale factors applied.

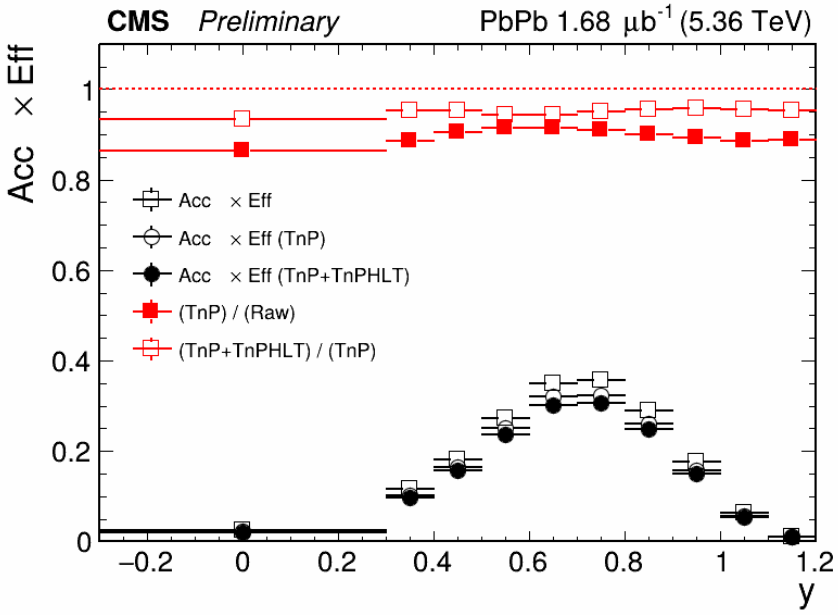

Figure 5.8 : Rebinned acceptance times efficiency correction factors as a function of ϕ rapidity. Comparisons are shown for cases with and without TnP and TnP HLT scale factors. Ratios between each scale factor correction are also displayed.

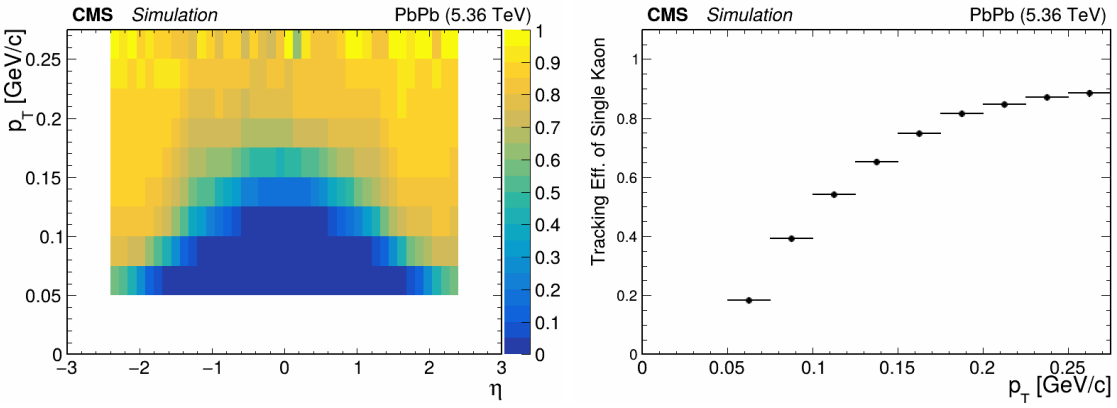

Figure 5.9 : Track reconstruction efficiency for kaons as a function of generated p_{T} and η. The left panel shows the 2D efficiency map, while the right panel shows the 1D efficiency as a function of p_{T}.

5.5.1 Track Reconstruction Efficiency

The track reconstruction efficiency for kaons is evaluated using the STARLIGHT MC sample [25]. It is defined as the ratio of reconstructed generalTracks to generated tracks. For each generated track, the corresponding reconstructed track is identified by matching to the reconstructed generalTracks. Fig. 5.9 shows the track reconstruction efficiency as a function of generated p_{T} and η.

5.5.2 Tag and Probe (TnP) Method

The tag-and-probe (TnP) method is a data-driven technique to measure selection efficiency [59]. It involves selecting a well-identified particle (tag) and measuring the efficiency of a second particle (probe) to pass a selection. The TnP method is applied to measure single K efficiency. K candidates are divided into two categories: tag and probe. The tag must pass tight selection criteria, while the probe must pass loose selection criteria. The efficiency is calculated as the fraction of probes passing the selection criteria divided by the total number of probes.

TnP scale factors are calculated for High-Purity (HP), Track Quality (TrkQual), and PID selections. These scale factors are the ratio of efficiencies in data to those in MC. They are applied to MC to correct the efficiencies of K candidates. Positive and negative K candidates are corrected separately.

For tag selection, K candidates must pass tight criteria defined in Tab. 5.5. Tagged tracks must be within the detector acceptance, have high purity, and meet tracking quality requirements as defined in Sec. 5.4.1. A summary of TnP probe and passing probe definitions is shown in Tab. 5.6. TnP efficiency is calculated as a function of K η and p_{T}. Efficiencies in data and MC are compared to calculate TnP scale factors.

After an event passes the general selection shown in Tab. 5.4, each track is checked for TnP tag selection. If a track passes the tag selection, the other track is checked for probe selection. If the probe passes, the invariant mass of the tag and probe is calculated. The invariant mass is fitted to extract the number of K pairs. Similarly, the invariant mass of the tag and passing probe is fitted to extract the number of K pairs passing the selection. Efficiency is calculated as the ratio of the passing fitted yield to the total fitted yield. For MC, the fitting function is its normalized mass histogram template, equivalent to counting histogram entries. For data, the fitting function is the corresponding mass shape from MC plus a Gaussian background.

The choice of η binning follows previous CMS muon TnP analyses. Since K candidates are mostly produced in the forward detector region with $p_{\mathrm{T}} < 0.20\,\mathrm{GeV}/c$, the efficiency correction focuses on a narrow p_{T} range. To ensure sufficient statistics, wide p_{T} binning is used, as scale factors are relatively flat in this range.

Table 5.4 : Event selection for TnP.

Event Selection for TnP
HLT trigger fired
pprimaryVertexFilter & pclusterCompatibilityFilter
$HF^{\text{leading}}_{\text{plus}} \leq 9.2\,\text{GeV}$ & $HF^{\text{leading}}_{\text{minus}} \leq 8.6\,\text{GeV}$
$N_{\text{trk}} == 2$

Table 5.5 : Selection criteria for K TnP tag.

Selection Criteria for K TnP Tag
Acc
isHP
TrkQual
$\mathrm{d}E/\mathrm{d}x > 4.0\,\text{MeV}/\,\text{cm}$
K Band

Table 5.6 : TnP probe and passing probe definitions.

Efficiency type	Probe	Passing Probe
HP & TrkQual	generalTrack+Acc	+isHP+TrkQual
PID	generalTrack+Acc+isHP+TrkQual	+PassPID

5.5.3 HP and TrkQual TnP

The HP and TrkQual TnP refer to the track selection efficiency, defined as the fraction of pairs passing the high-purity and track quality selection. These TnP selections are applied to the tracking efficiency of the K candidates. An event is selected if the tag passes the tight selection criteria and the probe passes the loose selection of being a general track within the detector acceptance. The probe is considered a passing probe if it is a high-purity track and satisfies the tracking quality selection.

The efficiencies are calculated as the ratio of the passing fitted yield to the total fitted yield. These efficiencies are then compared between data and MC to calculate the TnP scale factors. An example of the TnP HP&TrkQual efficiency as a function of η and p_{T} for the positive K probe is shown in Fig. 5.10.

5.5.4 PID TnP

The PID TnP method is applied to measure the PID efficiency of K candidates. The PID efficiency is defined as the fraction of probes passing the PID selection divided by the total number of probes. An event is selected if the tag passes the tight selection criteria and the probe passes the loose selection of being a general track, is within the detector acceptance, is a high-purity track, and satisfies the tracking quality selection. A probe is considered a passing probe if it satisfies the PID selection.

The efficiencies are calculated as the ratio of the passing fitted yield to the total fitted yield. These efficiencies are then compared between data and MC to calculate the TnP scale factors. An example of the TnP PID efficiency as a function of η and p_{T} for the positive K probe is shown in Fig. 5.11. The PID selection is applied separately to positive and negative tracks.

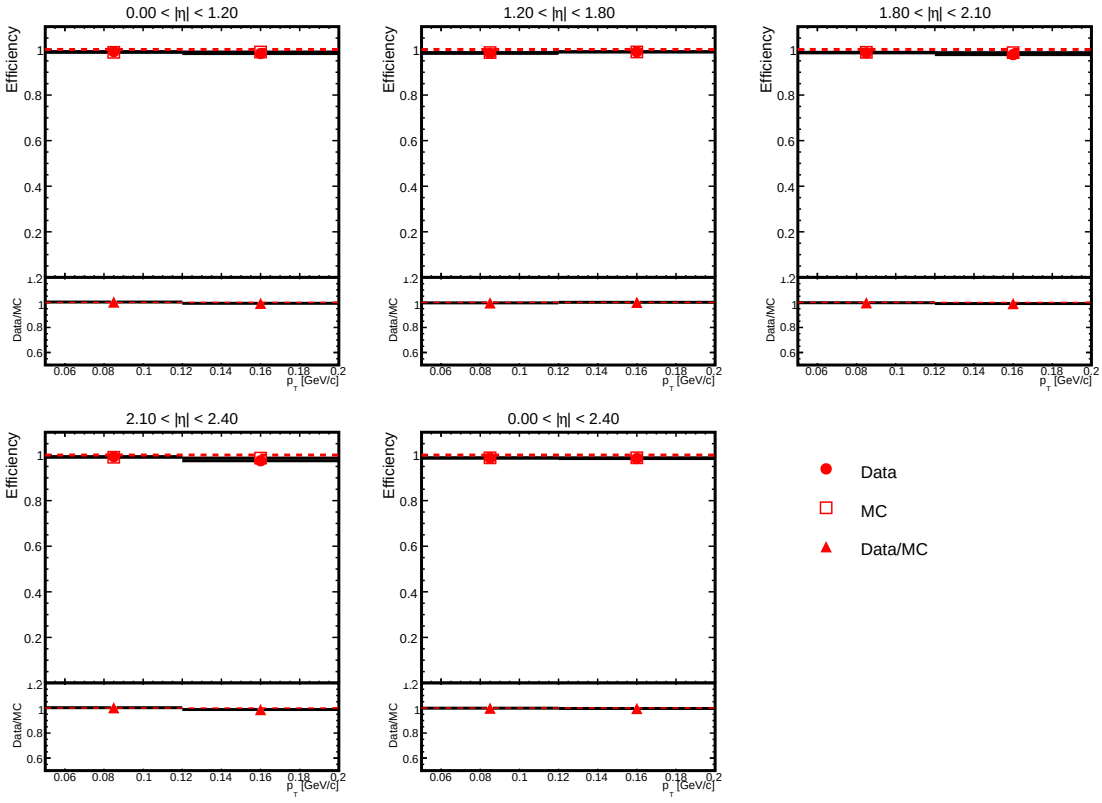

Figure 5.10 : TnP HP&TrkQual efficiency as a function of η and p_{T} for the positive K probe. Efficiencies are calculated from invariant mass fits of the tag and probe pairs. Red solid circles represent efficiencies in data, while red open squares represent efficiencies in MC. The ratio of data to MC efficiencies is shown in the bottom panel.

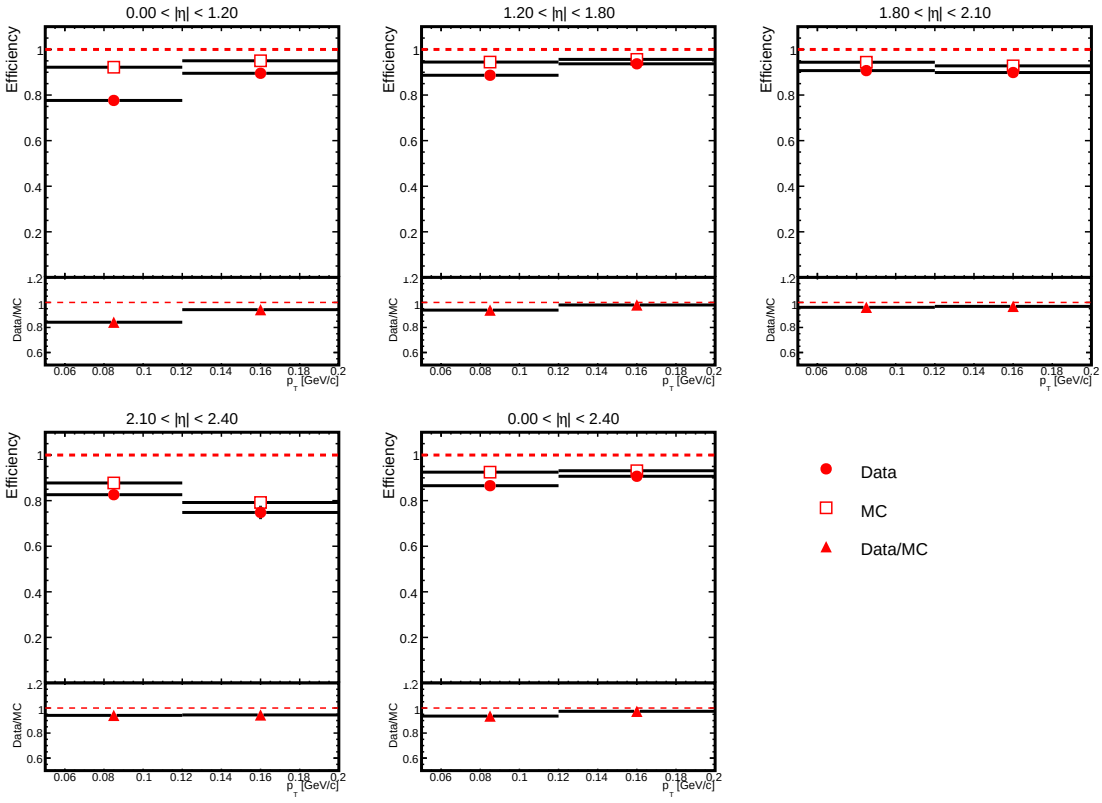

Figure 5.11 : TnP PID efficiency as a function of η and p_{T} for the positive K probe. Efficiencies are calculated from invariant mass fits of the tag and probe pairs. Red solid circles represent efficiencies in data, while red open squares represent efficiencies in MC. The ratio of data to MC efficiencies is shown in the bottom panel.

5.5.5 TnP HLT Scale Factors

For analyses using the pixel track trigger, scale factors (SFs) must be evaluated to correct for trigger efficiency. The TnP HLT method is used for this purpose. This method is similar to the standard TnP approach but requires the tag to match an HLT online trigger object, while the probe is checked for a similar match. The event selection for the TnP HLT is shown in Tab. 5.7. The selection criteria for the K TnP HLT tag are listed in Tab. 5.8. The definitions of the probe and passing probe are provided in Tab. 5.9.

Since the trigger efficiency must be corrected based on the number of offline tracks matched to online trigger objects, the overall event-level SF is evaluated according to the number of such matched tracks. The corresponding SFs are calculated using Eq. 5.7 and Eq. 5.8. Here, $\epsilon^{\text{data}}_{\text{HLT}}$ and $\epsilon^{\text{MC}}_{\text{HLT}}$ are the trigger efficiencies in data and MC, respectively, calculated based on the kinematics of matched generalTracks when only one track is matched to the online trigger object. $\epsilon(1)$ and $\epsilon(2)$ refer to the trigger efficiencies of the first and second tracks, respectively, when both tracks are matched to online trigger objects. The SFs are calculated as the ratio of trigger efficiencies in data to those in MC and are applied to the MC simulation to correct the trigger efficiency.

$$SF_{\text{HLT}} = \frac{\epsilon^{\text{data}}_{\text{HLT}}}{\epsilon^{\text{MC}}_{\text{HLT}}}. \tag{5.7}$$

$$\begin{aligned} \epsilon^{\text{diObj}}_{\text{data}} &= 1 - (1 - \epsilon(1)^{\text{data}}_{\text{HLT}}) \cdot (1 - \epsilon(2)^{\text{data}}_{\text{HLT}}), \\ \epsilon^{\text{diObj}}_{\text{MC}} &= 1 - (1 - \epsilon(1)^{\text{MC}}_{\text{HLT}}) \cdot (1 - \epsilon(2)^{MC}_{HLT}), \\ SF^{\text{diObj}}_{\text{HLT}} &= \frac{\epsilon^{\text{diObj}}_{\text{data}}}{\epsilon^{\text{diObj}}_{\text{MC}}}. \end{aligned} \tag{5.8}$$

Table 5.7 : Event selection for TnP HLT.

Event Selection for TnP HLT
pprimaryVertexFilter & pclusterCompatibilityFilter
$HF_{\text{plus}}^{\text{leading}} \leq 9.2\,\text{GeV}$ & $HF_{\text{minus}}^{\text{leading}} \leq 8.6\,\text{GeV}$
$N_{\text{trk}}^{\text{HP}} == 2$

Table 5.8 : Selection criteria for K TnP HLT tag.

Selection Criteria for K TnP HLT Tag
Acc
isHP
TrkQual
$\text{d}E/\text{d}x > 4.0\,\text{MeV/cm}$
Trigger Matched

Table 5.9 : TnP probe and passing probe definitions.

Efficiency type	Probe	Passing Probe
HLT	generalTrack+Acc+isHP+TrkQual	+Trigger Matched

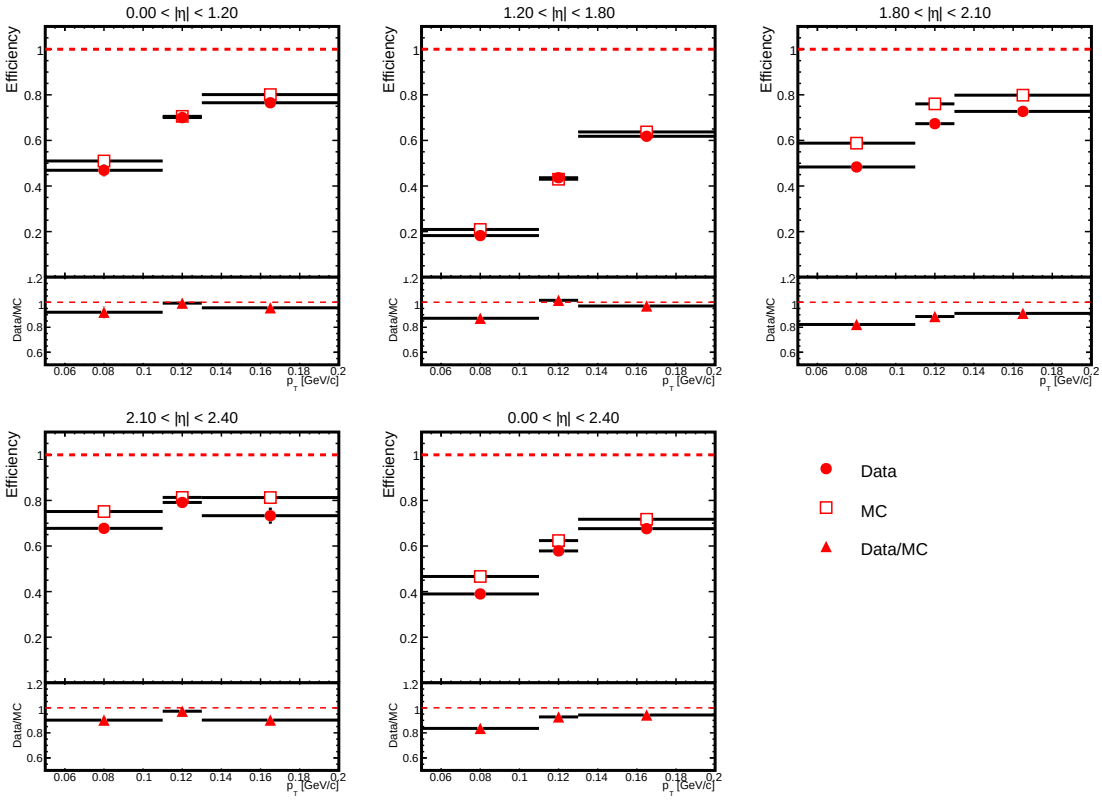

Figure 5.12 : TnP HLT efficiency as a function of η and p_{T}. Efficiencies are calculated from invariant mass fits of the tag and probe pairs. Red solid circles represent efficiencies in data, while red open squares represent efficiencies in MC. The ratio of data to MC efficiencies is shown in the bottom panel.

The TnP HLT fitting is performed similarly to Sec. 5.5.2, and efficiencies are calculated as the ratio of the passing fitted yield to the total fitted yield. Due to the nature of the HLT trigger, efficiencies are calculated based on the kinematics of matched generalTracks, and positive and negative entries are combined during fitting. Additionally, one extra p_{T} bin is added because the HLT trigger efficiency exhibits a stronger p_{T} dependence than the tracking and PID efficiencies. The resulting efficiencies are shown in Fig. 5.12.

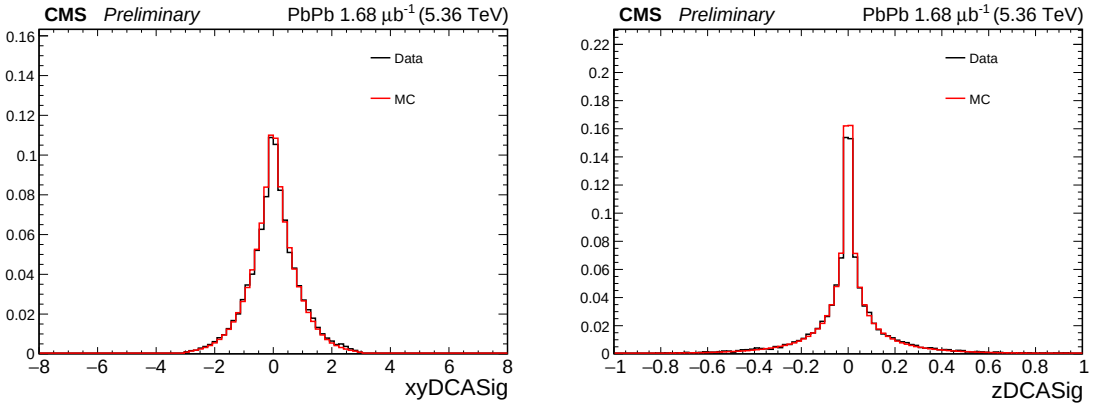

Figure 5.13 : Comparison of the xy (left) and z (right) DCA significance distributions of the selected K candidates after all selection criteria. The MC entries are weighted by the TnP SFs. Both data and MC are normalized.

5.5.6 Comparison of Kinematic Distributions

To evaluate whether the MC models the tracking efficiency correctly, we compare the xy and z DCA significance of the K candidates. Differences in tracking efficiency can affect alignment. After selecting DCA values less than 3 sigma, discrepancies in the kaon distributions between real data and MC would indicate inefficiencies. The comparison of the xy and z DCA significance of the K candidates is shown in Fig. 5.13. The p_{T}, η, and ϕ distributions of the K candidates are shown in Fig. 5.14.

Histogram entries are selected when both tracks pass the tight selection criteria defined in Tab. 5.5, with di-kaon cuts of $1.00 < m_{\mathrm{K^+K^-}} < 1.04\,\mathrm{GeV}/c^2$ and $0.0 < p_{\mathrm{T}} < 0.20\,\mathrm{GeV}/c$. These selections are applied to reduce background and ensure a fair comparison of signal ϕ kaon distributions. Both data and MC are normalized.

5.6 Signal Reconstruction

After selecting pure $\mathrm{K^+K^-}$ candidates, the $\mathrm{K^+K^-}$ pairs are reconstructed to measure the ϕ meson via its $\mathrm{K^+K^-}$ decays. The $\mathrm{K^+K^-}$ pairs are formed within the same

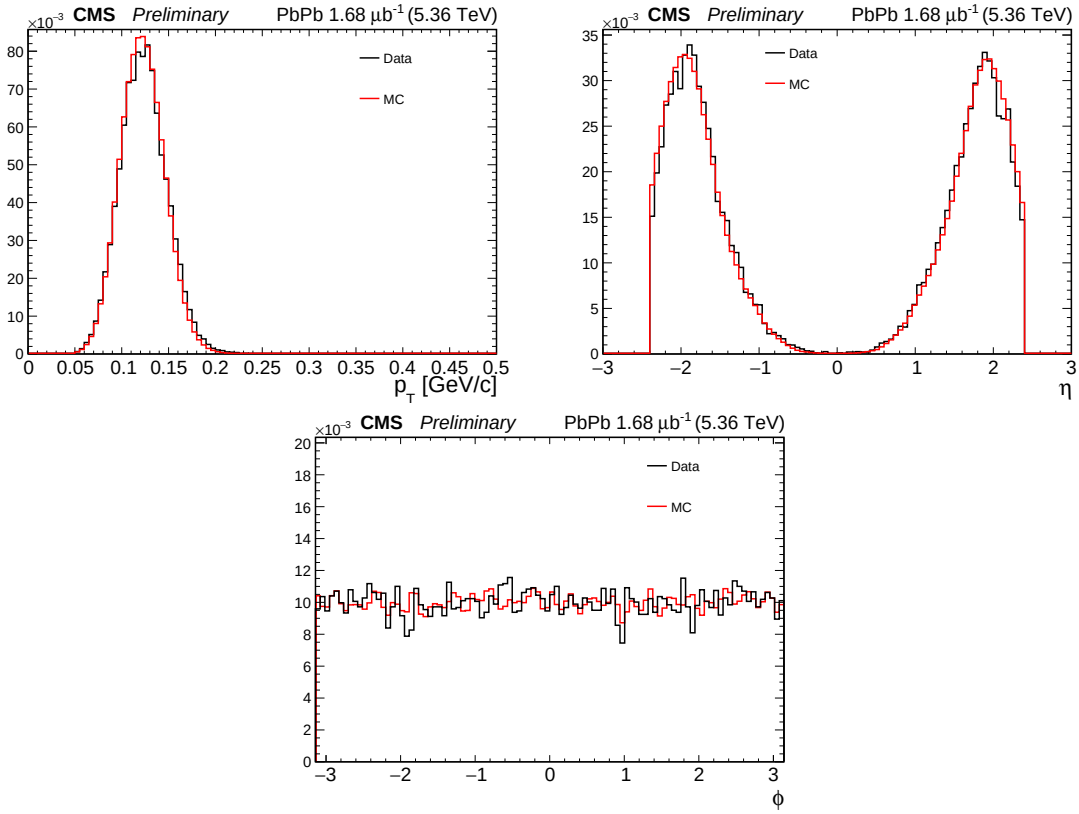

Figure 5.14 : Comparison of the p_{T} (top left), η (top right), and ϕ (bottom) distributions of the selected K candidates after all selection criteria. The MC entries are weighted by the TnP SFs. Both data and MC are normalized.

event, requiring exactly two K candidates. Wrong-sign pairs are negligible since UPC events almost exclusively produce opposite-sign K pairs. The main requirements for the K pair are as follows:

- Both K must be within the detector acceptance of $|\eta| < 2.4$.
- Both K must have a minimum $p_{\mathrm{T}} > 0.05\,\mathrm{GeV}/c$.
- The two K must have opposite charges and be high-purity tracks.
- Both K must satisfy the impact parameter significance criteria: $|d_{xy}|/\sigma_{d_{xy}} < 3$ and $|d_z|/\sigma_{d_z} < 3$.
- Both K must pass the PID selection based on $\mathrm{d}E/\mathrm{d}x$ information in the pixel detector.
- The di-K pair must have an invariant mass within the ϕ mass window of $0.98 < m_{\mathrm{K^+K^-}} < 1.15\,\mathrm{GeV}/c^2$ and a p_{T} within the ϕ p_{T} window of $0.0 < p_{\mathrm{T}} < 0.20\,\mathrm{GeV}/c$.

Fig. 5.15 shows the reconstructed raw invariant mass and p_{T} distributions. Prominent mass peaks are visible, with minimal background. The raw entries in the mass window $[0.98, 1.15]\,\mathrm{GeV}/c^2$, including background, are approximately 20k.

From these raw signals, clear differences between the coherent- and incoherent-dominated regions are observed: (1) In the low-p_{T} region ($< 0.20\,\mathrm{GeV}/c$), dominated by coherent processes, the data show distinct signals. (2) In the higher-p_{T} region ($> 0.20\,\mathrm{GeV}/c$), dominated by incoherent processes, the data exhibit a flat distribution. (3) A small diffractive peak is visible in the low-p_{T} region.

This analysis combines invariant mass and p_{T} distributions of the reconstructed $\mathrm{K^+K^-}$ pairs to disentangle the coherent ϕ contribution from other sources.

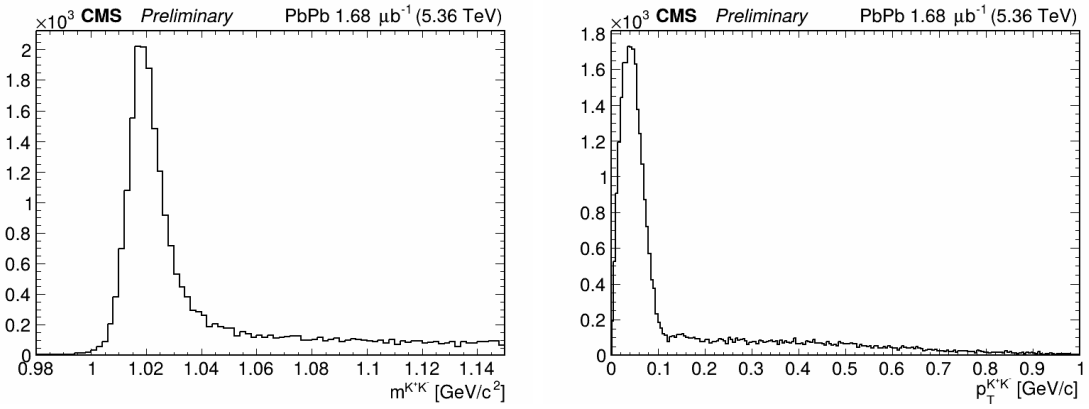

Figure 5.15 : The (left) raw invariant mass and (right) p_{T} distributions of the reconstructed $\mathrm{K}^{+}\mathrm{K}^{-}$ pairs after all selection criteria. The distributions represent the total raw count over all phase space.

5.6.1 Signal Extraction Strategy

The primary focus is on ϕ signals within the invariant mass window $0.98 < m_{\mathrm{K}^{+}\mathrm{K}^{-}} < 1.15\,\mathrm{GeV}/c^{2}$. Within this mass window, the total signal includes several known physics sources:

- Direct coherent $\phi \to \mathrm{K}^{+}\mathrm{K}^{-}$.
- Direct incoherent $\phi \to \mathrm{K}^{+}\mathrm{K}^{-}$ with or without nucleon dissociation.
- Misidentified π combinations.
- $\mathrm{K}^{+}\mathrm{K}^{-}$ continuum from direct non-resonant $\mathrm{K}^{+}\mathrm{K}^{-}$ production in photonuclear collisions.

The direct incoherent $\phi \to \mathrm{K}^{+}\mathrm{K}^{-}$ contamination is corrected using p_{T} fitting, as discussed in Sec. 5.6.2. Misidentified π combinations are minimal and can be neglected; see Sec. 5.6.3. The $\mathrm{K}^{+}\mathrm{K}^{-}$ continuum arises from direct non-resonant $\mathrm{K}^{+}\mathrm{K}^{-}$ production in photonuclear collisions, as discussed in [81]. Although the $\gamma\gamma$

interaction is possible, the production of $\gamma\gamma \rightarrow \mathrm{K}^{+}\mathrm{K}^{-}$ is expected to be minimal compared to the dominant non-resonant $\mathrm{K}^{+}\mathrm{K}^{-}$ production. This dominance arises due to the following reasons:

- The hadronic structure of the photon is dominated by VMs, as described by the vector dominance model.
- The $\mathrm{K}^{+}\mathrm{K}^{-}$ system has a strong coupling to the ϕ VM.
- Non-resonant $\mathrm{K}^{+}\mathrm{K}^{-}$ production is a strong interaction, whereas $\gamma\gamma \rightarrow \mathrm{K}^{+}\mathrm{K}^{-}$ is a QED process.
- The $\gamma\gamma \rightarrow \mathrm{K}^{+}\mathrm{K}^{-}$ process has not been directly measured, and theoretical calculations are still lacking.

Direct separation of direct $\mathrm{K}^{+}\mathrm{K}^{-}$ and $\phi \rightarrow \mathrm{K}^{+}\mathrm{K}^{-}$ is not practical. The simulation of direct $\mathrm{K}^{+}\mathrm{K}^{-}$ production in AA UPCs is still poorly controlled due to the lack of experimental data. Future measurements of direct $\mathrm{K}^{+}\mathrm{K}^{-}$ pair production in PbPb UPC events are of interest, but these must focus on mass regions far from the ϕ meson peak. For this study, the focus remains on the observation of coherent ϕ meson photoproduction. Related studies from both experimental and theoretical perspectives are rapidly evolving.

In summary, the total background is described by a smoothly falling distribution, modeled as a quadratic function similar to previous studies [82, 83, 84]:

$$f_{\mathrm{bkg}}(m) = A(m - 2m_{\mathrm{K}})^{1/2} + B(m - 2m_{\mathrm{K}})^{3/2}. \tag{5.9}$$

Here, m_{K} is the kaon mass, with $2m_{\mathrm{K}} \approx 1.0\,\mathrm{GeV}/c^2$. The parameters A and B are free and are fitted to the data in the sideband region of the invariant mass spectra (>

$1.05\,\mathrm{GeV}/c^2$). These parameters are then fixed in the signal region. This fit function provides a good description of the background with relatively few free parameters. Signal extraction is performed by fitting the total invariant mass distribution with the sum of the signal and background functions.

Reconstruction efficiencies are obtained using well-established simulation techniques, while decay branching ratios are quoted from the 2024 PDG [6]:

- $\mathcal{B}_{\phi\to \mathrm{K}^+\mathrm{K}^-} = (49.1 \pm 0.5)\%$

From the χ^2 template fit to the $m_{\mathrm{K}^+\mathrm{K}^-}$ distribution of $\mathrm{K}^+\mathrm{K}^-$ pairs within the low-p_T ($< 0.20\,\mathrm{GeV}/c$) region, the raw inclusive yields of $N(\phi)$ are calculated. The final coherent ϕ production cross section is then determined using:

$$\frac{\mathrm{d}\sigma_\phi^{\mathrm{coh}}}{\mathrm{d}y} = \frac{N_\phi^{\mathrm{coh}}}{(1+f_\mathrm{I})\cdot\epsilon_\phi\cdot\mathcal{B}_{\phi\to \mathrm{K}^+\mathrm{K}^-}\cdot\Delta y\cdot\mathcal{L}}. \tag{5.10}$$

See Sec. 5.6.2 for the correction factor f_I.

Figure 5.16 shows the mass fit of signals within $p_\mathrm{T} < 0.20\,\mathrm{GeV}/c$ for each rapidity bin. The total fit function is the sum of the signal and background functions. The signal function is derived from histogram-based templates from the MC simulation. The background function is the quadratic function defined in Eq. 5.9. The pull distributions, shown in the bottom panel of each figure, are centered around zero with a width of two, indicating a good fit to the data.

The reconstructed ϕ peaks in real data are influenced by both intrinsic shape and detector effects. The fitting performance (χ^2/ndf and pull histogram) indicates that the simulated MC template can accurately describe the data distribution across all measured rapidity bins. Since the ϕ signal is measured on top of the $\mathrm{K}^+\mathrm{K}^-$ mass threshold (due to the lowest p_T kaon measurement capability), the left side is positioned on a threshold, resulting in an asymmetric signal shape. This shape does

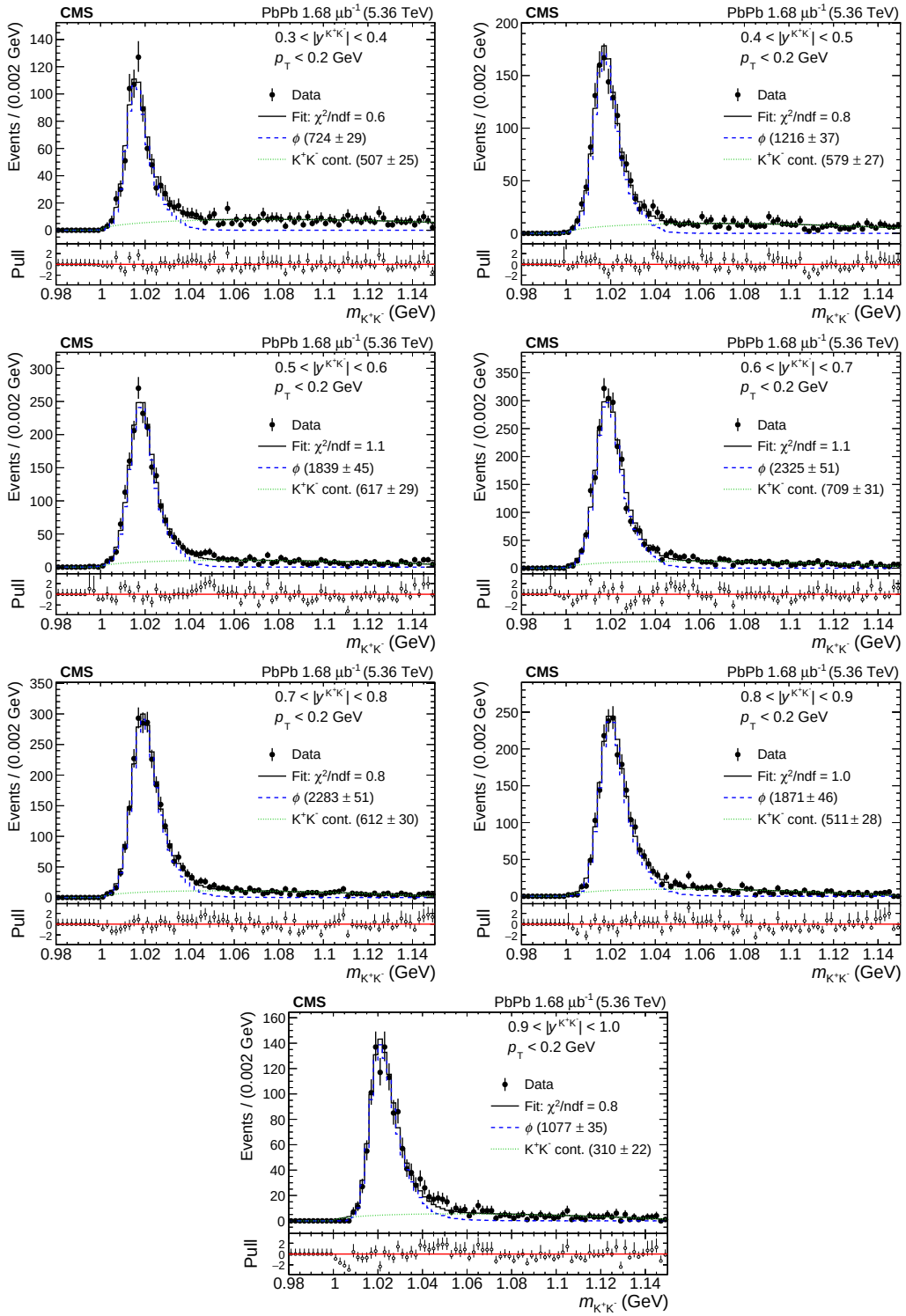

Figure 5.16 : Invariant mass fit of the K^+K^- pairs within $p_T < 0.20\,\mathrm{GeV}/c$ for each rapidity bin.

not conform to a natural Breit-Wigner distribution, making it challenging to fit with typical PDFs. Therefore, the STARLIGHT + CMS GEANT4 simulated template was ultimately chosen for fitting.

Previous ALICE studies [81] showed that in the mass range $1.1 < m_{\mathrm{K^+K^-}} < 1.4\,\mathrm{GeV}/c^2$ above the ϕ mass window, the measured $\mathrm{K^+K^-}$ cross section exceeds expectations from ϕ alone. They argued that interference effects could enhance the yield in the higher mass region ($m > 1.1\,\mathrm{GeV}/c^2$). However, theoretical studies [85, 86] suggest that interference between direct $\mathrm{K^+K^-}$ and $\phi \to \mathrm{K^+K^-}$ in photon-proton interactions is negligible. Direct $\mathrm{K^+K^-}$ (continuum) could dominate the $\mathrm{K^+K^-}$ yield over $\phi \to \mathrm{K^+K^-}$ at higher masses ($m > 1.2\,\mathrm{GeV}/c^2$) in photon-proton interactions.

The ϕ signal yield is extracted within the signal mass window, where $\phi \to \mathrm{K^+K^-}$ signals dominate, as expected from theory and observed in data. While direct $\mathrm{K^+K^-}$ is the main background, potential interference between direct $\mathrm{K^+K^-}$ and $\phi \to \mathrm{K^+K^-}$ is not included in the fitting for two reasons:

- The interference effect is expected to be small within the measured mass window.
- Including interference requires complex corrections to the invariant mass spectra and validation with theoretical PDFs.

This analysis focuses on the production yield of the ϕ meson to provide insights into interacting gluon PDFs inside the nucleus. It contributes experimental data to better understand the recent CMS and ALICE observations of the flattening of coherent J/ψ photoproduction cross sections as a function of photon-nucleon center-of-mass energy.

5.6.2 Incoherent Fraction Extraction

The fit to the coherent mass region within $p_{\mathrm{T}} < 0.20\,\mathrm{GeV}/c$ contains a small fraction of incoherent $\phi \to \mathrm{K}^+\mathrm{K}^-$ signals. To estimate the incoherent ϕ contributions, the distinct p_{T} shapes of different physics processes within the ϕ mass window are utilized. The p_{T} fitting algorithm, established in previous coherent J/ψ measurements (see Ch. 4), uses template fitting. Each source contributes a unique distribution shape to the overall p_{T} distribution, with most templates simulated using STARLIGHT + CMS GEANT4. The p_{T} distribution of reconstructed $\mathrm{K}^+\mathrm{K}^-$ pairs within the ϕ mass window $0.99 < m_{\mathrm{K}^+\mathrm{K}^-} < 1.05\,\mathrm{GeV}/c^2$ is used to extract the incoherent ϕ contribution in the coherent ϕ-dominated region.

After fitting the p_{T} distribution, the total fraction of incoherent ϕ, including contributions with and without nucleon dissociation, is calculated for $p_{\mathrm{T}} < 0.20\,\mathrm{GeV}/c$. This fraction is defined as:

$$f_{\mathrm{I}} = \frac{N_{\phi}^{\mathrm{InCoh}}}{N_{\phi}^{\mathrm{Coh}}}. \tag{5.11}$$

The constraints for the p_{T} fitting parameters are as follows:

- Three free normalization parameters:
  - Number of coherent ϕ mesons, N_{ϕ}^{Coh}.
  - Number of incoherent ϕ mesons without nucleon dissociation, $N_{\phi}^{\mathrm{InCoh}}$.
  - Number of incoherent ϕ mesons with nucleon dissociation, $N_{\phi}^{\mathrm{Disso}}$.
- The $\mathrm{K}^+\mathrm{K}^-$ continuum yield, $N_{\mathrm{K}^+\mathrm{K}^-}$, is determined by fitting the full-p_{T} invariant mass distribution. Its p_{T} distribution is obtained from the sideband near the ϕ mass signal.

The coherent and incoherent ϕ templates without nucleon dissociation are obtained from MC simulations, while the K^+K^- continuum is determined from the full mass sideband fitting. The incoherent ϕ with nucleon dissociation is described by the HERA-measured differential cross sections, $d\sigma/dt$ [87], for proton-dissociative photoproduction. Data for VM $d\sigma/dt$ exhibit an exponential drop with increasing $-t$, with the cross section for the elastic process falling off more steeply than that for the proton-dissociative process. HERA experiments used the fit function:

$$\frac{d\sigma}{dt} = A \cdot e^{-b_{pd}t}. \tag{5.12}$$

To transform $d\sigma/dt$ to $d\sigma/dp_T$, where $t = -p_T^2$, the following transformation is applied:

$$\frac{d\sigma}{dp_T} = \frac{d\sigma}{dt} \cdot \left|\frac{dt}{dp_T}\right| = 2p_T \cdot \frac{d\sigma}{dt}. \tag{5.13}$$

After transformation, the p_T distribution is expressed as:

$$\frac{dN}{dp_T} \sim \frac{d\sigma}{dp_T} \sim p_T \cdot e^{b_{pd} \cdot p_T^2}. \tag{5.14}$$

In ZEUS measurements, the parameter b_{pd} is fitted. In this analysis, b_{pd} is treated as a free parameter, initialized with ZEUS default values, as acceptance, efficiency, and kinematics affect the incoherent p_T shapes with nucleon dissociation.

The STARLIGHT templates are not perfect for describing data in the low-p_T region ($p_T < 0.20\,\text{GeV}/c$) [88, 63, 50, 51, 89, 90]. To improve the p_T fitting performance in the coherent ϕ-dominated region, the coherent ϕ p_T templates are simulated with the Pb radius increased by 2 fm. This accounts for the increased effective diffraction radius of VM photon-nuclear coherent production due to quantum interference effects [63]. Figure 5.17 shows the p_T fit results.

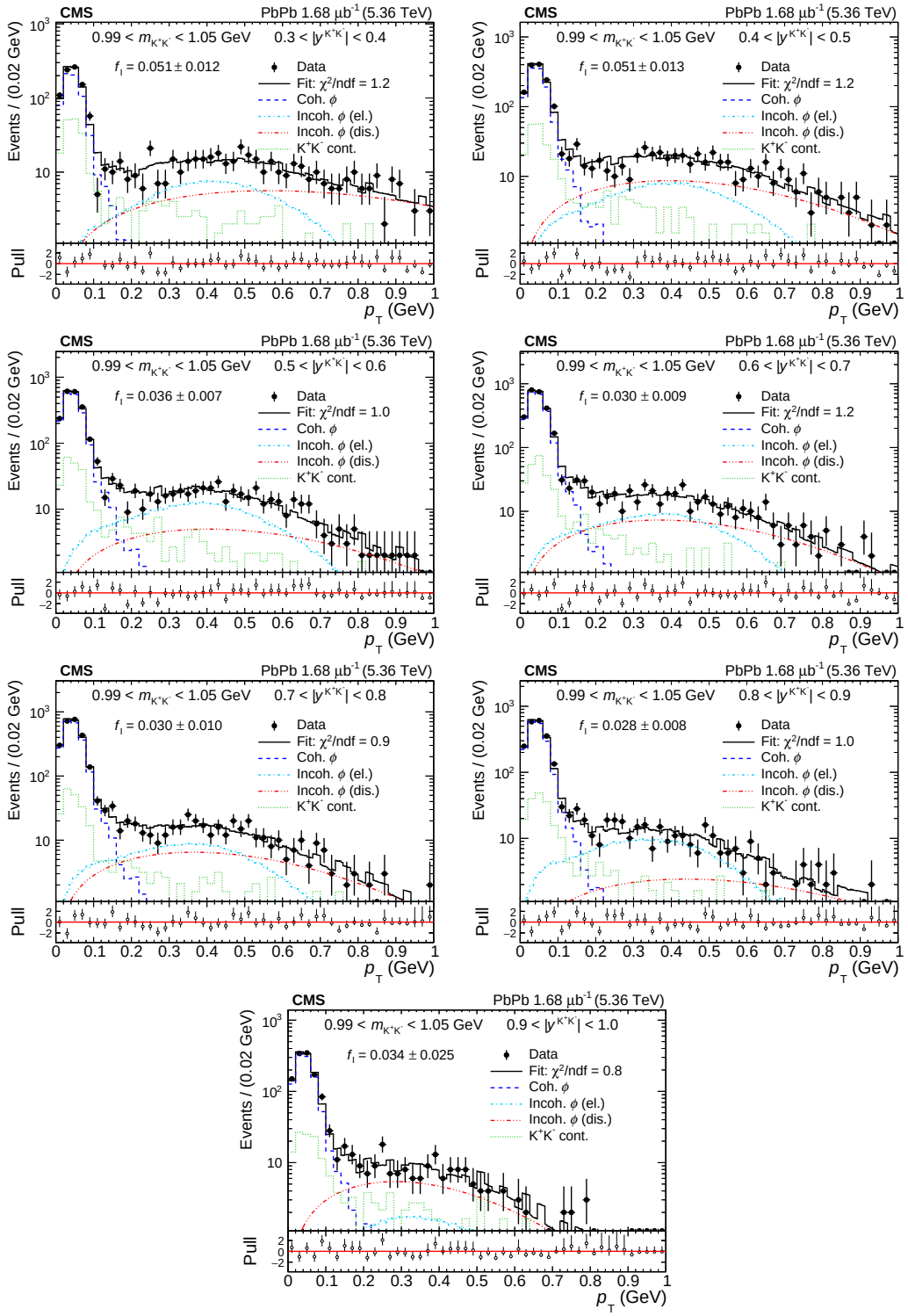

Figure 5.17 : The p_{T} fit results for the signal region $0.99 < m_{\mathrm{K^+K^-}} < 1.05\,\mathrm{GeV}/c^2$.

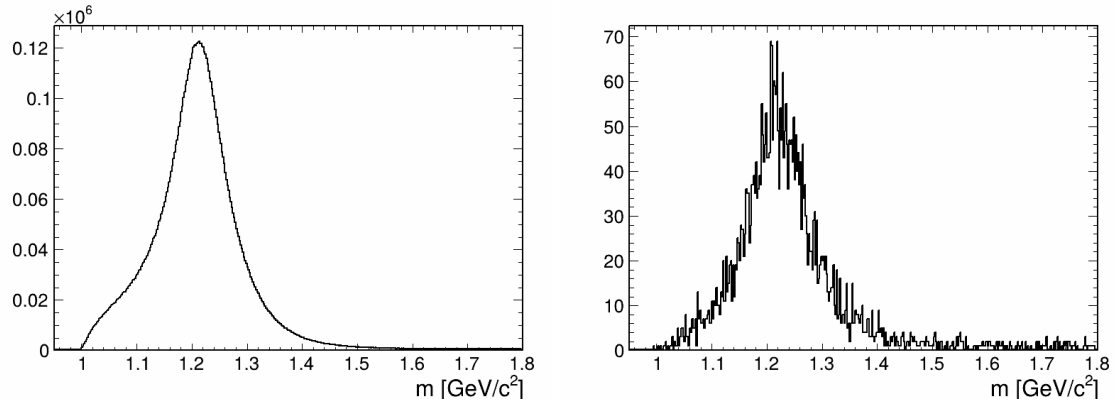

Figure 5.18 : Mass distribution of track pairs with the K mass hypothesis using STARLIGHT coherent UPC $\rho \to \pi^+\pi^-$ and direct π π MC samples. The left panel shows the distribution without PID selection, while the right panel includes PID selection.

5.6.3 Background Contamination

The PID strategy may misidentify pions as kaons, introducing background contamination. Using MC samples, the background contamination is estimated by examining the number of misidentified pion combinations falling within the ϕ mass window. Figure 5.18 shows the mass distribution of track pairs with the K mass hypothesis using STARLIGHT coherent UPC $\rho \to \pi^+\pi^-$ and direct $\pi^+\pi^-$ MC samples. The sample contains 26 million events and is reconstructed with the same low-p_{T} tracking. The left panel shows the mass distribution without PID selection, while the right panel includes PID selection.

Direct $\mathrm{K}^+\mathrm{K}^-$ contamination is also a concern. To compare direct $\mathrm{K}^+\mathrm{K}^-$ and $\pi^+\pi^-$ contamination, the mass distributions of MC $\phi + \mathrm{K}^+\mathrm{K}^-$ and MC $\rho + \pi^+\pi^-$ after PID selection are overlaid. Figure 5.19 shows the mass distributions of track pairs with the K mass hypothesis using STARLIGHT MC samples. The left panel shows the distributions normalized to their respective histogram integrals, while the

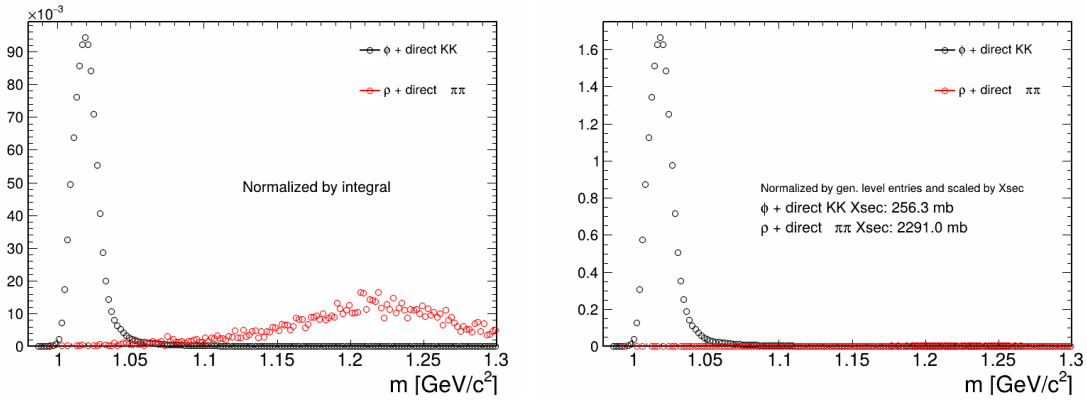

Figure 5.19 : Mass distribution of track pairs with the K mass hypothesis using STARLIGHT MC samples. The left panel shows the $\phi + \mathrm{K}^+\mathrm{K}^-$ and $\rho + \pi^+\pi^-$ distributions normalized to their histogram integrals. The right panel shows the distributions normalized by the number of generated events and scaled by their cross sections.

right panel normalizes them by the number of generated events and scales them by their cross sections. The right panel represents the real relative contributions. The plot suggests negligible pion contamination compared to the $\phi + \mathrm{K}^+\mathrm{K}^-$ peak. Thus, the main background arises from the $\mathrm{K}^+\mathrm{K}^-$ continuum produced directly in photonuclear interactions.

5.7 Systematic Uncertainties

The systematic uncertainties are categorized into several sources, as discussed below. Each uncertainty is evaluated by taking the maximum variation from the nominal result. The total systematic uncertainty is calculated as the quadrature sum of individual contributions.

- **Luminosity:** A 5.0% uncertainty is assigned to the integrated luminosity.
- **Decay Branching Ratio:** The uncertainty in the decay branching ratio of

$\phi \to \mathrm{K}^+\mathrm{K}^-$ is taken from the PDG value [6]: $\mathcal{B}_{\phi\to\mathrm{K}^+\mathrm{K}^-} = (49.1 \pm 0.5)\%$.

- **Efficiency Corrections:** Derived from MC simulations and corrected using TnP scale factors. Systematic uncertainties arise from variations in the fit range and background shape [83].

- **HF Threshold:** The HF energy thresholds are tightened to 8 GeV (from the default 9.2 GeV for HF+ and 8.6 GeV for HF-). The resulting changes in TnP SFs, acceptance, and efficiency corrections are used to estimate the uncertainty.

- **PID:** The PID uncertainty is evaluated by modifying the $\mathrm{d}E/\mathrm{d}x$ selection criteria. A curved band cut is applied, defined as three standard deviations from the mean $\mathrm{d}E/\mathrm{d}x$ value, with an additional lower limit of $\mathrm{d}E/\mathrm{d}x > 2.1$ to suppress pion contamination.

- **Signal Extraction:** Uncertainties in signal extraction are assessed by varying the mass fit range, background shape, and coherent p_T cut.

- **Incoherent Fraction Extraction:** The uncertainty in the incoherent fraction is estimated by varying the coherent p_T template, sideband range, and incoherent p_T template.

The systematic uncertainties are summarized in Fig. 5.20. The total uncertainty is calculated as the quadrature sum of individual contributions.

5.8 First Experimental Measurements of $\mathrm{d}\boldsymbol{\sigma}^{\mathbf{coh}}_{\boldsymbol{\phi}}/\mathrm{d}\boldsymbol{y}$

The first experimental measurements of the coherent ϕ differential cross section as a function of rapidity in heavy-ion UPCs are shown in the upper panel of Fig. 5.21. The

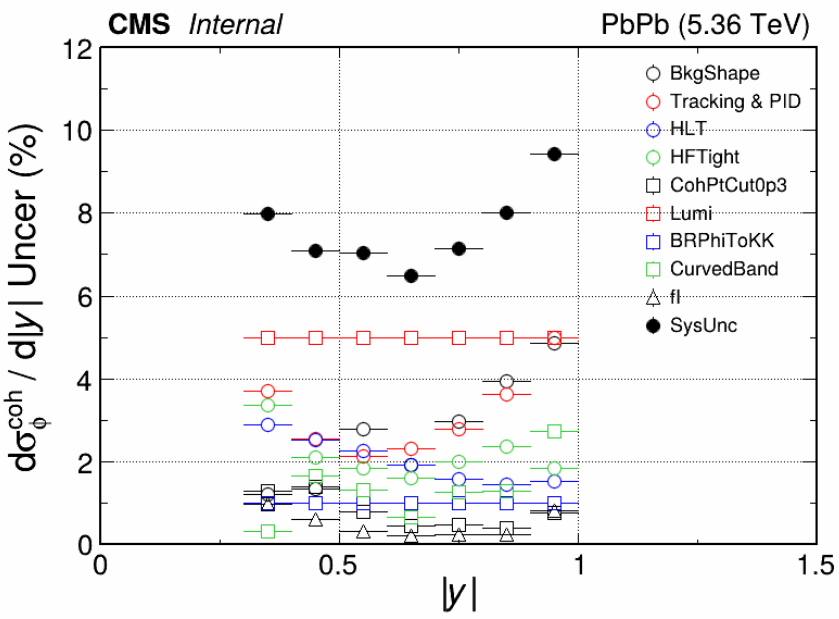

Figure 5.20 : Summary of systematic uncertainties. The left panel shows the overlay of the final results with systematic variations. The right panel shows the percentage contribution of each source to the total uncertainty.

CMS data reveal significant suppression compared to the Impulse Approximation (IA) model, which treats the nucleus as a collection of independent nucleons. To quantify nuclear suppression effects, the ratio of the data to the IA model, defined as S_ϕ, is shown in the lower panel of Fig. 5.21. The extracted S_ϕ values are approximately 0.18–0.20, indicating substantial suppression of coherent ϕ production in heavy-ion collisions compared to the IA model. Notably, the S_ϕ values are about half of the $S_{J/\psi}$ values measured in the midrapidity region in the same kinematic range, as reported by the ALICE experiment [51] with PbPb UPCs at $\sqrt{s_{_{NN}}} = 5.02$ TeV. This difference can be attributed to the smaller mass of the ϕ meson compared to the J/ψ meson, resulting in a larger dipole size and a stronger nuclear shadowing effect.

A summary of theoretical predictions is provided below:

- **Impulse Approximation (IA):** Assumes no nuclear effects, with the coherent

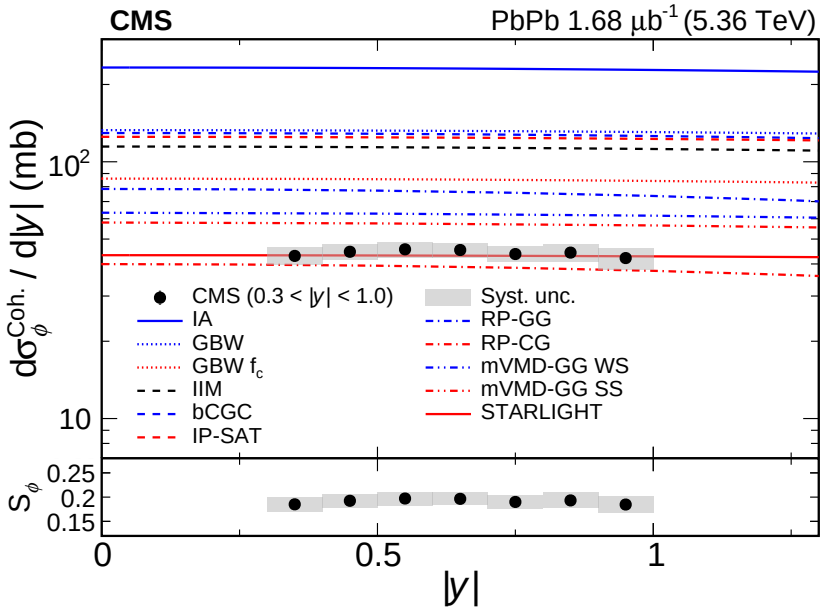

Figure 5.21 : First experimental measurements of the coherent ϕ differential cross section as a function of rapidity (upper panel). The data are compared to various theoretical models [91, 92, 93, 94, 95, 96, 97, 98, 56, 25] (colored curves). The lower panel shows the ratio of the data to the IA model (defined as S_ϕ).

cross section as the sum of contributions from individual nucleons. The ratio of the data to the IA model quantifies nuclear suppression.

- **STARLIGHT:** A Monte Carlo event generator for UPCs, parameterizing coherent photonuclear cross sections using γp data from HERA [25]. Nuclear effects are modeled with the classical Glauber (CG) [99] model, considering elastic dipole-nucleon scattering.

- **Saturation Models:** The color glass condensate (CGC) [10] framework models high-energy scattering in dense media. Coherent ϕ production is described using dipole-proton cross sections fitted to HERA DIS data and extended to nuclei using the Glauber-Gribov (GG) [100] theory.

- **IIM Model:** Interpolates between solutions of the BFKL and BK equations, describing the transition to the saturation regime [91].
- **bCGC Model:** Extends the CGC model by incorporating impact parameter dependence into the saturation scale [92].
- **IP-SAT Model:** Uses an eikonalized dipole-nucleon scattering amplitude and evolves the gluon distribution via the DGLAP equation, improving impact parameter and saturation scale dependence [93, 94].
- **GBW Model:** Incorporates non-perturbative QCD corrections to the photon wavefunction. Predictions with and without these corrections are referred to as GBW and GBW f_c, respectively.
- **Shadowing Models:** Based on the vector meson dominance (VMD) [101] picture, describing photon fluctuations into VMs followed by hadron-nucleon scattering. Multi-scattering effects are modeled using CG or GG models.
- **Modified VMD (mVMD):** Extends the VMD framework by including nuclear medium effects on the VM wavefunction, accounting for strong and weak shadowing [56].
- **Reggeometric Pomeron:** A phenomenological model combining VMD with CG and GG models to describe exclusive diffractive processes [97, 98].

Theoretical predictions incorporating saturation or shadowing effects reproduce the weak rapidity dependence of $\mathrm{d}\sigma_{\phi}^{\mathrm{coh}}/\mathrm{d}y$ but fail to describe the degree of suppression. Saturation models [102], while successful in describing γp data from HERA [82], overpredict $\mathrm{d}\sigma_{\phi}^{\mathrm{coh}}/\mathrm{d}y$ off Pb nuclei by a factor of 2.6–3.0, highlighting the need for

non-perturbative QCD effects. The GBW f_c model [96], which includes non-pQCD corrections to the photon wavefunction, predicts an additional suppression of $d\sigma_{\phi}^{coh}/dy$ by approximately 40% compared to the baseline GBW model but still overestimates the data by a factor of 2.

In contrast, shadowing models predict stronger suppression due to nuclear gluon density effects, suggesting a depletion of the gluon distribution in nuclei at low-x relative to nucleons. This indicates a qualitative difference between the interaction of a small dipole with several nucleons and a similar interaction with a single hadron.

Surprisingly, the STARLIGHT model, based on HERA data and the CG model, describes the data within uncertainties, despite failing to describe recent measurements of coherent ρ and J/ψ photoproduction [51, 103, 53, 88, 76, 77].

In conclusion, the first observation of coherent ϕ meson photoproduction off a heavy nucleus is reported in UPCs at 5.36 TeV. The measured ϕ meson differential cross section as a function of rapidity is presented in the range $0.3 < |y| < 1.0$, probing gluons within the lead nucleus at $x \sim 10^{-4}$. The results provide a unique energy scale between perturbative and non-perturbative QCD regimes. The $d\sigma_{\phi}^{coh}/dy$ is found to be significantly suppressed by a factor of ~ 5 compared to a baseline model treating the nucleus as a collection of free nucleons. This measurement establishes a powerful new tool for exploring nuclear effects and gluonic structure in the small-x regime.

Chapter 6

Conclusions

This thesis presents an analysis of exclusive vector meson photoproduction in ultraperipheral heavy-ion collisions at the LHC using the CMS detector. The main findings and contributions are summarized as follows:

- The first measurement of neutron multiplicity-dependent charmonium photoproduction in ultraperipheral PbPb collisions at $\sqrt{s_{\mathrm{NN}}} = 5.02\,\mathrm{TeV}$ was performed. The differential cross sections of coherent J/ψ and ψ(2S) production as functions of rapidity were measured in the range $1.6 < |y| < 2.4$. The results were compared with theoretical predictions, which were found to be inconsistent with the data, indicating gaps in the current theoretical understanding of coherent charmonium photoproduction.

- The first direct disentanglement of the energy dependence of the coherent J/ψ cross section in ultraperipheral PbPb collisions at $\sqrt{s_{\mathrm{NN}}} = 5.02\,\mathrm{TeV}$ was achieved. An earlier onset and significantly larger suppression of the coherent J/ψ cross section were observed, in clear disagreement with various theoretical models.

- The first observation of coherent ϕ photoproduction in ultraperipheral PbPb collisions at $\sqrt{s_{\mathrm{NN}}} = 5.36\,\mathrm{TeV}$ was reported. The differential cross section of coherent ϕ production as a function of rapidity was measured in the range $0.3 < |y| < 1.0$, revealing substantial suppression of the coherent ϕ cross section.

The data were inconsistent with models incorporating nuclear shadowing or saturation effects, highlighting the importance of nonperturbative QCD effects in the photoproduction process.

In summary, this thesis employs multiple probes of exclusive vector meson production in UPCs to map the gluon distribution in nuclei, study nuclear structure at high energies, and provide new insights into the gluon saturation regime and the small-x nuclear gluonic structure. The wide phase space coverage is achieved by measuring different vector mesons (covering a range of Q^2) and wide rapidity intervals (covering a broad range of Bjorken-x values). These results challenge the current theoretical understanding at extreme densities. A pronounced suppression effect is observed across all measurements, indicating the presence of significant nuclear effects. However, the underlying physics remains unclear. The use of vector meson photoproduction in ultraperipheral heavy-ion collisions as a tool to study nuclear gluonic structure and QCD dynamics in the nuclear medium is shown to be highly promising.

Looking ahead, several exciting projects are planned in UPC studies:

- The full CMS Run-3 dataset will offer significantly higher statistics for ϕ mesons, enabling the first disentanglement of the energy dependence of the coherent ϕ cross section in ultraperipheral PbPb collisions at $\sqrt{s_{\mathrm{NN}}} = 5.36\,\mathrm{TeV}$.

- Future measurements will explore other vector mesons, such as ρ^0, $\psi(2\mathrm{S})$, and Υ, at higher luminosities and energies, utilizing the neutron tagging technique introduced in this thesis.

- Nuclear size scans in UPCs using different ion species, including the upcoming OO collisions at the LHC, will provide further insights into nuclear effects.

- A particularly intriguing prospect is the search for exotic states (e.g. $X(3872)$, $X(6900)$) and double vector meson production (e.g. $J/\psi J/\psi$, $\phi\phi$). LHC experiments have reported numerous exotic resonances in diffractive processes in pp collisions, such as $J/\psi J/\psi$ and $J/\psi\phi$ resonances [104]. The CMS detector's excellent muon reconstruction capabilities are particularly advantageous for reconstructing exotic states decaying into $J/\psi J/\psi$ or $\Upsilon\Upsilon$. For example, CMS has reported multiple exotic resonances in the $J/\psi J/\psi$ mass spectrum in pp collisions [105]. Searching for these exotic-hadron candidates in both pp and heavy-ion data will provide new insights into their internal structure, shedding light on the nature of tetraquark candidates.

By leveraging UPCs as a tool, this thesis has made significant progress in advancing our understanding of nuclear gluonic structure and QCD dynamics in the nuclear medium. These UPC photoproduction studies will be complemented by the future Electron-Ion Collider (EIC) planned at Brookhaven National Laboratory, which will provide a unique opportunity to study both photoproduction ($Q^2 \approx 0$) and electroproduction ($Q^2 > 0$) processes. The EIC will enable a comprehensive investigation of nuclear gluonic structure and the gluon distribution in nuclei across a wide range of length scales.

Bibliography

[1] G. Aad *et al.*, "Observation of a new particle in the search for the Standard Model Higgs boson with the ATLAS detector at the LHC," *Phys. Lett. B*, vol. 716, pp. 1–29, 2012.

[2] S. Chatrchyan *et al.*, "Observation of a New Boson at a Mass of 125 GeV with the CMS Experiment at the LHC," *Phys. Lett. B*, vol. 716, pp. 30–61, 2012.

[3] R. Brandelik *et al.*, "Evidence for Planar Events in e+ e- Annihilation at High-Energies," *Phys. Lett. B*, vol. 86, pp. 243–249, 1979.

[4] Particle Data Group, "Plots of cross sections and related quantities," 2022.

[5] M. E. Peskin and D. V. Schroeder, *An Introduction to quantum field theory*. Addison-Wesley, 1995.

[6] S. Navas *et al.*, "Review of particle physics," *Phys. Rev. D*, vol. 110, no. 3, p. 030001, 2024.

[7] A. Accardi *et al.*, "Electron Ion Collider: The Next QCD Frontier: Understanding the glue that binds us all," *Eur. Phys. J. A*, vol. 52, no. 9, p. 268, 2016.

[8] L. McLerran, "RHIC physics: The Quark gluon plasma and the color glass condensate: Four lectures," 11 2003.

[9] E. Iancu and R. Venugopalan, *The Color glass condensate and high-energy scattering in QCD*, pp. 249–3363. World Scientific, 3 2003.

[10] F. Gelis, E. Iancu, J. Jalilian-Marian, and R. Venugopalan, "The Color Glass Condensate," *Ann. Rev. Nucl. Part. Sci.*, vol. 60, pp. 463–489, 2010.

[11] M. Klein and R. Yoshida, "Collider Physics at HERA," *Prog. Part. Nucl. Phys.*, vol. 61, pp. 343–393, 2008.

[12] P. Newman and M. Wing, "The Hadronic Final State at HERA," *Rev. Mod. Phys.*, vol. 86, no. 3, p. 1037, 2014.

[13] H. Abramowicz *et al.*, "Measurement of the t dependence in exclusive photoproduction of Υ(1S) mesons at HERA," *Phys. Lett. B*, vol. 708, pp. 14–20, 2012.

[14] E. Fermi, "On the Theory of the impact between atoms and electrically charged particles," *Z. Phys.*, vol. 29, pp. 315–327, 1924.

[15] E. J. Williams, "Nature of the high-energy particles of penetrating radiation and status of ionization and radiation formulae," *Phys. Rev.*, vol. 45, pp. 729–730, 1934.

[16] C. F. von Weizsacker, "Radiation emitted in collisions of very fast electrons," *Z. Phys.*, vol. 88, pp. 612–625, 1934.

[17] A. J. Baltz *et al.*, "The Physics of Ultraperipheral Collisions at the LHC," *Phys. Rept.*, vol. 458, pp. 1–171, 2008.

[18] J. Adam *et al.*, "Measurement of e^+e^- Momentum and Angular Distributions from Linearly Polarized Photon Collisions," *Phys. Rev. Lett.*, vol. 127, no. 5,

p. 052302, 2021.

[19] C. A. Bertulani and G. Baur, "Electromagnetic Processes in Relativistic Heavy Ion Collisions," *Phys. Rept.*, vol. 163, p. 299, 1988.

[20] J. D. Jackson, *Classical Electrodynamics*. Wiley, 1998.

[21] S. Klein and P. Steinberg, "Photonuclear and Two-photon Interactions at High-Energy Nuclear Colliders," *Ann. Rev. Nucl. Part. Sci.*, vol. 70, pp. 323–354, 2020.

[22] V. Guzey, M. Strikman, and M. Zhalov, "Disentangling coherent and incoherent quasielastic J/ψ photoproduction on nuclei by neutron tagging in ultraperipheral ion collisions at the LHC," *Eur. Phys. J. C*, vol. 74, no. 7, p. 2942, 2014.

[23] S. Ragoni, "Recent results for forward J/$\boldsymbol{\psi}$ production in Pb-Pb Ultra-Peripheral Collisions at $\sqrt{\mathbf{s_{NN}}} = \mathbf{5.02}$ TeV with the ALICE detector," in *27th International Nuclear Physics Conference*, 9 2019.

[24] S. Klein and J. Nystrand, "Exclusive vector meson production in relativistic heavy ion collisions," *Phys. Rev. C*, vol. 60, p. 014903, 1999.

[25] S. R. Klein, J. Nystrand, J. Seger, Y. Gorbunov, and J. Butterworth, "STARlight: A Monte Carlo simulation program for ultra-peripheral collisions of relativistic ions," *Comput. Phys. Commun.*, vol. 212, pp. 258–268, 2017.

[26] V. Guzey, E. Kryshen, M. Strikman, and M. Zhalov, "Evidence for nuclear gluon shadowing from the ALICE measurements of PbPb ultraperipheral exclusive J/ψ production," *Phys. Lett. B*, vol. 726, pp. 290–295, 2013.

[27] Wikimedia Commons contributors, "LHC.svg," 2024.

[28] S. Dubourg, M. Schaumann, and D. Walsh, eds., *Proceedings of the 2019 Evian Workshop on LHC Beam Operations*, (Geneva, Switzerland), 2019.

[29] CMS Collaboration, "CMS Luminosity Public Results."

[30] V. Chekhovsky *et al.*, "Luminosity measurement for lead-lead collisions at $\sqrt{s_{\mathrm{NN}}}$ = 5.02 TeV in 2015 and 2018 at CMS," 3 2025.

[31] M. Aaboud *et al.*, "Measurement of the Inelastic Proton-Proton Cross Section at $\sqrt{s}$ = 13 TeV with the ATLAS Detector at the LHC," *Phys. Rev. Lett.*, vol. 117, no. 18, p. 182002, 2016.

[32] S. Acharya *et al.*, "ALICE luminosity determination for Pb−Pb collisions at $\sqrt{s_{\mathrm{NN}}} = 5.02$ TeV," *JINST*, vol. 19, no. 02, p. P02039, 2024.

[33] S. Chatrchyan *et al.*, "The CMS Experiment at the CERN LHC," *JINST*, vol. 3, p. S08004, 2008.

[34] CMS Open Data Workshop, "CMS Detector - Images," 2024.

[35] S. Chatrchyan *et al.*, "Description and performance of track and primary-vertex reconstruction with the CMS tracker," *JINST*, vol. 9, no. 10, p. P10009, 2014.

[36] A. M. Sirunyan *et al.*, "Electron and photon reconstruction and identification with the CMS experiment at the CERN LHC," *JINST*, vol. 16, no. 05, p. P05014, 2021.

[37] G. Bayatian *et al.*, "Design, performance and calibration of the CMS forward calorimeter wedges," *Eur. Phys. J. C*, vol. 53, pp. 139–166, 2008.

[38] A. M. Sirunyan *et al.*, "Performance of the CMS muon detector and muon reconstruction with proton-proton collisions at $\sqrt{s} = 13$ TeV," *JINST*, vol. 13, no. 06, p. P06015, 2018.

[39] V. Khachatryan *et al.*, "The CMS trigger system," *JINST*, vol. 12, no. 01, p. P01020, 2017.

[40] L. Frankfurt, M. Strikman, and C. Weiss, "Small-x physics: From HERA to LHC and beyond," *Ann. Rev. Nucl. Part. Sci.*, vol. 55, pp. 403–465, 2005.

[41] S. Chekanov *et al.*, "Exclusive photoproduction of J / psi mesons at HERA," *Eur. Phys. J. C*, vol. 24, pp. 345–360, 2002.

[42] A. Aktas *et al.*, "Elastic J/psi production at HERA," *Eur. Phys. J. C*, vol. 46, pp. 585–603, 2006.

[43] C. Alexa *et al.*, "Elastic and Proton-Dissociative Photoproduction of J/psi Mesons at HERA," *Eur. Phys. J. C*, vol. 73, no. 6, p. 2466, 2013.

[44] R. Aaij *et al.*, "Exclusive J/ψ and $\psi(2S)$ production in pp collisions at $\sqrt{s} = 7$ TeV," *J. Phys. G*, vol. 40, p. 045001, 2013.

[45] B. B. Abelev *et al.*, "Exclusive J/ψ photoproduction off protons in ultra-peripheral p-Pb collisions at $\sqrt{s_{\rm NN}} = 5.02$ TeV," *Phys. Rev. Lett.*, vol. 113, no. 23, p. 232504, 2014.

[46] R. Aaij *et al.*, "Updated measurements of exclusive J/ψ and $\psi(2S)$ production cross-sections in pp collisions at $\sqrt{s} = 7$ TeV," *J. Phys. G*, vol. 41, p. 055002, 2014.

[47] S. Acharya *et al.*, "Energy dependence of exclusive J/ψ photoproduction off protons in ultra-peripheral p–Pb collisions at $\sqrt{s_{\rm NN}} = 5.02$ TeV," *Eur. Phys. J. C*, vol. 79, no. 5, p. 402, 2019.

[48] E. Abbas *et al.*, "Charmonium and e^+e^- pair photoproduction at mid-rapidity in ultra-peripheral Pb-Pb collisions at $\sqrt{s_{\rm NN}}$=2.76 TeV," *Eur. Phys. J. C*, vol. 73, no. 11, p. 2617, 2013.

[49] B. Abelev *et al.*, "Coherent J/ψ photoproduction in ultra-peripheral Pb-Pb collisions at $\sqrt{s_{NN}} = 2.76$ TeV," *Phys. Lett. B*, vol. 718, pp. 1273–1283, 2013.

[50] S. Acharya *et al.*, "Coherent J/ψ photoproduction at forward rapidity in ultra-peripheral Pb-Pb collisions at $\sqrt{s_{\rm NN}} = 5.02\,\text{TeV}$," *Phys. Lett. B*, vol. 798, p. 134926, 2019.

[51] S. Acharya *et al.*, "Coherent J/ψ and ψ' photoproduction at midrapidity in ultra-peripheral Pb-Pb collisions at $\sqrt{s_{\rm NN}} = 5.02$ TeV," *Eur. Phys. J. C*, vol. 81, no. 8, p. 712, 2021.

[52] V. Khachatryan *et al.*, "Coherent J/ψ photoproduction in ultra-peripheral PbPb collisions at $\sqrt{s_{NN}} = 2.76$ TeV with the CMS experiment," *Phys. Lett. B*, vol. 772, pp. 489–511, 2017.

[53] R. Aaij *et al.*, "Study of coherent J/ψ production in lead-lead collisions at $\sqrt{\rm s_{NN}}$ = 5 TeV," *JHEP*, vol. 07, p. 117, 2022.

[54] R. Aaij *et al.*, "Study of exclusive photoproduction of charmonium in ultra-peripheral lead-lead collisions," *JHEP*, vol. 06, p. 146, 2023.

[55] C. A. Bertulani, S. R. Klein, and J. Nystrand, "Physics of ultra-peripheral nuclear collisions," *Ann. Rev. Nucl. Part. Sci.*, vol. 55, pp. 271–310, 2005.

[56] V. Guzey, E. Kryshen, and M. Zhalov, "Coherent photoproduction of vector mesons in ultraperipheral heavy ion collisions: Update for run 2 at the CERN Large Hadron Collider," *Phys. Rev. C*, vol. 93, no. 5, p. 055206, 2016.

[57] S. Agostinelli *et al.*, "GEANT4 - A Simulation Toolkit," *Nucl. Instrum. Meth. A*, vol. 506, pp. 250–303, 2003.

[58] A. M. Sirunyan *et al.*, "Observation of Forward Neutron Multiplicity Dependence of Dimuon Acoplanarity in Ultraperipheral Pb-Pb Collisions at $\sqrt{s_{NN}}$=5.02 TeV," *Phys. Rev. Lett.*, vol. 127, no. 12, p. 122001, 2021.

[59] S. Chatrchyan *et al.*, "Performance of CMS Muon Reconstruction in *pp* Collision Events at $\sqrt{s} = 7$ TeV," *JINST*, vol. 7, p. P10002, 2012.

[60] B. Abelev *et al.*, "Measurement of the Cross Section for Electromagnetic Dissociation with Neutron Emission in Pb-Pb Collisions at $\sqrt{s_{NN}} = 2.76$ TeV," *Phys. Rev. Lett.*, vol. 109, p. 252302, 2012.

[61] G. Aad *et al.*, "Exclusive dimuon production in ultraperipheral Pb+Pb collisions at $\sqrt{s_{\mathrm{NN}}} = 5.02$ TeV with ATLAS," *Phys. Rev. C*, vol. 104, p. 024906, 2021.

[62] S. Acharya *et al.*, "Coherent J/ψ photoproduction at forward rapidity in ultraperipheral Pb-Pb collisions at $\sqrt{s_{\mathrm{NN}}} = 5.02$ TeV," *Phys. Lett. B*, vol. 798, p. 134926, 2019.

[63] M. Abdallah *et al.*, "Tomography of ultrarelativistic nuclei with polarized photon-gluon collisions," *Sci. Adv.*, vol. 9, no. 1, p. eabq3903, 2023.

[64] R. L. Workman *et al.*, "Review of Particle Physics," *PTEP*, vol. 2022, p. 083C01, 2022.

[65] D. d'Enterria and C. Loizides, "Progress in the Glauber Model at Collider Energies," *Ann. Rev. Nucl. Part. Sci.*, vol. 71, pp. 315–344, 2021.

[66] A. J. Baltz, M. J. Rhoades-Brown, and J. Weneser, "Heavy ion partial beam lifetimes due to Coulomb induced processes," *Phys. Rev. E*, vol. 54, pp. 4233–4239, 1996.

[67] A. Łuszczak and W. Schäfer, "Coherent photoproduction of J/ψ in nucleus-nucleus collisions in the color dipole approach," *Phys. Rev. C*, vol. 99, no. 4, p. 044905, 2019.

[68] H. Mäntysaari and B. Schenke, "Probing subnucleon scale fluctuations in ultraperipheral heavy ion collisions," *Phys. Lett. B*, vol. 772, pp. 832–838, 2017.

[69] J. Cepila, J. G. Contreras, and M. Krelina, "Coherent and incoherent J/ψ photonuclear production in an energy-dependent hot-spot model," *Phys. Rev. C*, vol. 97, no. 2, p. 024901, 2018.

[70] D. Bendova, J. Cepila, J. G. Contreras, and M. Matas, "Photonuclear J/ψ production at the LHC: Proton-based versus nuclear dipole scattering amplitudes," *Phys. Lett. B*, vol. 817, p. 136306, 2021.

[71] K. J. Eskola, C. A. Flett, V. Guzey, T. Löytäinen, and H. Paukkunen, "Exclusive J/ψ photoproduction in ultraperipheral Pb+Pb collisions at the CERN Large Hadron Collider calculated at next-to-leading order perturbative QCD," *Phys. Rev. C*, vol. 106, no. 3, p. 035202, 2022.

[72] K. J. Eskola, C. A. Flett, V. Guzey, T. Löytäinen, and H. Paukkunen, "Next-to-leading order perturbative QCD predictions for exclusive J/ψ photoproduction in oxygen-oxygen and lead-lead collisions at energies available at the CERN Large Hadron Collider," *Phys. Rev. C*, vol. 107, no. 4, p. 044912, 2023.

[73] V. N. Gribov, "Interaction of gamma quanta and electrons with nuclei at high-energies," *Zh. Eksp. Teor. Fiz.*, vol. 57, pp. 1306–1323, 1969.

[74] L. Frankfurt, V. Guzey, M. McDermott, and M. Strikman, "Revealing the black body regime of small x DIS through final state signals," *Phys. Rev. Lett.*, vol. 87, p. 192301, 2001.

[75] L. Frankfurt, M. Strikman, and M. Zhalov, "Signals for black body limit in coherent ultraperipheral heavy ion collisions," *Phys. Lett. B*, vol. 537, pp. 51–61, 2002.

[76] S. Acharya *et al.*, "Energy dependence of coherent photonuclear production of J/ψ mesons in ultra-peripheral Pb-Pb collisions at $\sqrt{s_{NN}} = 5.02$ TeV," *JHEP*, vol. 10, p. 119, 2023.

[77] M. I. Abdulhamid *et al.*, "Observation of Strong Nuclear Suppression in Exclusive J/ψ Photoproduction in Au+Au Ultraperipheral Collisions at RHIC," *Phys. Rev. Lett.*, vol. 133, no. 5, p. 052301, 2024.

[78] T. C. Collaboration, "Description and performance of track and primary-vertex reconstruction with the cms tracker," *Journal of Instrumentation*, vol. 9, p. P10009–P10009, Oct. 2014.

[79] S. Chatrchyan *et al.*, "Study of the Inclusive Production of Charged Pions,

Kaons, and Protons in pp Collisions at $\sqrt{s} = 0.9$, 2.76, and 7 TeV," *Eur. Phys. J. C*, vol. 72, p. 2164, 2012.

[80] A. Hayrapetyan *et al.*, "Nonresonant central exclusive production of charged-hadron pairs in proton-proton collisions at s=13 TeV," *Phys. Rev. D*, vol. 109, no. 11, p. 112013, 2024.

[81] S. Acharya *et al.*, "Photoproduction of K+K- Pairs in Ultraperipheral Collisions," *Phys. Rev. Lett.*, vol. 132, no. 22, p. 222303, 2024.

[82] M. Derrick *et al.*, "Measurement of elastic ϕ photoproduction at HERA," *Phys. Lett. B*, vol. 377, pp. 259–272, 1996.

[83] T. Mibe *et al.*, "First measurement of coherent phi-meson photoproduction on deuteron at low energies," *Phys. Rev. C*, vol. 76, p. 052202, 2007.

[84] V. Khachatryan *et al.*, "Multiplicity and rapidity dependence of strange hadron production in pp, pPb, and PbPb collisions at the LHC," *Phys. Lett. B*, vol. 768, pp. 103–129, 2017.

[85] M. G. Ryskin and Y. M. Shabelski, "Elastic rho-prime and phi meson photoproduction and electroproduction with nonresonant background," *Phys. Atom. Nucl.*, vol. 62, pp. 980–986, 1999.

[86] P. Lebiedowicz, O. Nachtmann, and A. Szczurek, "Towards a complete study of central exclusive production of K^+K^- pairs in proton-proton collisions within the tensor Pomeron approach," *Phys. Rev. D*, vol. 98, p. 014001, 2018.

[87] J. Breitweg *et al.*, "Measurement of diffractive photoproduction of vector mesons at large momentum transfer at HERA," *Eur. Phys. J. C*, vol. 14, pp. 213–238,

2000.

[88] A. Tumasyan *et al.*, "Probing Small Bjorken-x Nuclear Gluonic Structure via Coherent J/ψ Photoproduction in Ultraperipheral Pb-Pb Collisions at sNN=5.02 TeV," *Phys. Rev. Lett.*, vol. 131, no. 26, p. 262301, 2023.

[89] J. Adam *et al.*, "Coherent ρ^0 photoproduction in ultra-peripheral Pb-Pb collisions at $\sqrt{s_{\mathrm{NN}}} = 2.76$ TeV," *JHEP*, vol. 09, p. 095, 2015.

[90] S. Acharya *et al.*, "First measurement of coherent ρ0 photoproduction in ultra-peripheral Xe–Xe collisions at sNN=5.44 TeV," *Phys. Lett. B*, vol. 820, p. 136481, 2021.

[91] E. Iancu, K. Itakura, and S. Munier, "Saturation and BFKL dynamics in the HERA data at small x," *Phys. Lett. B*, vol. 590, pp. 199–208, 2004.

[92] H. Kowalski, L. Motyka, and G. Watt, "Exclusive diffractive processes at HERA within the dipole picture," *Phys. Rev. D*, vol. 74, p. 074016, 2006.

[93] J. Bartels, K. J. Golec-Biernat, and H. Kowalski, "A modification of the saturation model: DGLAP evolution," *Phys. Rev. D*, vol. 66, p. 014001, 2002.

[94] A. H. Rezaeian, M. Siddikov, M. Van de Klundert, and R. Venugopalan, "Analysis of combined HERA data in the Impact-Parameter dependent Saturation model," *Phys. Rev. D*, vol. 87, no. 3, p. 034002, 2013.

[95] K. J. Golec-Biernat and M. Wusthoff, "Saturation effects in deep inelastic scattering at low Q**2 and its implications on diffraction," *Phys. Rev. D*, vol. 59, p. 014017, 1998.

[96] V. P. Gonçalves and B. D. Moreira, "A phenomenological analysis of the non-perturbative QCD contributions for the photon wave function," *Eur. Phys. J. C*, vol. 80, no. 6, p. 492, 2020.

[97] L. Jenkovszky, E. d. S. Rocha, and M. V. T. Machado, "Investigating exclusive $\rho 0$ photoproduction within the Regge phenomenology approach," *Phys. Lett. B*, vol. 835, p. 137585, 2022.

[98] L. Jenkovszky, E. S. Rocha, and M. V. T. Machado, "Light vector meson photoproduction in ultraperipheral heavy-ion collisions at the LHC within the Reggeometric Pomeron approach," *Astron. Nachr.*, vol. 344, no. 1-2, p. e220117, 2023.

[99] V. N. Gribov, "Glauber corrections and the interaction between high-energy hadrons and nuclei," *Sov. Phys. JETP*, vol. 29, pp. 483–487, 1969.

[100] R. J. Glauber and G. Matthiae, "High-energy scattering of protons by nuclei," *Nucl. Phys. B*, vol. 21, pp. 135–157, 1970.

[101] T. H. Bauer, R. D. Spital, D. R. Yennie, and F. M. Pipkin, "The Hadronic Properties of the Photon in High-Energy Interactions," *Rev. Mod. Phys.*, vol. 50, p. 261, 1978. [Erratum: Rev.Mod.Phys. 51, 407 (1979)].

[102] V. P. Gonçalves, M. V. T. Machado, B. D. Moreira, F. S. Navarra, and G. S. dos Santos, "Color dipole predictions for the exclusive vector meson photoproduction in pp , pPb , and PbPb collisions at run 2 LHC energies," *Phys. Rev. D*, vol. 96, no. 9, p. 094027, 2017.

[103] S. Acharya *et al.*, "Coherent photoproduction of ρ^0 vector mesons in ultra-peripheral Pb-Pb collisions at $\sqrt{s_{NN}} = 5.02$ TeV," *JHEP*, vol. 06, p. 035, 2020.

[104] R. Aaij *et al.*, "Observation of Exotic J/$\psi\phi$ Resonant Structure in Diffractive Processes in Proton-Proton Collisions," *Phys. Rev. Lett.*, vol. 134, no. 3, p. 031902, 2025.

[105] A. Hayrapetyan *et al.*, "New Structures in the J/ψJ/ψ Mass Spectrum in Proton-Proton Collisions at s=13 TeV," *Phys. Rev. Lett.*, vol. 132, no. 11, p. 111901, 2024.